E.O. Paton Electric Welding Institute of the National Academy of Science of Ukraine
International Association «Welding»

The Paton Welding Journal

02
2023

International Scientific-Technical and Production Journal ◊ Founded in January 2000 (12 Issues Per Year)

Address of Editorial Board
E.O. Paton Electric Welding Institute, 11 Kazymyr Malevych Str., 03150, Kyiv, Ukraine
Tel./Fax: (38044) 205 23 90, E-mail: journal@paton.kiev.ua
https://patonpublishinghouse.com/eng/journals/tpwj

State Registration Certificate 24933-14873 ПР from 13.08.2021
ISSN 0957-798X, DOI: http://dx.doi.org/10.37434/tpwj

Subscriptions, 12 issues per year:
$384 — annual subscription for the printed (hard copy) version, air postage and packaging included;
$312 — annual subscription for the electronic version (sending issues in pdf format or providing access to IP addresses).

Representative Office of «The Paton Welding Journal» in China:
China-Ukraine Institute of Welding, Guangdong Academy of Sciences
Address: Room 210, No. 363 Changxing Road, Tianhe, Guangzhou, 510650, China.
Zhang Yupeng, Tel: +86-20-61086791, E-mail: patonjournal@gwi.gd.cn

The content of the journal includes articles received from authors from around the world in the field of welding, metallurgy, material science and selectively includes translations into English of articles from the following journals, published by PWI in Ukrainian:
- Automatic Welding (https://patonpublishinghouse.com/eng/journals/as);
- Electrometallurgy Today (https://patonpublishinghouse.com/eng/journals/sem);
- Technical Diagnostics & Nondestructive Testing (https://patonpublishinghouse.com/eng/journals/tdnk).

CONTENTS

ORIGINAL ARTICLES

*Translated Article(s) from «Automatic Welding», No. 2, 2023.

**Translated Article(s) from «Electrometallurgy Today», No. 4, 2022.

***Translated Article(s) from «Technical Diagnostics & Nondestructive Testing», No. 1, 2023.

DOI: https://doi.org/10.37434/tpwj2023.02.01

IMPROVEMENT OF TECHNOLOGY OF PRODUCING Ti–TiC MODIFIERS AND STUDYING THEIR IMPACT ON THE STRUCTURE OF DEPOSITED METAL OF TYPE 25Kh5FMS

L.M. Lobanov[1], O.M. Syzonenko[2], I.O. Ryabtsev[1], M.O. Pashchyn[1], A.A. Babinets[1], I.P. Lentyugov[1], A.S. Torpakov[2], O.L. Mikhodui[1], T.G. Solomiichuk[1]

[1]E.O. Paton Electric Welding Institute of the NASU
11 Kazymyr Malevych Str., 03150, Kyiv, Ukraine
[2]Institute of Pulse Processes and Technologies of the NASU
43a Bohoyavlensky Prosp., 54018, Mykolaiv, Ukraine

ABSTRACT

The technology of producing Ti–TiC modifiers was improved, which allowed reducing the average diameter of its particles by more than 6 times. The use of the proposed treatment procedure made it possible to produce a Ti–TiC powder with at least 20 % of TiC in its composition. It was found that for the investigated modes, treatment in kerosene is more effective in terms of dispersion than treatment in ethanol. The use of the produced powder as a modifier at its content in a deposited metal 25Kh-5FMS at a level of 0.01 %, leads to a significant change in the microstructure and its transformation from a columnar into a cellular one. In terms of the possibility to control the structure and properties of the deposited metal, the most promising is the use of modified Ti–TiC powders of N2 and N4 type, which were produced as a result of high-voltage treatment of the mixture of corresponding powders in a hydrocarbon liquid using a volumetrically-distributed multi-spark discharge mode. This provides a significant effect on the structure of the deposited metal of type 25Kh5FMS, but at the same time does not lead to the formation of microcracks in the deposited metal.

KEYWORDS: modification, technology of producing modifiers, high-voltage treatment, hydrocarbon liquid, arc surfacing, flux-cored wire, deposited metal, structure of deposited metal, nonmetallic inclusions

INTRODUCTION

The introduction of different types of modifiers into the melt of metals is a fairly common method of refining their structure and enhancing mechanical and service properties. Modifiers and microalloying elements are also used to refine the structure and prevent crystalline growth orientation during solidification of the welding pool in surfacing and welding production [1–8]. Technical literature gives data on the use of modifiers containing boron or yttrium, to refine the structure and increase the service properties of the deposited metal [2, 3]. However, modifiers containing these elements are very expensive, which does not always justify their use from an economic point of view.

In [9], the example of using Ti–TiC modifier at casting shows that its introduction has made it possible to reduce the size of the grain and increase the mechanical characteristics of the heat-resistant SM88U alloy. This indicates the prospect of using Ti–TiC metal powders for modification and microalloying of deposited metal of different alloying systems.

The technology of producing Ti–TiC modifier was developed at the Institute of Pulse Processes and Technology of the NASU. According to this technology, to produce Ti–TiC modifiers, the treatment of a mixture of corresponding powders with a high-voltage electric discharge (HED) in the hydrocarbon liquid is used.

HED in the liquid is a unique comprehensive method of influencing various dispersed systems in order to disperse them, which is accompanied by a change in the structure and phase composition of the latter. HED is characterized by instantaneous release of a large amount of energy (units, tens or hundreds of kJ) in the original small volume of the discharge channel within a few microseconds. A high concentration of energy in the plasma channel of discharge leads to generation of electromagnetic and thermal fields, intensive waves of pressure, hydraulic flows, volumetric microcavitation and electro-erosion processes in the volume of a discharge chamber, that promote dispersion and evolution in the structure of dispersed systems [10, 11].

The work investigates the possibility of using Ti–TiC modifier to refine the metal structure using PP-Np-25Kh5FMS flux-cored wire. Also the results of improving the technology of producing Ti–TiC modifier using different technological modes and hydrocarbon liquid media are presented.

Thus, the aim of the work is to improve the technology of producing Ti–TiC modifier with the use of

HED and investigation of its impact on the structure of the deposited metal of type 25Kh5FMS.

PROCEDURES OF INVESTIGATIONS

Improvement of the technology of producing Ti–TiC modifier using HED was performed in an experimental bench, the circuit of which is shown in Figure 1, and the principle of operation is described in the article [11].

The study of HED in the dispersed system "liquid dielectric–metal powder" was performed at the voltage of capacitors charge U = 50 kV, the inductance of the discharge circuit L = 0.7 μH and the discharge gap l_d, which was selected depending on the working liquid and amounted to ~17 mm for kerosene and ~24 mm for ethanol. The capacity of the capacitor C was 0.8 μF, so the value of a stored single discharge energy W_1 was 1 kJ. The specific treatment energy was 20 MJ/kg. According to the results given in [10, 11], namely such values of the parameters of HED-treatment allow reaching the balance between refining, the amount of synthesized titanium carbide powder and the number of free nanocarbon particles.

The use of kerosene as a working medium in the treatment of mixtures of powders allows synthesizing nanocarbon of different allotropic modifications as a result of pyrolysis of hydrocarbon chains by plasma of the discharge channel. Active nanocarbon is able to react with Ti powder, resulting in synthesis of titanium carbide [12]. Due to the change in the composition of the hydrocarbon liquid, it is possible to control the amount of a synthesized nanocarbon, so in the work as a working medium for the realization of HED, kerosene and ethanol were used. The ratio of the solid and liquid phase in the studies was 1:15 (the weight of the treated powder was 100 g, the volume of a working liquid was 1.5 dm^3).

During each treatment, the record of discharge current and voltage within every 100 discharges was performed by means of the oscillograms. The values of electrical and hydrodynamic characteristics for each of the treatments were averaged according to the results of the calculations for recorded oscillograms. For each of the following modes, no less than three experiments were performed.

HED-treatment of Ti powder with the use of single-edge and three-edge electrode systems (ES) in kerosene or ethanol medium was performed. When using the "one edge-plane" system, HED propagates according to the classical mechanism of the spark discharge (SD) in the dispersed system, while the use of ES of type "three edges-plane" allows realizing the mode of volumetrically-distributed multi-spark discharge (VMD). Modifiers produced as a result of treatment were marked respectively as N1 and N2 (kerosene medium) and N3 and N4 (ethanol medium) (Table 1).

To estimate the degree of HED exposure in the hydrocarbon medium on the morphology and the sizes of powders particles, an optical microscope BIOLAM-I with a maximum magnification of ×1350, a scanning electron microscope REM-MA-102 with a range of magnification from 10 to ×250000 and a digital camera Canon were used. The powder samples for optical microscopy were selected in accordance with GOST 23402–78.

The study of the phase composition of powders was performed by X-ray-phase analysis using a DRON-4-07 diffractometer at CuKα-radiation. The phase identification on diffractograms was carried out accoding to the bases POW_COD. The quantitative phase composition was determined accoding to the procedure of evaluating the intensity using the corundum number

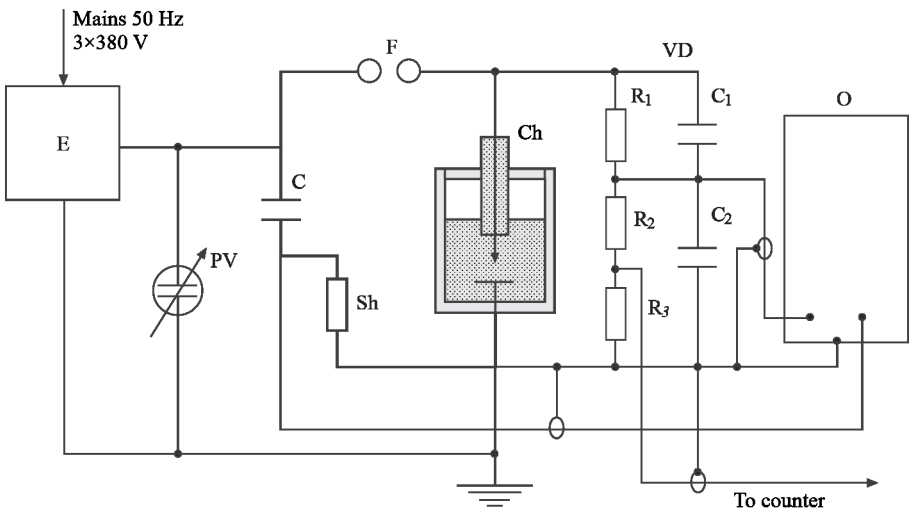

Figure 1. Circuit of experimental bench for electric discharge treatment of powders: E — power part; PV — kilovolt meter; C — capacitive capacitor; Sh — coaxial shunt; K — working chamber; O — memorizing oscilloscope; F — air discharger; VD — voltage divider; R1, R2, R3, C1, C2 — elements of voltage divider

Table 1. Characteristics of metal, deposited using flux-cored wires PP-Np-25Kh5FMS containing Ti–TiC modifiers, which are produced by HED-treatment on different modes

Modifier description	Working medium	Discharge mode	Content of TiC in the powder after treatment, %	Size of crystallites l_c, μm/type of structure	Hardness of deposited metal *HV*1, MPa
Without modifier	–	–	–	30–60/columnar	5920–6060
N1	Kerosene	SD	20	30–180/cellular	6410–6420
N2		VMD	23	20–80/cellular	5700–5800
N3	Ethanol	SD	20	35–170/cellular	6350–6600
N4		VMD	23	30–100/cellular	5250–5330

of RIR (Reference Intensity Ratio) using QualX and a full profile analysis using Maud program.

The specimenss for microstructure examination were produced by arc surfacing with the flux-cored wires on plates of 40Kh steel. For surfacing, the flux-cored wire PP-Np-25Kh5FMS was used, in the charge of which powders modifiers were added with such a calculation as to obtain the content of a modifier in the deposited metal at a level of 0.01 %. As a reference, the specimens deposited by the flux-cored wire PP-Np-25Kh5FMS without modifiers were used. The diameter of all the developed wires is 1.8 mm, the filling factor is 25 %. In total, five experimental flux-cored wires were manufactured (see Table 1).

Surfacing of all the specimens was performed under the flux AN-26P on the same mode: current — 220–230 A, voltage — 36–37 V, deposition rate — 25 m/h. In order to avoid the impact of the base metal stirring, on each specimen the surfacing was performed in four layers. In order to avoid crystallization cracks, before surfacing, the specimens were heated to 200 °C and after surfacing, they were cooled with the furnace. After complete cooling, from the deposited specimens, transverse billets were cut out for preparation of appropriate microsections and conducting metalographic examinations.

The specimens for metallographic examinations were prepared by standard procedures. To reveal microstructure, the specimens were etched electrolytically in a 20 % solution of chromic acid at a voltage of 20 V.

Examinations of microstructure and nonmetallic inclusions of the deposited metal were carried out in NEOPHOT-32 microscope. The hardness measurements were carried out in M-400 LECO hardness meter at a load of 100 g and 1 kg. The photos of microstructures were obtained with OLYMPUS C-500 camera.

RESEARCH RESULTS AND DISCUSSION

The results of studying the change in the dispersion of Ti powder after HED-treatment in different modes are shown in Figure 2. The original titanium powder had a monomodal distribution of particles by sizes, the peak of which was at a point corresponding to the diameter of ~30 μm and 54 % of the powder particles had a size smaller than this value (see Figure 2, curve *1*), and the average diameter of such powder was 60 μm.

Analyzing the results presented in Figure 2, it should be noted that HED-treatment in all studied modes provided a significant reduction in the average diameter of the powder particles and changed the nature of its distribution by sizes. Thus, HED-treatment in kerosene in SD mode allowed producing a Ti–TiC system powder with an average diameter of 8.2 μm. The distribution of such powder by sizes had a bimodal nature (curve *2*) — one of the peaks was close to the initial range of sizes and amounted to 7.5 μm (32 %) and the other was in the size range of less than 1 μm (0.6 μm, 37 %).

Changing the treatment mode on VMD with the preservation of kerosene as a working medium allowed increasing the efficiency of dispersion — the produced Ti–TiC system powder had an average diameter of 7.4 μm. It was characterized by an almost monomodal distribution (curve *3*), the main peak of which was at a point corresponding to a diameter of 0.7 μm (44 %). Namely such a mode was the most effective in terms of dispersion of powder particles.

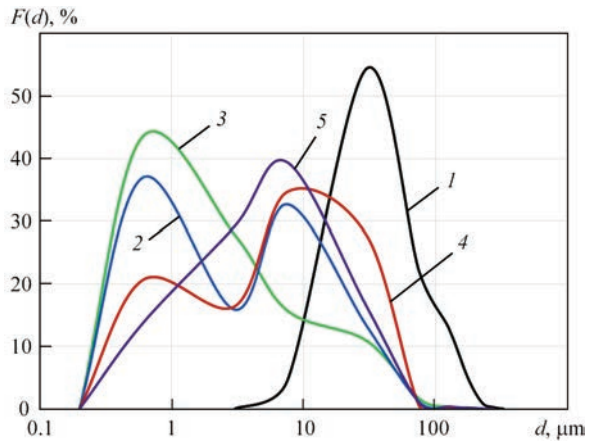

Figure 2. Distribution of powder particles of modifiers by sizes *d* before and after HED-treatment at different modes: *1* — initial Ti powder; *2* — modifier N1, treatment medium — kerosene, SD mode; *3* — modifier N2, treatment medium — kerosene, VMD mode; *4* — modifier N3, treatment medium — ethanol, SD mode; *5* — modifier N4, treatment medium — ethanol, VMD mode

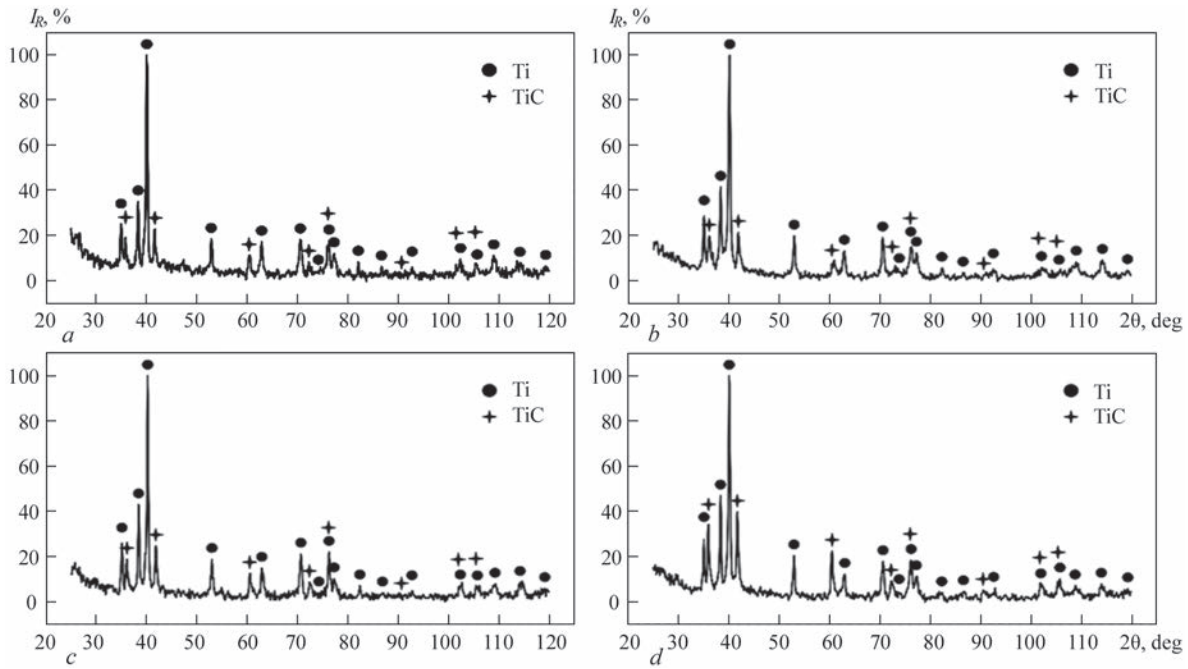

Figure 3. Diffraction patterns of Ti–TiC powder mixture produced by HED-treatment of titanium powder: *a* — modifier N1, treatment medium — kerosene, SD mode; *b* — modifier N2, treatment medium — kerosene, VMD mode; *c* — modifier N3, treatment medium — ethanol, SD mode; *d* — modifier N4, treatment medium — ethanol, VMD mode

The change in a working medium from kerosene to ethanol during the realization of SD mode allowed producing a Ti–TiC powder with an average diameter of 12.1 μm. The distribution of this powder by sizes had a bimodal nature (curve *4*) — peaks were observed at the points of 10 (35 %) and 0.8 μm (21 %).

The change in the discharge mode on VMD by replacement of the electrode system "one edge–plane" with the electrode system "three edges–plane" with the preservation of ethanol as a working medium of HED made it possible to increase the efficiency of dispersion in ethanol. The produced Ti–TiC powder was characterized by an average diameter of 10.2 μm, and its distribution had a monomodal nature (curve *5*) with a peak at a point that corresponds to a diameter of 7.5 μm (40 %).

Thus, treatment of Ti powder in all the considered modes allowed reducing its average diameter by more than 6 times. VMD treatment allows obtaining an almost monomodal distribution of particles by sizes and is distinguished by a higher efficiency of dispersion. Treatment in kerosene for the investigated modes is more effective in terms of dispersion than treatment in ethanol.

The studies of the diffraction patterns of samples of the treated powders obtained in the X-ray diffractometer DRON-4 are shown in Figure 3. On all the diffraction patterns in addition to the peaks characteristic of Ti, there are also peaks that indicate the synthesis of TiC in the process of HED-treatment of the initial titanium powder.

The results of quantitative analysis by the RIR method indicate that the amount of a synthesized titanium carbide for all studied modes differs within the error (Table 1). Somewhat better results in terms of carbidization efficiency were observed during treatment in ethanol in SD mode, but all the modes allowed producing no less than 20 % of TiC in the powder composition after its treatment. These results confirm the conclusion made in [8, 9], that Ti powder carbidization efficiency is most influenced by the specific energy of treatment, which was constant for all the studied modes and amounted to 20 MJ/kg.

The microstructure of the metal was studied, deposited with five experimental flux-cored wires (Figure 4, *a–e* and Figure 5, *a*, *b*).

The microstructure of the specimen metal, deposited by the wire PP-Np-25Kh5FMS without adding modifier (Table 1, line 1) consists of columnar crystallites (Figure 4, *a*), which grow in the direction of heat removal. The width of the crystallites is in the range of 30–60 μm. In the body of crystallites, an acicular martensitic structure is observed, on the boundaries of cast crystallites, light precipitates are observed that correspond to residual austenite (Figure 4, *a*). The precipitates of a rounded shape, that can be complex carbides, are quite rarely observed. The hardness of the deposited metal is *HV*1 – 5920–6060 MPa. The defects both in the deposited metal and near the fusion line are absent.

Microstructure of the metal of the specimen deposited by the PP-Np-25Kh5FMS wire with the content of the modifier N1 with the content of 80 % of

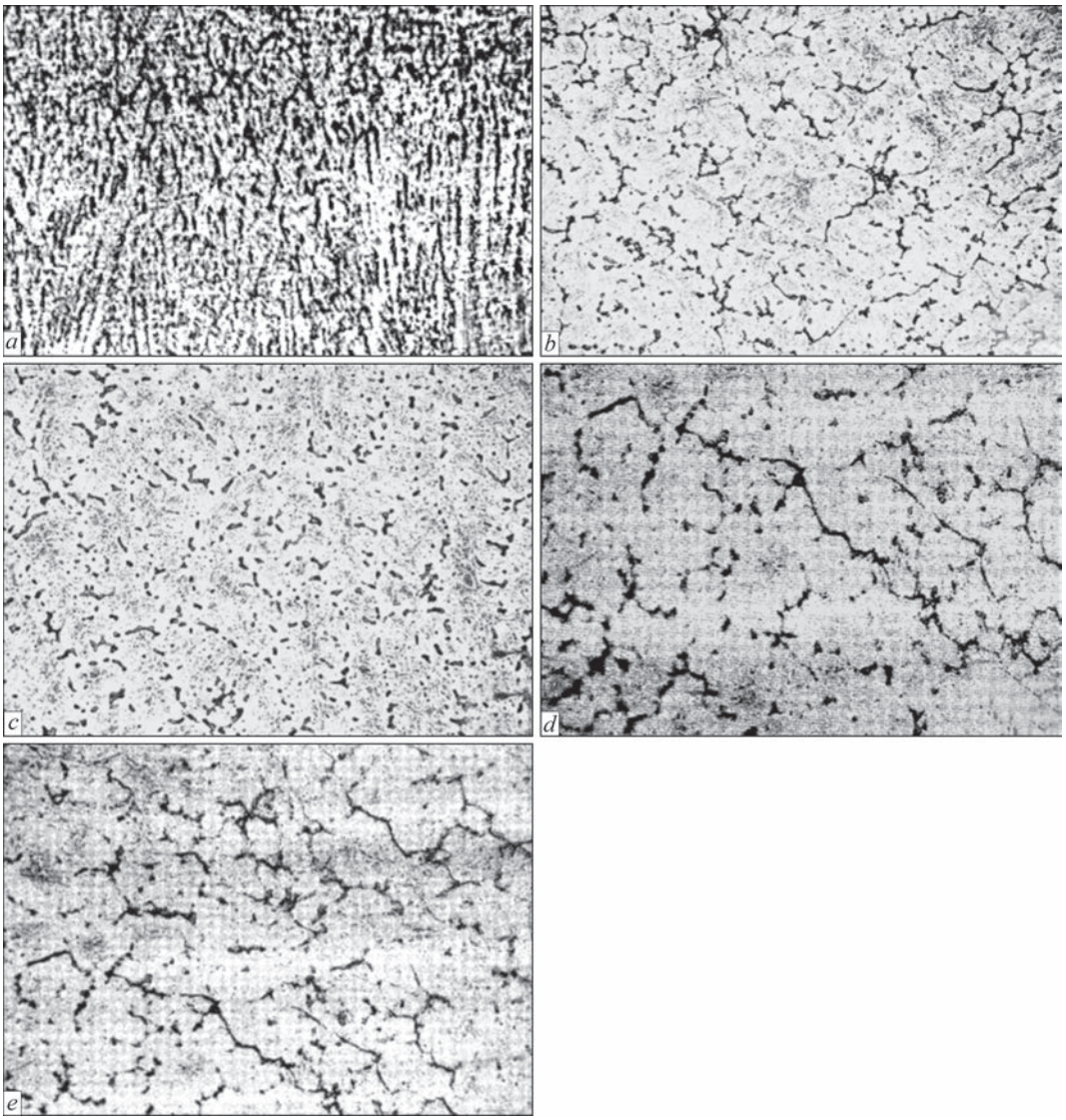

Figure 4. Microstructure (×200) of metal, deposited with a flux-cored wire PP-Np-25Kh5FMS: *a* — without microalloying additives; *b* — using modifier N1; *c* — N2; *d* — N3; *e* — N4

Ti + 20 % TiC (Table 1, line 2), was refined (Figure 4, *b*). The structure of martensite was also refined. The size of the cells is within 30–180 μm. On the boundaries of cells, a quite large number of dark-etched phase and rounded precipitates is observed that are built into chains and probably may represent carbides. In addition, in the upper layer of the deposited metal microcracks are observed, which is undesirable (Figure 5, *a*). The hardness of the deposited metal is *HV*1 – 6410–6420 MPa.

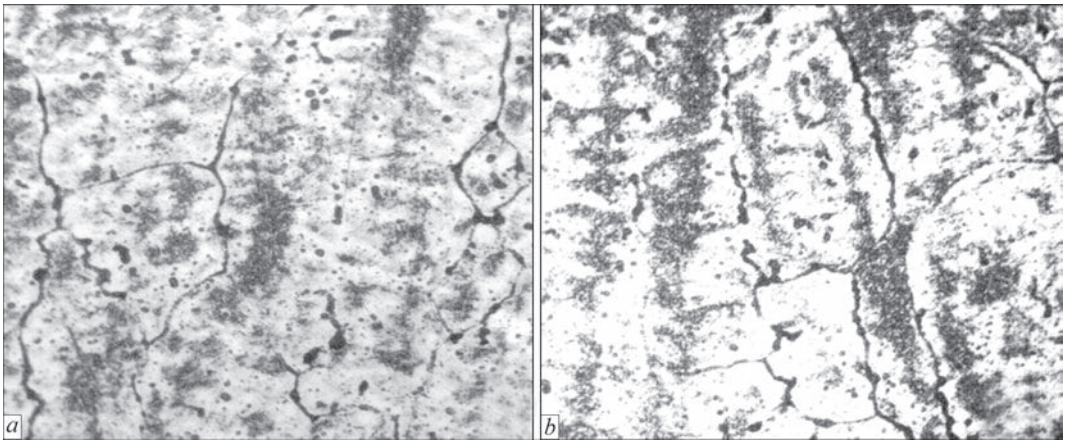

Figure 5. Microstructure (×600) of metal, deposited with PP-Np-25Kh5FMS flux-cored wire, with microcracks: *a* — with the use of modifier N1; *b* — N3

Microstructure of the specimen metal, deposited by PP-Np-25Kh5FMS wire with the content of the modifier N2 with a composition of 77 % Ti + 23 % TiC (Table 1, line 3), represents a cast cellular structure (Figure 4, *c*). In the body of crystallites, a large acicular martensitic structure with the hardness $HV_{0.1}$ — 4900–5450 MPa is observed. On the boundaries of cast crystallites, a light-etched austenitic structure with the hardness $HV_{0.1}$ — 5100 MPa with a few precipitates of carbides and intermetallics is observed. The integrated hardness of this specimen is within *HV*1 — 700–5800 MPa. The size of the cells is 20–80 μm. Microcracks in this specimen were not detected.

The microstructure of the specimen, deposited by the wire PP-Np-25Kh5FMS with the content of the modifier N3 with a composition of 80 % Ti + 20 % TiC (Table 1, line 4; Figure 4, *d*) was investigated. It represents a matrix, consisting of slightly-etched dispersed needles of martensite with the precipitates of carbides or intermetallics, or both of them on the boundaries of cast crystallites in the form of separate or chain inclusions (Figure 4, *d*). The hardness of martensite matrix is $HV_{0.1}$ — 5700–5750 MPa, and integral hardness is within *HV*1 — 6350–6600 MPa. The size of the cells is 35–170 μm. In this specimen, as well as in the specimen with the modifier N1, in the upper layers of deposited metal microcracks were found (Figure 5, *b*).

It should be noted that the modifiers N1 and N3 were produced using HED-treatment in SD mode. In contrast, the modifiers N2 and N4 were produced using HED-treatment in VMD mode. As was shown above, VMD treatment provides producing a larger amount of smaller titanium carbides. In our opinion, this is one of the reasons for the absence of microcracks in the deposited metal with the modifiers N2 and N4.

The microstructure of the specimen, deposited by PP-Np-25Kh5FMS wire with the content of the modifier N4 with a composition of 77 % Ti + 23 % TiC (Table 1, line 5), was also significantly refined (Figure 4, *e*). On the cell boundaries, dark-etched precipitates are observed, but a number of these precipitates is lower than in the similar area of the specimen with the modifier N1. In addition, they do not merge into long chains. Microcracks in this area are also not noted. The hardness of the deposited metal is *HV*1 — 5250–5330 MPa.

Also, according to the procedure of GOST 1778–70, on the polished non-etched microsections, the level of the deposited metal contamination with nonmetallic inclusions was determined. From the presented specimens, the biggest contamination of the deposited metal with nonmetallic inclusions, mainly oxides, is observed in the specimen without modifiers. It corresponds to the grain size No. 3a according to the Table 1 “Spot oxides” GOST 1778–70. The specimens with the modifiers N1, N2, N3 are significantly cleaner from nonmetallic inclusions than the specimen without modifiers and their contamination corresponds to the size No. 1a of the same Table 1. In the specimen with the modifier N4, contamination of the deposited metal with nonmetallic inclusions is the least and amounts to less than the size No. 1 a of the Table 1 “Spot oxides”.

CONCLUSIONS

1. The method of HED-treatment of Ti–TiC powder on different modes in the hydrocarbon liquid allowed reducing the average diameter of its particles by more than 6 times. As a result, a powder with an almost monomodal distribution of particles by sizes was produced.

2. The use of the produced Ti–TiC powder as a modifier with its content in the deposited metal of type 25Kh5FMS at a level of 0.01 % leads to a significant change in the microstructure and its transformation from a columnar into a cellular one.

3. The use of modifiers of type N2 and N4 for Ti–TiC powders seems to be the most promising in terms of the ability to control the structure and properties of the deposited metal, which can significantly affect the structure of the deposited metal of type 25Kh5FMS, but at the same time do not lead to the formation of microcracks on the deposited metal due to the presence of a larger amount of smaller titanium carbides in the composition of these modifiers.

REFERENCES

1. Babinets, A.A., Ryabtsev, I.O. (2021) Influence of modification and microalloying on deposited metal structure and properties (Review). *The Paton Welding J.*, **10**, 3–10. DOI: https://doi.org/10.37434/tpwj2021.10.01
2. Gladky, P.V., Mikaelyan, G.S. (1992) *Microalloying and modification of wear-resistant deposited metal. Deposited metal. Composition, structure, properties.* Kyiv, PWI, 33–36 [in Russian].
3. Babinets, A.A., Ryabtsev, I.O., Lentyugov, I.P., Bogaichuk, I.L. (2022) Influence of microalloying with boron on the structure and properties of deposited metal of the type of tool steel 25Kh5FMS. *The Paton Welding J.*, **6**, 3–11. DOI: https://doi.org/10.37434/tpwj2022.06.01
4. Krivchikov, S.Yu. (2012) Modification by boron of deposited metal of white cast iron type. *The Paton Welding J.*, **6**, 19–21.
5. Maksimov, S.Yu., Machulyak. V.V., Sheremeta, A.V., Goncharenko, E.I. (2014) Investigation of influence of microalloying with titanium and boron of weld metal on its mechanical properties in underwater welding. *The Paton Welding J.*, **6–7**, 76–79. DOI: https://doi.org/10.15407/tpwj2014.06.15
6. Kuznetsov, V.D., Stepanov, D.V. (2015) Structure and properties of weld metal modified by nanooxides. *The Paton Welding J.*, **11**, 10–16. DOI: https://doi.org/10.15407/tpwj2015.11.01

7. Stepnov, K.K., Matvienko, V.N., Oldakovsky, A.I. (2011) Modification of medium-chromium deposited metal. *The Paton Welding J.*, **8**, 10–12.
8. Pu, J., Yu, Sh., Li, Yu. (2017) Effects of Zr–Ti on the microstructure and properties of flux aided backing submerged arc weld metals. *J. of Alloys and Compounds*, **692**, 351–358.
9. Syzonenko, O.M., Prokhorenko, S.V., Lypyan, E.V. et al. (2020) Pulsed discharge preparation of a modifier of Ti–TiC system and its influence on the structure and properties of the metal. *Materials Sci.*, 56(**2**), 232–239. DOI: 10.1007/s11003-020-00421-1
10. Lypyan, E.V., Syzonenko, O.N., Torpakov, A.S., Zdanov, A.A. (2015) Thermodynamical analysis of heterogeneous chemical reactions in system "mixture of Fe–Ti powders – hydrocarbon liquid" under the action of high-voltage electric discharges. *Visnyk NTU KhPI. Seriya: Tekhnika ta Elektrofizyka Vysokykh Naprug. Kharkiv*, 51, 1160, 59–65 [in Russian].
11. Sizonenko, O.N., Tregub, V.A., Lipyan, E.V. (2015) Analysis of physico-technical processes in high-voltage electric-discharge treatment of metal powders. *Vestnik Ukr. Mater. Obshchestva*, **8**, 10–21 [in Russian].
12. Goldshtejn, M.I., Grachev, S.V., Veksler, Yu.J. (1985) *Special steels.* Moscow, Metallurgiya, 308–309 [in Russian].

ORCID
L.M. Lobanov: 0000-0001-9296-2335,
O.M. Syzonenko: 0000-0002-8449-2481,
I.O. Ryabtsev: 0000-0001-7180-7782,
M.O. Pashchyn: 0000-0002-2201-5137,
A.A. Babinets: 0000-0003-4432-8879,
I.P. Lentyugov: 0000-0001-8474-6819,
A.S. Torpakov: 0000-0002-9805-3914,
O.L. Mikhodui: 0000-0001-6660-7540,
T.G. Solomiichuk: 0000-0002-3038-8291

CONFLICT OF INTEREST
The Authors declare no conflict of interest

CORRESPONDING AUTHOR
M.O. Pashchyn
E.O. Paton Electric Welding Institute of the NASU
11 Kazymyr Malevych Str., 03150, Kyiv, Ukraine.
E-mail: svarka2000@ukr.net

SUGGESTED CITATION
L.M. Lobanov, O.M. Syzonenko, I.O. Ryabtsev, M.O. Pashchyn, A.A. Babinets, I.P. Lentyugov, A.S. Torpakov, O.L. Mikhodui, T.G. Solomiichuk (2023) Improvement of technology of producing Ti–TiC modifiers and studying their impact on the structure of deposited metal of type 25Kh5FMS. *The Paton Welding J.*, **2**, 3–9.

JOURNAL HOME PAGE
https://patonpublishinghouse.com/eng/journals/tpwj

Received: 28.12.2022
Accepted: 30.03.2023

DOI: https://doi.org/10.37434/tpwj2023.02.02

STRENGTH AND STRUCTURE OF BUTT, OVERLAP AND FILLET JOINTS OF AMg6M ALLOY PRODUCED BY FRICTION STIR WELDING

A.G. Poklyatskyi, S.I. Motrunich, V.E. Fedorchuk, I.M. Klochkov

E.O. Paton Electric Welding Institute of the NASU
11 Kazymyr Malevych Str., 03150, Kyiv, Ukraine

ABSTRACT

The paper deals with the results of studying the structure and strength of butt, overlap and fillet joints of AMg6M aluminium alloy, produced by friction stir welding (FSW). It is shown that a weld nugget with fine-crystalline structure forms as a result of intensive plastic deformation of the metal. The size of grains, which are of practically globular shape, does not exceed 4–5 μm, and that of dispersed phase precipitates — ≤ 1 μm. In the zone of thermomechanical impact, in addition to fine grains, somewhat larger elongated grains (6–7 мкм) form on the boundary of the weld-to-base metal transition, which are oriented along the direction of plasticized metal displacement by the tool working surfaces. Here, in the HAZ, where the metal did not undergo any deformational impact, the maximum size of its grains is on the level of 10–15 μm. The ultimate strength of samples of butt joints and fillet joints, produced by making butt and overlap-butt welds, is on the level of 335–350 MPa at their static tension, and it practically does not depend on the welded sheet location either from the advancing side or from the retreating side, or on the weld orientation relative to their flanging direction. Here, the butt joint samples fail mainly through the base metal or the boundary of thermomechanical impact zone and heat-affected zone. Samples of fillet joints produced by overlap-butt welds, fail in the zone of weld-to-base metal transition in the thermomechanical impact zone, and those produced by butt welds fail also through the base metal.

KEYWORDS: friction stir welding, AMg6M aluminium alloy, fillet joints, strength, structure, butt joints, overlap joints

INTRODUCTION

The scope of aluminium application in different industries is growing constantly owing to its physical, mechanical and technological properties. The main sectors, which determine the global demand for aluminium alloys, now are construction, packing, general engineering, aerospace engineering, car making and power engineering. Aluminium rolled stock and shaped sections are widely used in industrial and civil construction, in particular for fabrication of lightweight welded structures. Aluminium application in car-making allows a significant increase of strength at reduction of the weight and preservation of the dimensions of cars, ensuring fuel saving. In the aerospace sector aluminium has long been the main structural material and makes up almost 80 % of the aircraft fuselage weight. The modern global aluminium market offers to consumers pure aluminium and almost 300 compositions of structural aluminium alloys with different physico-mechanical properties. The range of marketable products from aluminium and its alloys includes cast ingots, flat rolled stock, shaped sections, extrusions, wire and foil. Therefore, at fabrication of welded structures, depending on their functional purpose, both different aluminium alloys and diverse kinds of semi-finished products are usually used [1].

Increase of the scope of aluminium application is inseparably connected not only with development of new readily weldable alloys, but also with improvement of the currently available and development of promising welding technologies, which allow expansion of their application areas. So, intensification of stirring of molten metal of the weld pool in nonconsumable electrode argon-arc welding with arc oscillation promoted reduction of porosity in welds of aluminium-lithium alloys, breaking up and fragmentation of macroinclusions of oxide film in welds of aluminium-magnesium alloys and formation of a fine-crystalline crack-resistant weld structure [2, 3]. Application of highly-concentrated heat sources in beam and hybrid welding processes enabled reduction of the degree of metal softening in the zone of permanent joint formation and improvement of mechanical properties of welds [4]. Development of FSW process allowed producing welds without application of shielding inert gas or welding wire, avoiding ultraviolet arc radiation and the processes of metal melting and solidification, which lead to formation of defects characteristic for fusion welding in the form of hot cracks, pores and oxide film macroinclusions [5–7]. During FSW, favourable conditions are in place for formation of fine-crystalline weld structure, as a result of plastic deformation of metal [8–10]. Owing to formation of permanent joints at much lower temperatures ($\leq T_S$) compared to fusion welding, the degree of metal softening decreases, high level of the joint mechanical properties and low level of residual

stresses and strains is ensured [11–13]. The advantages of FSW process promoted its wide acceptance by industry at manufacture of undetachable components and structures in different sectors. In shipbuilding it is applied to produce large-sized panels from separate extruded profiles, which are used at fabrication of side sections of the hulls of ships, ferries, launches and boats, walls of refrigerators and cabins, deck superstructures, platforms for helicopters, gangways, masts, oil platforms, etc. In manufacture of railway transport, this process is used to join profiles and rigid integrated panels from different aluminium alloys. In the automotive industry FSW is successfully used in manufacture of the car boot and doors, space frames of motorcycles and bicycles, bodies and lifting devices of trucks, bodies and floors of buses, vans, trailers, elements of chassis, wheel rims, etc. In construction it is used to weld panels of walls and facades, window and door frames, floors and other building elements. This process has become important in construction of bridges, allowing their weight to be reduced and mounting operation duration to be shortened. In the aerospace sector, FSW is used for manufacture of elements of aircraft and missile fuel tanks. In most cases, when designing various components of such products, butt welded joints are predominantly used. It, however, cannot always be done, so that overlap, fillet or tee joints have to be used [14–16].

The objective of this work is investigation of the structure and assessment of the strength of butt, overlap and fillet joints of sheets from AMg6M alloy, produced by FSW.

INVESTIGATION PROCEDURE

Sheets of batch-produced AMg6M aluminium alloy (400×200×1.9 mm) were used to produce butt and overlap joints. Here, four variants of butt joints were welded, depending on weld orientation relative to sheet flanging direction, located from the advancing side (where the directions of rotation and linear displacement of the tool coincide) and the retreating side (where the directions are opposite). The first variant is when both the sheets were positioned along the flanging direction (D), and the second one is when both the sheets were positioned across the flanging direction (P). In the third and fourth variants the sheet oriented along the flanging direction was placed from the advancing side, and the sheet across the flanging direction was located from the retreating side, and vice versa.

Depending on weld position relative to the direction of flanging of the upper and lower sheets, four variants of overlap joints were also produced. In the first and second variant the upper and lower sheets were placed along or across their flanging direction relative to weld orientation, and in the third and fourth variants the upper and lower sheets had different directions of flanging relative to weld orientation.

Fillet joints were produced by making butt and overlap-butt welds, welding similar sheets to 12.0 mm sheets. In the second case, a recess of 6 mm width (half the shoulder diameter) and 1.9 mm depth (thinner sheet thickness) was made in the thick sheet. Here, thicker sheets were placed from the advancing side or from the retreating side.

In keeping with the requirements to welded joints of critical structures, standard chemical etching of the sheets was carried out in NaOH solution with subsequent clarification in HNO_3 solution, and directly before welding mechanical scraping of the sheet surface was performed in the weld formation zone.

FSW was conducted in a laboratory set-up developed at PWI with welding speed V_w = 10 m/h at tool rotation frequency N = 1420 rpm, using a special tool with shoulder diameter of 12 mm and pin in the form of a truncated cone of 3.4 mm diameter at the shoulder base and 12° inclination angle of the forming cone [37]. When welding butt and fillet joints by butt welds, the pin length was 1.75 mm and in welding overlap and fillet joints by overlap-butt welds it was 2.25 mm, so as to ensure a reliable connection of the upper sheet with the lower one.

The produced welded joints were used to cut out sections to study their structural features. The ultimate strength of butt and fillet joints was determined at static uniaxial stretching of standard flat samples with 15 mm width of the working part in versatile servohydraulic system MTS 318.25. The structural features of welded joints were evaluated using an optical electron microscope MMT-1600V.

RESULTS AND DISCUSSION

The conducted experimental studies revealed that at FSW of butt and overlap joints, irrespective of weld orientation relative to the sheet flanging direction, the nature of formation, appearance and macrostructure of such joints remain the same (Figures 1, 2). Thus, at FSW the metallurgical heredity does not affect the structure of such sheet joints of AMg6M aluminium alloy.

Microstructural studies showed that the weld nugget with a fine-crystalline structure forms in the central part of welds in butt joints, as a result of intensive plastic deformation. The size of grains, having a practically globular shape, is not more than 4–5 μm, and that of dispersed phase precipitates is ≤ 1 μm. In the thermomechanical impact zone partial deformation of the metal takes place at the boundary of weld-to-base material transition, so that in addition to fine grains, somewhat larger (6–7 μm) elongated grains

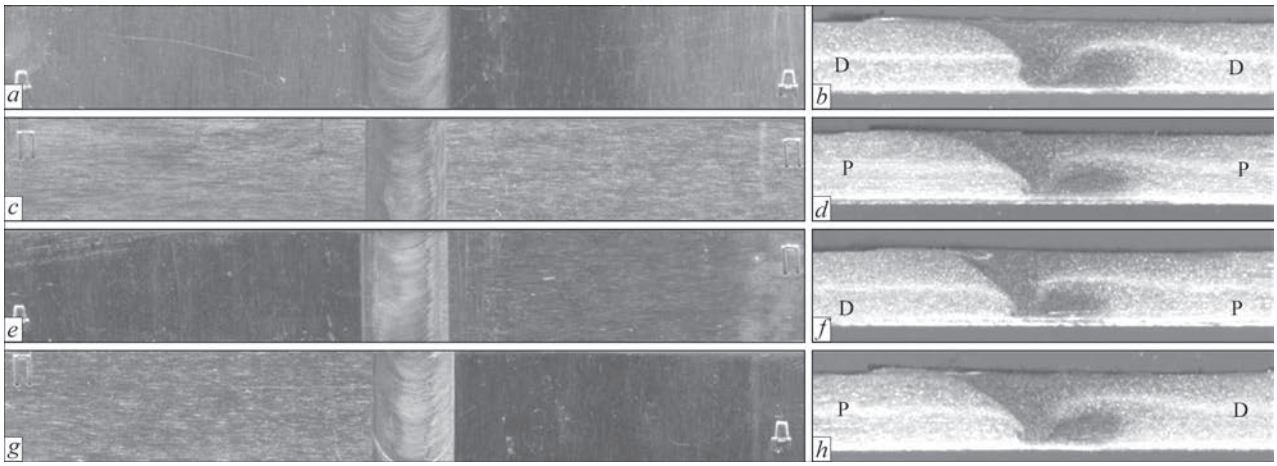

Figure 1. Appearance of surfaces (*a*, *c*, *e*, *g*) and cross-sections (*b*, *d*, *f*, *h*) of butt joints of 1.9 mm AMg6M aluminium alloy, produced by FSW at different orientation of welds relative to the sheet flanging direction (sheet position): D — along the flanging direction, P — across the flanging direction)

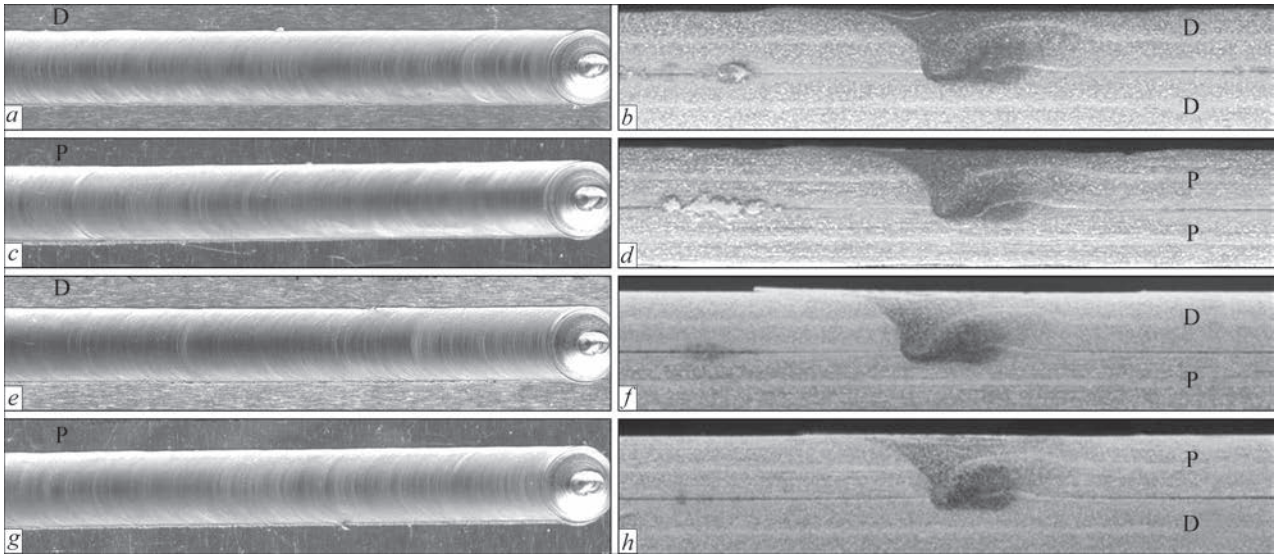

Figure 2. Appearance of surfaces (*a*, *c*, *e*, *g*) and cross-sections (*b*, *d*, *f*, *h*) of overlap joints of 1.9 mm AMg6M aluminium alloy, produced by FSW at different weld orientation relative to sheet flanging direction (sheet position): D — along the flanging direction; P — across the flanging direction)

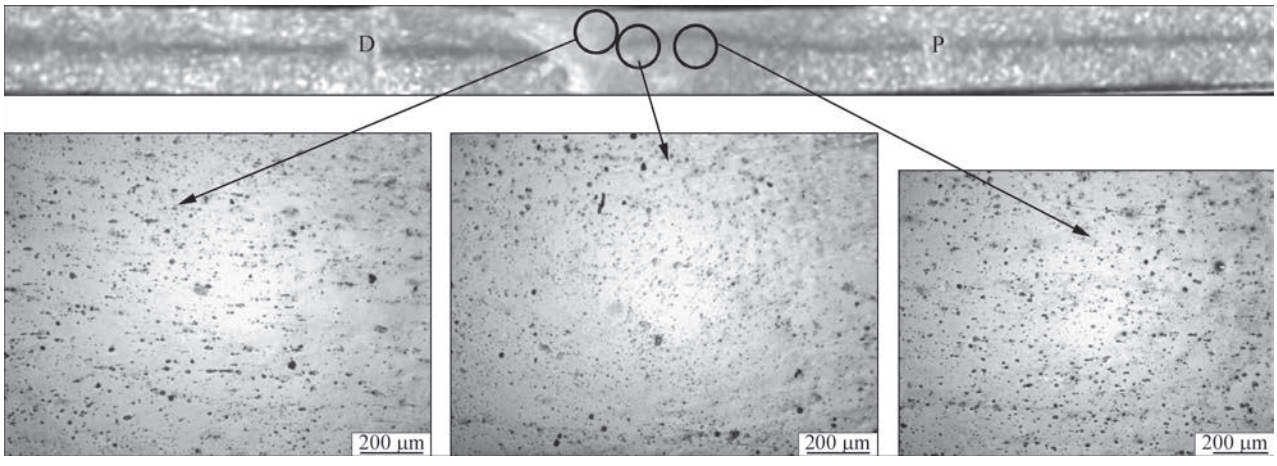

Figure 3. Microstructure of characteristic regions of butt joint of 1.9 mm AMg6M alloy, produced by FSW at sheet position to the left (from the advancing side) along its flanging direction, and to the right (from the retreating side) — across its flanging direction (sheet position: D — along the flanging direction, P — across the flanging direction)

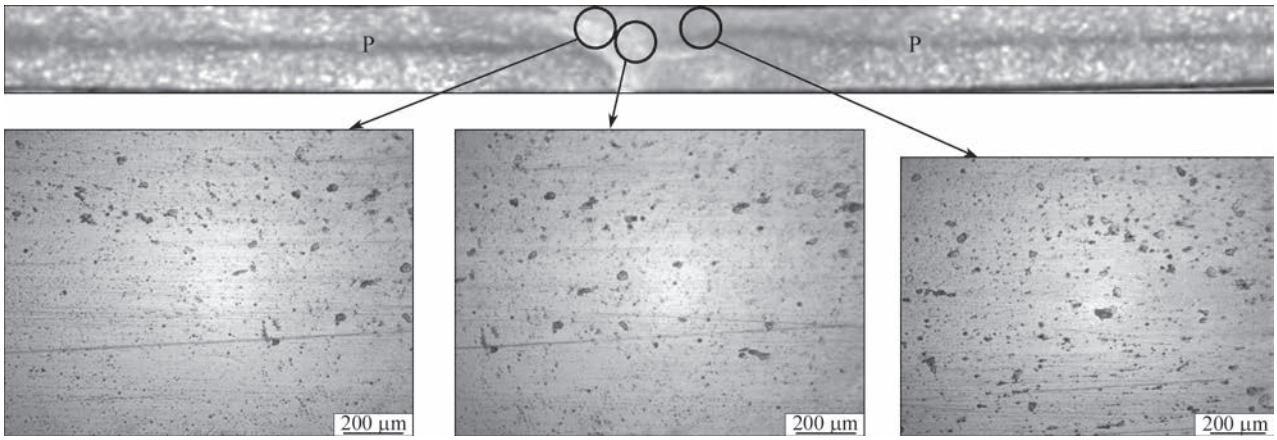

Figure 4. Microstructure of characteristic regions of butt joint of 1.9 mm AMg6M alloy, produced by FSW at both sheets positioned across their flanging direction (sheet position: D — along the flanging direction, P — across the flanging direction)

form, which are oriented along the direction of plasticized metal displacement by the tool working surfaces. Owing to weld formation in the solid phase at FSW, unlike fusion welding, there are no conditions for formation of one of the defects, characteristic for aluminium alloy welded joints, namely concentration of low-melting eutectic inclusions on the weld boundary with the base material (Figures 3, 4). Analysis of overlap joint microstructure also showed formation of a new fine-grained microstructure in the weld nugget, which is independent of the features of the metal initial structure, from which it formed. Now, in the zones of weld transition to base material grain deformation takes place, as a result of thermomechanical impact (Figures 5, 6).

Figures 7, 8 shows the microstructure of the characteristic regions of welded joints, produced at FSW of fillet joints by making butt and overlap-butt welds. Analysis of the microstructure of fillet joints produced by butt welds, showed that similar to welding of sheet butt joints, a weld nugget with a fine-crystalline structure forms in the weld central part, as a result of intensive plastic deformation of metal. The size of grains, having a practically globular shape, is not higher than 4–5 μm, and that of dispersed phase inclusions is ≤ 1 μm. In the thermomechanical impact zone on the boundary of weld-to-base material transition, both from the side of the thin (1.9 mm) and from the side of the thick (12.0 mm) sheets, in addition to fine grains, somewhat larger (6–7 μm) elongated grains form, which are oriented along the direction of displacement of plasticized metal by the tool working surfaces. Here, in the HAZ, where the metal was not exposed to deformational impact, the maximum size of its grains is on the level of 10–15 μm. In welding of fillet joints by overlap-butt welds no essential differences in the microstructure of its characteristic subzones is observed (see Figure 8).

For the studied AMg6M alloy the ultimate strength of base metal for samples cut out along the sheet flanging direction, is on the level of 370 MPa, and for those cut out across this direction, it is on the lev-

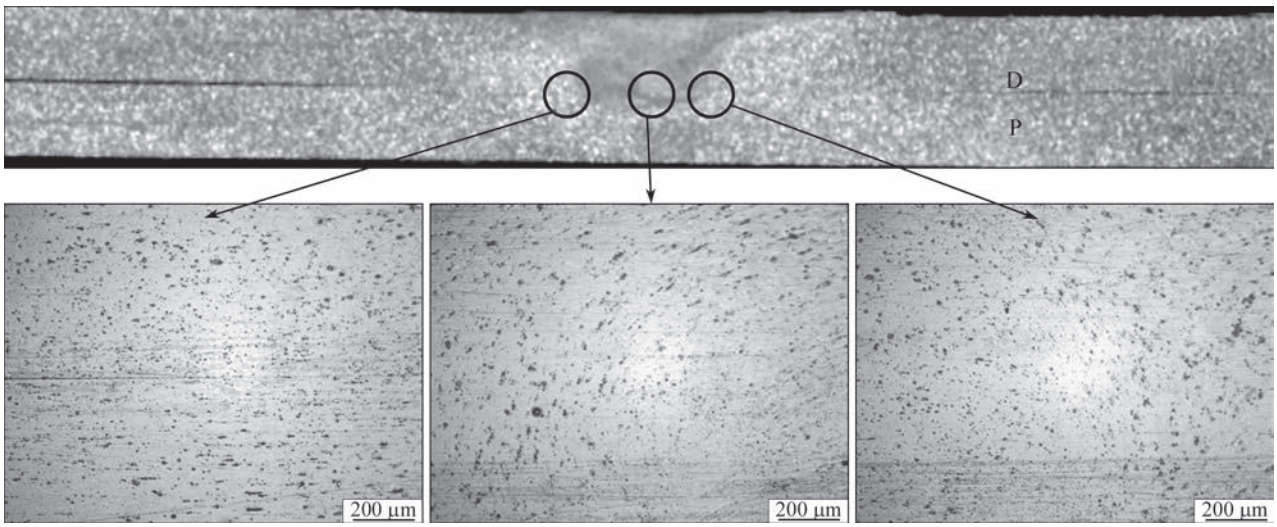

Figure 5. Microstructure of characteristic regions of overlap joint of 1.9 mm AMg6M alloy, produced by FSW at weld orientation along their flanging direction on the upper sheet, and across their flanging direction on the lower sheet (sheet position: D — along the flanging direction, P — across the flanging direction)

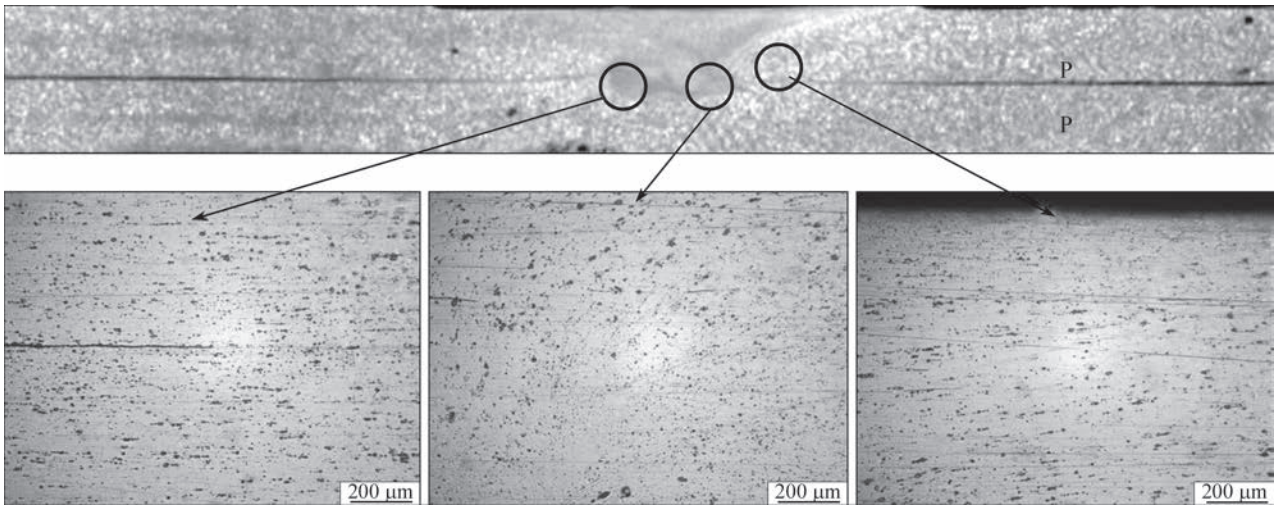

Figure 6. Microstructure of characteristic regions of overlap joint of 1.9 mm AMg6M alloy, produced by FSW at weld orientation across sheet flanging direction on the upper and lower sheets (sheet position: D — along the flanging direction, P — across the flanging direction)

el of 359 MPa. As a result of the conducted studies it was found that the ultimate strength of samples of butt joints, in which the sheet flanging direction is normal relative to the weld orientation, both from the advancing and from the retreating side, is on the level of 343–350 MPa. At static tension of such samples they fail through the base material from the advancing or the retreating side, or on the boundary of the thermomechanical impact zone and the heat-affected zone from the retreating side (Figure 9, *a–c*).

When testing samples of butt joints, where sheet flanging direction is normal from the advancing side,

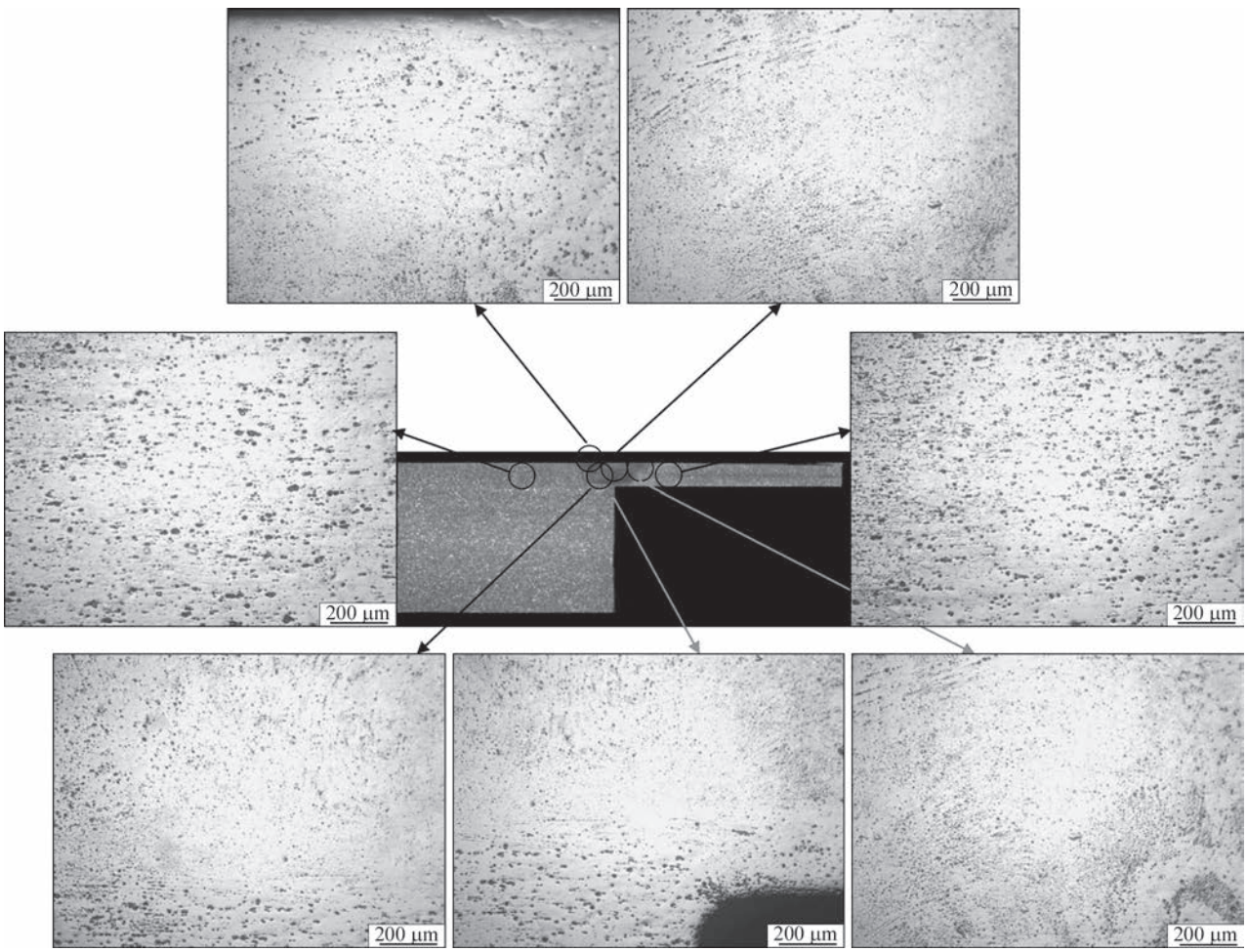

Figure 7. Microstructure of characteristic regions of fillet joint of 1.9 mm AMg6M alloy, produced by FSW by a butt weld with 12.0 mm sheet placed from the advancing side

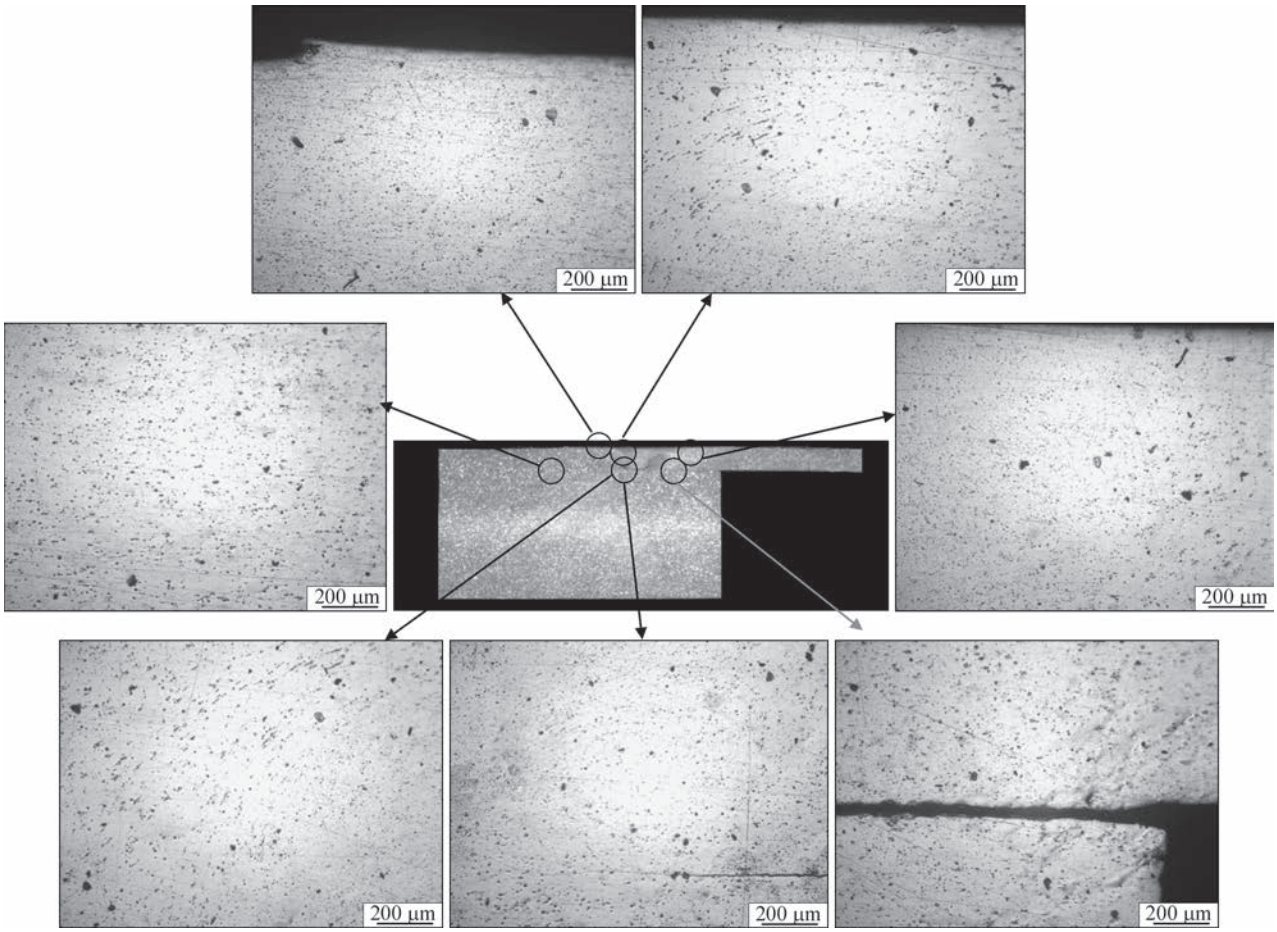

Figure 8. Microstructure of characteristic regions of fillet joint of 1.9 mm AMg6M alloy, produced by FSW by an overlap-butt weld with 12.0 mm sheet placed from the advancing side

and parallel relative to weld orientation from the retreating side, the ultimate strength is somewhat lower and it is on the level of 336–343 MPa. This is due to the fact that the samples fail through the base metal or on the boundary of the thermomechanical impact zone and the heat-affected zone from the retreating side, where the forces at their stretching are directed normal to the sheet flanging direction, and the base

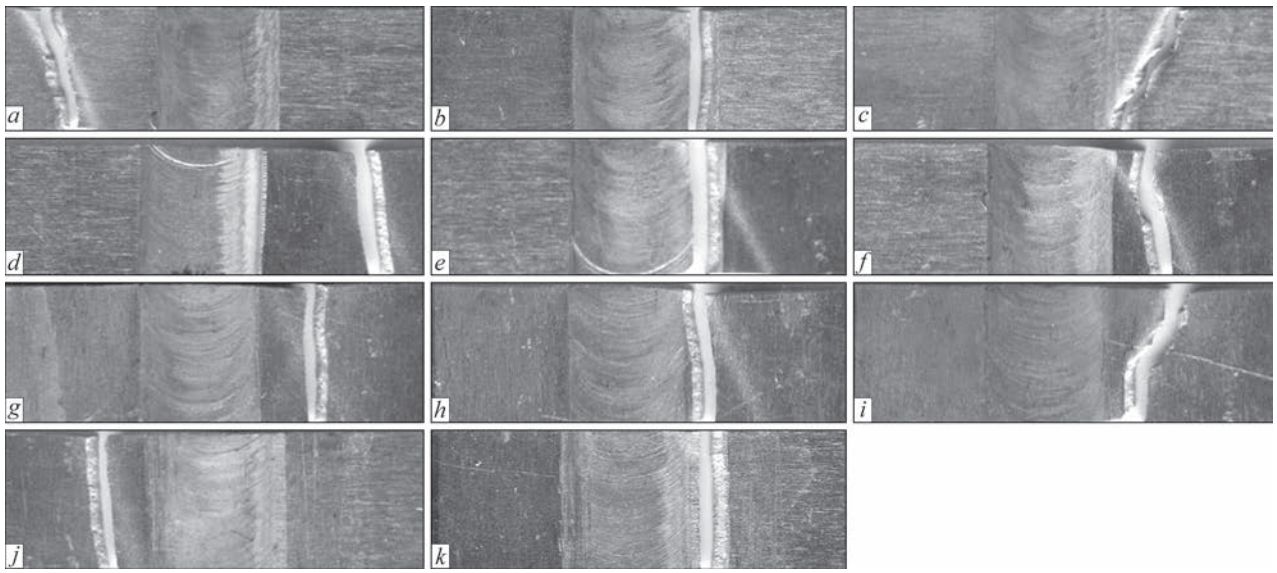

Figure 9. Appearance of the face of broken samples of butt joints of 1.9 mm AMg6M alloy produced by FSW at different arrangement of sheets relative to weld orientation: *a–c* — from the advancing side and from the retreating side their flanging direction is normal relative to weld orientation; *d–f* — from the advancing side, their flanging direction is normal and from the retreating side — parallel to weld orientation; *g–i* — from the advancing side and from the retreating side their flanging direction is parallel to weld orientation; *j*, *k* — from the advancing side their flanging direction is parallel and from he retreating side it is normal to weld orientation

Table 1. Ultimate strength of base metal and welded joints of AMg6M aluminium alloy made by FSW

Sample orientation relative to sheet flanging direction		Ultimate strength, MPa
Base metal	Along the sheet flanging direction	368–372
	Across the sheet flanging direction	357–361
Butt welded joint	From the tool advancing side and from the retreating side sheet flanging direction is normal to weld orientation	343–350
	From the advancing side the sheet flanging direction is normal, and from the retreating side it is parallel to weld orientation	336–343
	From the advancing and the retreating side sheet flanging direction is parallel to weld orientation	335–340
	From the advancing side the sheet flanging direction is parallel, and from the retreating side it is normal to weld orientation	338–344
Fillet welded joint	From the tool advancing side and from the retreating side sheet flanging direction is normal to weld orientation	342–347
Overlap welded joint	From the tool advancing side and from the retreating side sheet flanging direction is normal to weld orientation	337–341

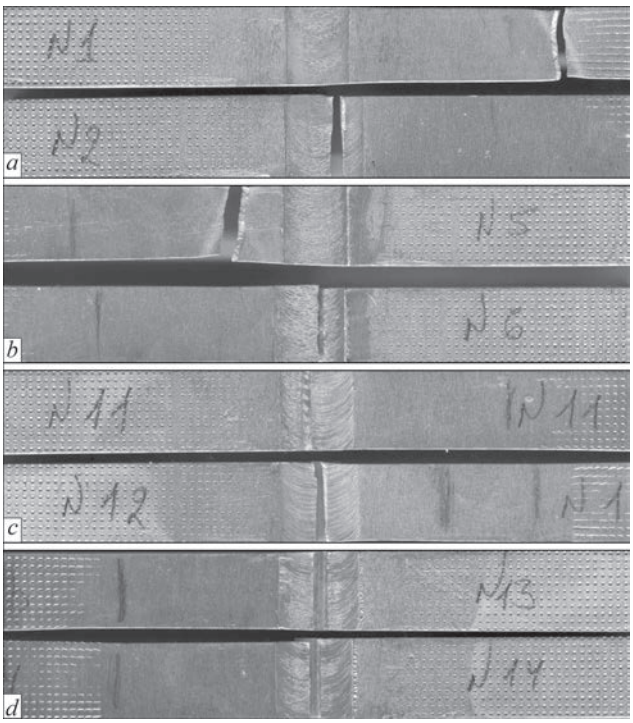

Figure 10. Appearance of the face of broken samples of fillet joints of AMg6M alloy produced by butt (*a*, *b*) and overlap-butt (*c, d*) welds with 12.0 mm sheet placed from the advancing (*a*, *c*) and the retreating side (*b*, *d*)

metal strength is lower under such conditions (Figure 9, *d–f*).

For butt joints, where the sheet flanging direction is parallel to weld orientation both from the advancing and the retreating sides, the ultimate strength is equal to 335–340 MPa. This parameter is close by its value to the previous variant of sheet arrangement, as the samples fail in the same zones, and base metal strength at such an arrangement of the sheets is lower (Figure 9, *g–i*).

Now, if from the advancing side the sheet flanging direction is parallel, and from the retreating side it is normal relative to the weld orientation, the ultimate strength of samples of such joints is on the level of 338–344 MPa. At their static stretching, the samples fail through the base material from the advancing side, where the forces are oriented normal to the sheet flanging direction, or on the boundary of the thermomechanical impact zone and heat-affected zone from the retreating side (Figure 9, *j*, *k*).

Testing of samples of fillet joints made by butt welds showed that at their static stretching, fracture usually runs through the base metal (sometimes, in the thermomechanical impact zone in the area of weld-to-base metal transition), irrespective of the position of the sheets being welded (Figure 10 *a*, *b*). Here, the ultimate strength of such welded joints is in the range of 342–347 MPa.

Fillet welded joints, made by overlap-butt welds, at static stretching fail in the thermomechanical impact zone in the area of weld metal fusion with base metal (Figure 10 *c*, *d*) and their ultimate strength is on the level of 337–341 MPa.

The generalized results from experimental data of studying the strength of base metal and welded joints of AMg6M aluminium alloy, produced by FSW, are given in the Table 1, depending on the sheet flanging orientation.

CONCLUSIONS

1. At FSW of butt, overlap and fillet joints of AMg6M aluminium alloy a weld nugget with a fine-crystalline

structure forms in the central part of the welds as a result of intensive plastic deformation of the metal. The size of the grains having a practically globular shape, is not more than 4–5 μm, and that of phase precipitates is ≤ 1 μm. In the thermomechanical impact zone on the fusion boundary of the weld and base materials, partial metal deformation takes place, so that in addition to fine grains, somewhat larger (6–7 μm) elongated grains form, oriented along the direction of plasticized metal displacement by the tool working surfaces. Here, in the HAZ, where the metal was not exposed to deformational impact, the maximal size of its grains is on the level of 10–15 μm.

2. The ultimate strength of samples of butt joints and fillet joints produced by butt and overlap-butt welds is on the level of 335–350 MPa at their static stretching, and it is practically independent of the position of the sheets being welded, either from the advancing side or the retreating side or weld orientation relative to their flanging direction. Here, butt joint samples fail mainly through the base metal, or on the boundary of the thermomechanical impact zone and the heat-affected zone. Samples of fillet joints, produced by overlap-butt welds, fail in the thermomechanical impact zone, and those made by butt welds fail also through the base metal.

REFERENCES

1. Ishchenko, A.Ya., Labur, T.M., Bernadsky, V.M. et al. (2006) *Aluminium and its alloys in modern welded structures.* Kyiv, Ekotekhnologiya [in Russian].
2. Poklyatsky, A.G., Grinyuk, A.A. (2001) Effect of parameters of asymmetric and modulated currents on quality of aluminium alloy welded joints. *The Paton Welding J.*, **7**, 33–36.
3. Poklyatsky, A.G., Ishchenko, A.Ya., Grinyuk, A.A. et al. (2002) Non-consumable electrode argon-arc welding of aluminium alloys with arc oscillations. *The Paton Welding J.*, **2**, 18–22.
4. Shiganov, I.N., Shakhov, S.V., Kholopov, A.A. (2012) Laser welding of aluminum alloys for aviation. *Engineering J.: Science and Innovations*, **6**, 34–50.
5. Defalco, J. (2006) Friction stir welding vs. fusion welding. *Welding J.*, **3**, 42–44.
6. Pietras, A., Zadroga, L., Lomozik, M. (2004) Characteristics of welds formed by pressure welding incorporating stirring of the weld material (FSW). *Welding Inter.*, **1**, 5–10.
7. Ishchenko, A.Ya., Podielnikov, S.V., Poklyatsky, A.G. (2007) Friction stir welding of aluminium alloys (Review). *The Paton Welding J.*, **11**, 25–30.
8. Chionopoulos, S.K., Sarafoglou, CH.I., Pantelis, D.I. et al. (2008) Effect of Tool Pin and Welding Parameters on Friction Welded (FSW) Marine Aluminium Alloys. In: *Proc. of the 3rd Inter. Conf. on Manufacturing Engineering (ICMEN), 1–3 October 2008, Chalkidiki, Greece*, 7–15.
9. Shibayanagi, T. (2007) Microstructural aspects in friction stir welding. *J. of Japan Institute of Light Metals*, **9**, 416–423.
10. Markashova, L.I., Poklyatsky, A.G., Kushnaryova, O.S. (2013) Influence of welding processes on the structure and mechanical properties of welded joints of aluminium alloy 1460. *The Paton Welding J.*, **3**, 18–23.
11. Saad, A.K, Shibayanagi, T. (2007) Microstructure and mechanical properties of friction stir welded similar and dissimilar joints of Al and Mg alloys. *Transact. of JWRT*, **1**, 27–40.
12. Lin, H., Fujii, H., Maeda, M. et al. (2003) Mechanical properties of friction stir welded joints of 1050-H24 aluminium alloy. *Science and Technology of Welding and Joining*, **6**, 450–454.
13. Mori, H., Noda, M., Tominaga, T. (2007) Current state on application of friction stir welding for rolling stock. *J. of Japan Institute of Light Metals*, **11**, 506–510.
14. Kumagai, M., Tanaka, S. (2001) Application of friction stir welding to welded construction of aluminium alloys. *J. of Light Metal Welding and Construction*, **1**, 22–28.
15. Arbegast, W.J. (2006) Friction stir welding after a decade of development. *Welding J.*, **3**, 28–35.
16. Ding, J., Carter, R., Lawless, K. et al. (2006) Friction stir welding flies high at NASA. *Welding J.*, **3**, 54–59.

ORCID

A.G. Poklyatskyi: 0000-0002-4101-2206,
S.I. Motrunich: 0000-0002-8841-8609,
V.E. Fedorchuk: 0000-0002-9929-3231,
I.M. Klochkov: 0000-0001-6490-8905

CONFLICT OF INTEREST

The Authors declare no conflict of interest

CORRESPONDING AUTHOR

A.G. Poklyatskyi
E.O. Paton Electric Welding Institute of the NASU
11 Kazymyr Malevych Str., 03150, Kyiv, Ukraine.
E-mail: pag556a@gmail.com

SUGGESTED CITATION

A.G. Poklyatskyi, S.I. Motrunich, V.E. Fedorchuk, I.M. Klochkov (2023) Strength and structure of butt, overlap and fillet joints of AMg6M alloy produced by friction stir welding. *The Paton Welding J.*, **2**, 10–17.

JOURNAL HOME PAGE

https://patonpublishinghouse.com/eng/journals/tpwj

Received: 14.02.2023
Accepted: 30.03.2023

DOI: https://doi.org/10.37434/tpwj2023.02.03

INVESTIGATIONS OF THE STRUCTURE OF WELDED JOINTS OF POLYMERS USING THE REHBINDER EFFECT

G.M. Korab, M.V. Iurzhenko, M.O. Kovalchuk, L.S. Parshutina, O.M. Chukashkin

E.O. Paton Electric Welding Institute of the NASU
11 Kazymyr Malevych Str., 03150, Kyiv, Ukraine

ABSTRACT

Welds of polymer materials, butt welded with a heated tool, are distinguished by a variety of structural components. Investigations of such welds allow studying the general fundamental processes of structure formation in the formation of welded joints of polymers. In this work, mechanical tests of welded joints of polymer pipes with a local load in the environment of surface active substances and with the use of the Rehbinder effect were carried out. Experimental specimens of pipe joints with a diameter of 63, 90, 110 and 160 mm from PE80 polyethylene were produced in the standard equipment for butt welding with a heated tool on the modes recommended by DBN V.2.5-41:2009. The tests were carried out in accordance with the requirements of the international standard ISO 22088 "Cracking under the influence of the environment" (ESC). The characteristic features of cracks propagation in the tests of the base material and the fusion zone of the weld were investigated. Using optical microscopy, the fracture surfaces of the specimens were investigated immediately after tests and after chemical etching in sulfuric acid solution. It was shown that in the fusion zone, a weakened "blurry" structure of polymer material is formed, which is fractured during a local load.

KEYWORDS: butt welding with a heated tool, supramolecular structure, mechanical tests, fracture surfaces

INTRODUCTION

Supramolecular structure of polymer is very complex and divides for several levels depending on size of the structural elements. The spherulites of size at a level of 10 μm are the main component for crystalline polymers. At the next level there are domains of crystalline-lammellaes of 10–100 nm size. A size of folded lamellaes is evaluated in 10 nm. An elementary folded link forming lammellaes are of 0.1–1.0 nm size limit.

Most of the engineering plastics have in their content various admixtures and fillers, therefore, examination of a material microstructure using light microscope is usually impossible [1]. Visual evaluation of the details of complex supramolecular structure is possible by means of investigation of the typical features of weld fracture under the effect of local mechanical loads [2, 3].

Since the polymers consist of the long flexible molecular chains, they have typical features of the material in a solid state, namely inhomogeneity, non-linearity and time dependence of mechanical properties [4]. Loss of strength by a polymer usually takes place in several steps after sufficient plastic deformations. The following terms are used in the theory of polymer fracture, namely failure, i.e. accumulation of structure defects, fracture — formation of cracks with development of new surfaces and rupture — division of body on separate parts. In other words, gradual loss of strength by polymer material in loading takes place due to expansion of existing and formation of new defects of supramolecular structure. The investigations of crack propagation are used for determination of different types of strength of polymer materials 5]. In this work there were carried out the investigations of strength of base material and welded joints of polymers using mechanical loading with additional stimulation of fracture with the help of surface-active substances (SAS).

The processes of fracture taking place in a solid polymer significantly depend on its physico-chemical interaction with environment. Such organic substances as alcohols, fatty acids, rosins, soaps contain in their molecule composition at the same time hydrophilic and hydrophobic groups and being called surface-active. SAS molecules in contact are intensively adsorbed on a surface of solid body that significantly decreases its surface energy and proportionally reduces body strength [6, 7].

Adsorption decrease of strength of solid bodies was titled as Rehbinder effect [8]. The effect has a versatile nature and observed for any solid materials.

In polymers development of cracks in material takes place through successive rupture of separate macromolecular chains. Crack propagation promotes formation of the new material surfaces which adsorb SAS. The SAS molecules covering the newly formed crack planes neutralize their high energy potential and try to move as close as possible to the very beginning of the crack. Even at absence of surface loads these molecules colliding between themselves create a fracture force F in a crack basis (Figure 1). It can reach significant value in the minimum gaps.

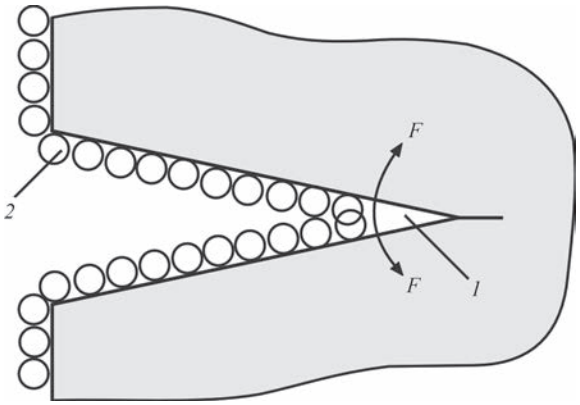

Figure 1. Scheme of SAS effect on crack development in solid body: *1* — crack start; *2* — SAS molecules on surface

There are different procedures being used for generation of local loads and stress concentrators in a polymer specimen. International standard ISO 22088-1 [9] provides the definition of the process of crack formation in polymer material (plastic) which is located in a certain chemical environment and being under the effect of constant stress less than a value of yield strength. This process has a standard name — environmental stress cracking, ESC.

One of the most widespread methods of evaluation of strength to ESC is a bend strip method [10]. A cut is made on a plate from polymer material. It serves as a concentrator for crack initiation. Then the plate is bent in half in the place of cut developing constant mechanical stresses. Bent plates are located in SAS environment and after a while evaluate the number and size of the formed cracks. However, the load in this method is applied asymmetrically and at once for all width of the plate-specimen, therefore, this method is used for testing of base material and for polymer welded joints it is not applicable. The task of this work lies in performance of the comparative tests of strength of base material and weld material as well as evaluation of supramolecular structure of a transition fusion zone in the welded joints of polyethylene pipes.

The segments of the standard polyethylene pipes of 63, 90, 110 and 160 mm diameter designed for construction of gas pipelines made of polyethylene of PE80 grade according to the requirements of DSTU B V.2.7-73–98 were used in work. The pipes of black and yellow colors were used. The section of polyethylene pipes were joined using butt welds on standard equipment for butt welding with a heated tool applying the modes recommended by the standard [13].

METHOD FOR DETERMINATION OF CRACK FORMATION RESISTANCE

Resistance of base material and weld material to crack formation was determined according to a procedure of ISO 22088-4 [11] by means of formation of local

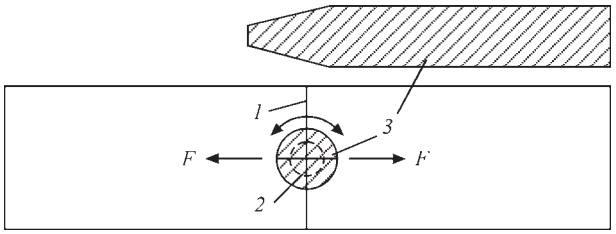

Figure 2. Scheme of initiation of fracture of welded joint using hole and cylinder rod: *1* — weld fusion line; *2* — through hole in specimen; *3* — cylinder rod

loading in a necessary area of a polymer specimen. For this a pin impression method was used, the essence of which is schematically shown in Figure 2. A lamellar specimen with a weld in the middle is cut out from a welded joint. A hole of 3–4 mm diameter depending on specimen size is drilled on a fusion line. A cylinder rod of somewhat larger diameter with a cone tip is impressed in the hole that creates in the specimen a total tensile load F and tangential loads on a hole perimeter f. The works using this method have already been carried out at the E.O. Paton Electric Welding Institute (PWI) for comparison of strength of a butt welded joint of the polyethylene pipes in the different points of butt orbit [12].

For all the tests by ISO 22088-4 procedure there were used a rod with a cone tip varying the relationship of diameters of hole and rod to change of a value of stresses in the specimen (Figure 2). After immersion of the rod in the hole and appearance of local load the specimens with welds were placed in a SAS water solution (grade OP-7) at up to 80 °C temperature and hold there from several minutes to hours till crack appearance. The joints from black and yellow pipes were made in order to ease the study of weld fusion line. In most of the cases at local initiation of stresses using a rod the welded joints fracture close to a fusion line (Figure 3). The difference in pipe colors provides the possibility for good evaluation of belonging of polymer material to one or another pipe part on the fracture surfaces.

The photos of specimens were made using digital camera Nikon D350 (NIKON Corp, Tokyo, Japan).

The magnified images of the surfaces of specimens were made by the same camera imbedded in a

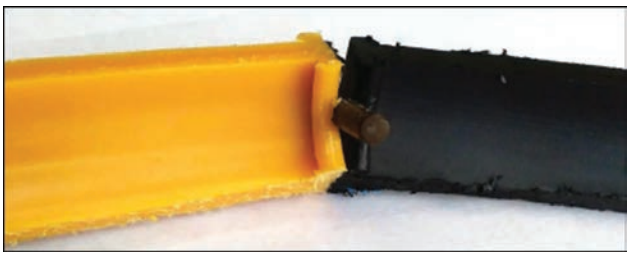

Figure 3. Specimen of butt welded joint of polyethylene pipes fractured after testing

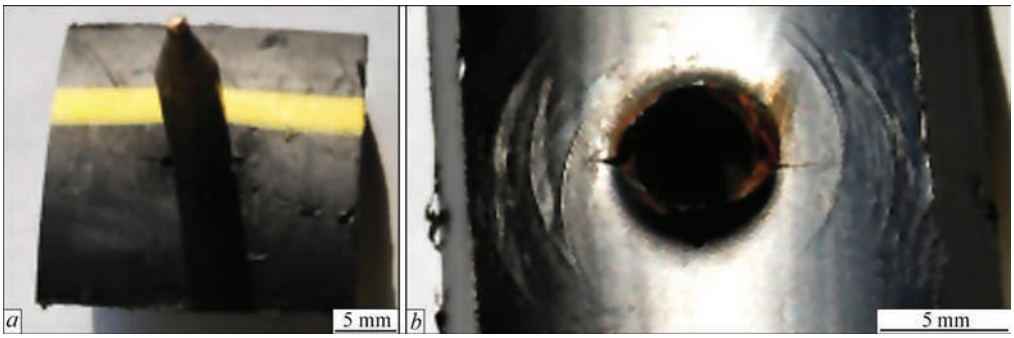

Figure 4. Cracks in specimens from base material of polyethylene pipes of gas grades PE80 with wall thickness 10 mm on outer (*a*) and inner pipe surface (*b*)

light polarizing microscope Versamet-2 (UNITRON, New-York, NY, USA).

INVESTIGATION RESULTS

Polyethylenes of pipe grades PE80 and PE100 are sufficiently ductile materials with high crack resistance. Therefore, the small cracks in testing of base metal of polyethylene pipes appear only after holding under stress in SAS environment for several hours (Figure 4). The cracks in the base material are of small length and propagate on both sides of the stress source along a straight line. A direction of crack on the outer surface of a pipe exactly matches with a longitudinal axis of the pipe that indicates some structural organization of material. Cracks on the inner pipe surface appear in a transverse direction relatively to the axis direction, they do not have through nature and form on the surfaces of specimens in the places where stresses and effect of SAS are the biggest.

The fracture surfaces of pipe specimen of PE80 polyethylene with outer diameter 110 mm and wall thickness 10 mm (Figure 5) demonstrate complete cohesion nature of the welded joint, i.e. the fragments of material of one element of the joint are present on the fracture surface of another one. The specimen of welded joint of pipes of 160 mm diameter and wall thickness 14.6 mm fractured inhomogeneously during testing (Figure 6). The part of specimen fractures exactly along the fusion surface, another part demonstrates a joint nature of crack propagation along the weld and base material of the pipe. At significant pipe wall thickness the direction of crack propagation can change and deviate from a failured fusion zone.

Analyzing a magnified image of the crack formed in fracture of the welded joint (Figure 7) it is possible to judge a nature of a transition structure being formed after cooling of molten metal inside the weld. A solid spherulitic structure along a delimitation line is not observed. Obviously, the monoliths of two parts are joined through the finer arranged structures of fibrils, folded domains or micelles. Therefore, a line of joining in a transition structure appears to be the weakest place. Tension of the supramolecular structures (Figure 7, below) that hold joint elements starts at local loading. It takes place slowly under standard conditions and sufficiently quick in SAS environment. Tensile structures reach a strength limit and tear provoking further crack propagation. If such failured structures in the weld have local nature, the crack ruining them stops or changes the direction meeting stronger structural areas. In other case, the transition structures are uniformly distributed along the whole area of butt orbit, therefore, fracture takes place in this plane or its vicinity. Only the remnants of torn transition structures are observed on the fracture surface (Figure 7, upper part).

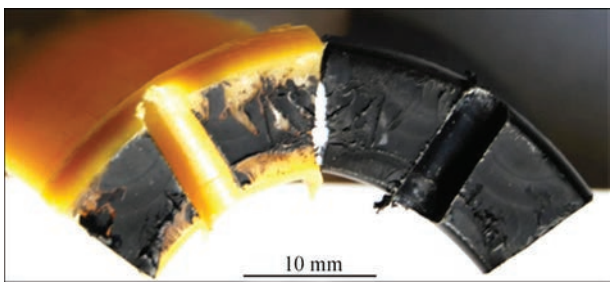

Figure 5. Fracture surfaces of welded joint of pipes from PE80 of 110 mm diameter and wall thickness 10 mm

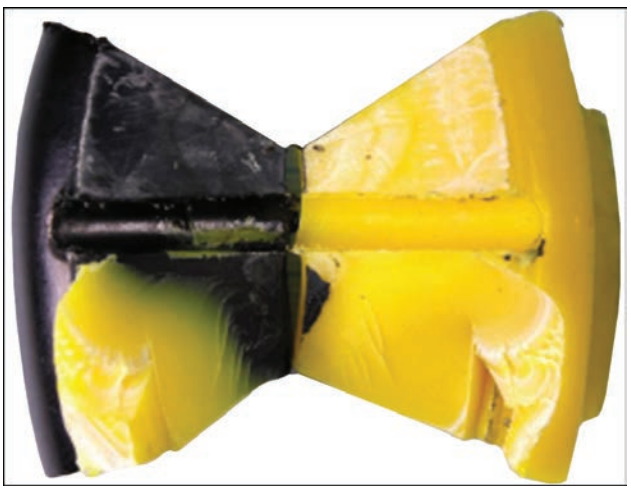

Figure 6. Fracture surfaces of welded joint of pipes from PE80 of 160 mm diameter and wall thickness 14.6 mm

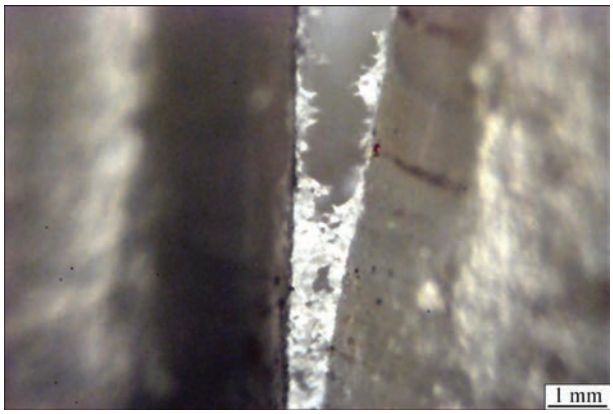

Figure 7. Crack propagation at fracture of welded joint of polyethylene pipes, ×10

The fusion line of two pipe specimens of different color polyethylene (Figure 8) demonstrates partial interpenetration of the supramolecular domains of black and yellow polyethylene (white on the photo). An interface profile has a non-uniform jagged nature, probably formed under effect of random factors. Such a profile apparently can not be a consequence of a joint flow of melts of two parts being joined under effect of upset force. A transition zone demonstrates the sharp elongated elements of black and yellow material which mutually pass through the fusion line "diluting" it. It is logical to assume that the deeper such interpenetration of the materials in weld formation, the stronger formed welded joint will be. The single driving force of such interpenetration is a heat movement of the segments of macromolecular chains at elevated temperature. The velocity of such movement is limited and dramatically drops with temperature decrease. Therefore, formation of sound welded joint requires staying of the material in a fusion zone for some time at elevated temperature.

Information on nature of microstructure of a polymer can be obtained by means of examination of their fracture surfaces. Fracture of any material is formation of the new surfaces. In given case a fracture of the specimens of welded joints of polyethylene pipes is a process taking place relative to slow propagation of a crack plane from the place of its initiation and nucleation. A polyethylene of high density is a semi-crystalline material. In it the areas of ordered and amorphous material border each other on a supramolecular level. The amorphous areas and intermolecular cavities also accumulate different admixtures and oligomers. Crack propagation takes place directly on failured, amorphous areas, thus allows revealing material structure.

The fracture surfaces were examined using the light microscope on the black specimens since dark material allow obtaining more contrast image. A typical example of the directed structural formations in a

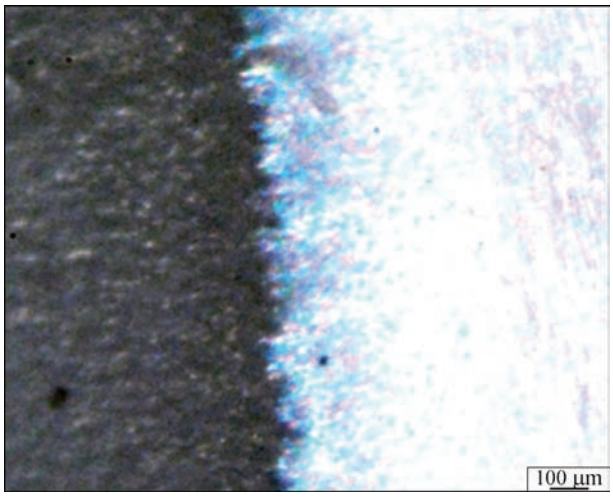

Figure 8. Line of welded joint of polyethylene pipes of different colors at ×20 magnification

bulk of polymer material is given on Figure 9. A series of objective and random factors is superimposed on the process of crack propagation. Therefore, on the fracture surface we can observe the elongated curvilinear structures, which are demonstration of a regular spherulitic structure and a randomly located area, formed due to crack "wandering" in the sections with relatively isotropic structure.

A spherulitic structure of a crystalline polymer is formed non-uniformly depending on heat conditions at a level of micron sizes and presence of necessary amount of crystallization nuclei. During formation of the ordered structures, low-molecular substances are displaced in the areas between them. Randomly formed spherulites in turn form the supracrystalline structures, which in fracture form a surface similar to double-sided lamellaes only of larger scale. It is well observed on Figure 9 that these lines are the double-sided or semi-round formations with deep, sharped to bottom cavities between them. It is necessary to take into account that such a surface was formed not as a result of some special treatment or etching, but due to free process of material fracture. Such a surface indicates significant physical inhomo-

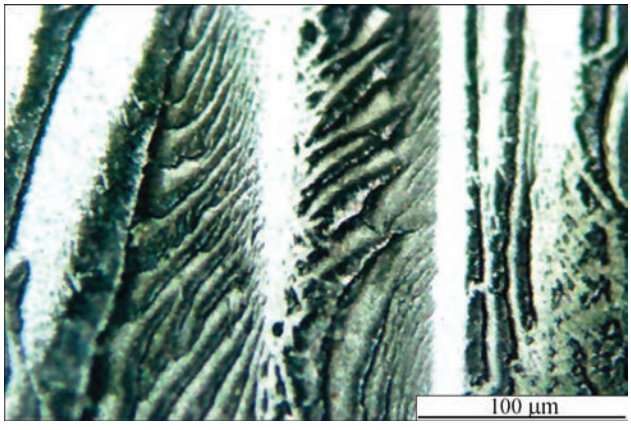

Figure 9. Fragment of fracture surface with ×10 magnification

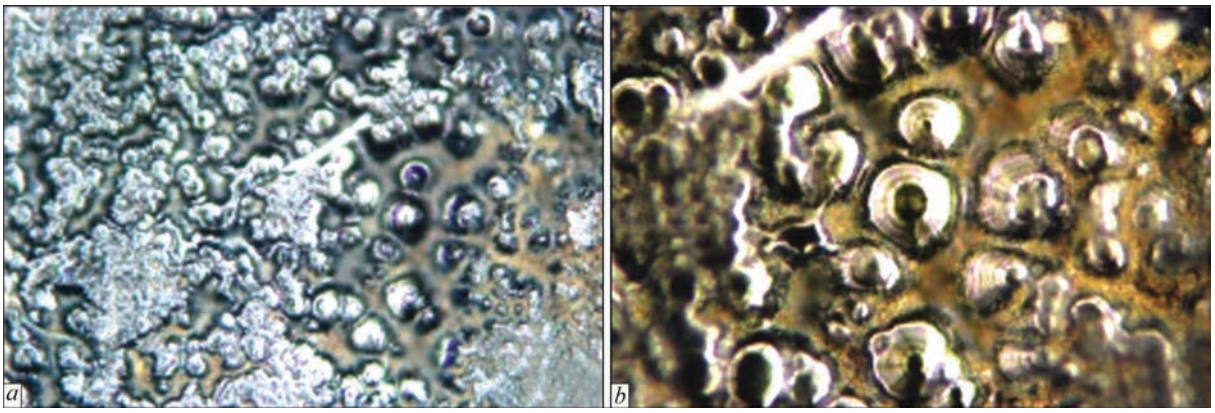

Figure 10. Area of ordered spherulite structures, magnification: *a* — ×10; *b* — ×20

geneity of the material, in which areas of strong and failured material alternate in orderly manner.

The double-sided ordered formations border with more extended elongated linear areas on the surface. Obviously, in these areas the material on a microlevel created less resistance to crack propagation and fracture took place linearly remaining on the surface the traces made as "under the ruler". There are also areas with disordered structure of the surface, which, obviously, correspond similar areas of structure in a bulk of material. Depressions in the surface between double-sided structures actually have uniform homogeneous structure. Obviously, this is a consequence of the fact that the failured areas between the crystalline areas have own certain minimum size, which appear on the surface in a form of filamentary formations of almost similar width. It can be seen that such nature of a surface is present only in some certain places, therefore, it appear only at match of several necessary factors in the process of crack propagation.

Etching of the specimen in a sulfuric acid solution helps clearly reveal crystalline and amorphous areas on the surface of polymer. The amorphous failured areas dissolve significantly quicker than the crystalline ones, therefore appear on the surface in form of depressions at a background of higher ordered areas. Fracture surfaces of the specimens were subjected to etching and examined using light microscope (Figure 10).

The areas of surface with linear ordered structure almost do not undergo the changes after etching. Obviously, these are areas with the highest level of crystallinity and percent of amorphous phase here is small. Therefore, after etching the surface contains only narrow longitudinal bands that were formed after removal of small amount of failured material. The zones of spherulite structure are characterized with great non-uniformity of surface and presence of round-shaped formations. Since crystallization of spherulites is non-uniform, they accumulate in some places forming supracrystalline associations that consist of rounded objects. Admixtures, oligomers and other amorphous material in small quantity remain in spherulites content, but they are mainly displaced out of the borders of ordered zones, forming, in turn, amorphous associations, sometimes of sufficiently large size.

Figure 10, *a* shows that structure of the surface is non-uniform and changes from one area to another. Crystalline areas of irregular shape are obviously a demonstration of the associations of spherulites which united in one large formation. Not by chance, one of the most realistic theories of polymer structure, namely paracrystalline Hosemann [14] model describes its structure as a moving matrix with crystalline folded formations floating in an amorphous phase located between them. Separate convex rounded objects can be the remains of torn molecular domains — fibrils which were formed in the process of crack formation. Amorphous material occupies in some regions sufficiently large areas, therefore, in these zones the polymer material has decreased strength that can serve a direction for crack propagation. The photo of the largest scale (Figure 10, *b*) demonstrates the ordered formations of rounded shape, which after etching got a typical cone-like shape, inside which a finer layerwise structure similar to spherulite is observed. Chemical etching agent removed from these objects all amorphous loops of chains and through molecules remaining only crystalline phase of spherical shape.

It is necessary to note that the examined welded joints are mechanically full-strength according to tensile test under [12]. In such a way, regardless the fact that the microstructure of polymer material is non-uniform enough, a failure zone is formed along the fusion surface, but on macrolevel it is possible to assume that the material of welded joint is statistically isotropic. A semi-crystalline transition zone is formed in a zone of fusion of butt weld. It obviously consists of fragments of macromolecules and clusters that by a thin layer join a monolithic spherulite structure of base material.

CONCLUSIONS

1. There was carried out a crack resistance testing of base material and welded joints of polyethylene pipes according to the requirements of International Standard ISO 220088-4 using the Rehbinder effect.

2. A nature of crack propagation in a base material indicates some structural organization of polyethylene in pipe longitudinal direction. On external pipe surface the direction of crack matches exactly with its longitudinal axis. In the welded joints of polyethylene pipes the cracks are formed along the fusion surface or in vicinity to it.

3. A fracture nature shows that the solid spherulite structure is absent along a fusion line, and failured "diluted" structure of polymer material is formed in this zone by mutual penetration of fragments of molecules. The magnified images of the fracture surface of welded joints demonstrate the disordered randomly located areas as well as fragments of regular spherulite structure that indicate "wandering" of a crack in the region of failured fusion zone.

REFERENCES

1. (2018) *Welding and gluing of plastics:* Reference Book. Ed. by B.E. Paton. Kyiv, Naukova Dumka [in Ukrainian].
2. Ward, I.M., Sweeney, J. (2012) *Mechanical properties of solid polymers*. 3rd Ed. Wiley.
3. Kulak, M.I. (2002) *Fractal mechanics of materials*. Moscow, Vysshaya Shkola [in Russian].
4. Demchenko, V., Iurzhenko, M., Shadrin, A. et al. (2017) Relaxation behavior of polyethylene welded joints. *Nanoscale Research Letters*, **12**, 280–285. DOI: https://doi.org/10.1186/s11671-017-2059-z
5. Buketov, A., Brailo, M., Yakushchenko, S. et al. (2019) Investigation of tribological properties of two-component bidisperse epoxy-polyester composite materials for its use in the friction units of means of sea transport. *Periodica Polytechnica Mechanical Engineering*, 63(**3**), 171–182. DOI: https://doi.org/10.3311/PPme.13161
6. Ibeh, C.C. (2011) *Thermoplastic materials: Properties, manufacturing methods and applications.* CRC Press, Boca Raton.
7. Chetvergov, V.A. (2002) *Physical principles of reliability. Lectures.* Omsk, OGUPS [in Russian].
8. Volynskii, A.L., Bakeev, N.F. (2013) Regularities of the Rehbinder effect in polymers. Review. *Prot. Met. Phys. Chem. Surf.*, **49**, 493–509. DOI: https://doi.org/10.1134/.
9. *ISO 22088-1:2006: Plastics — determination of resistance to environmental stress cracking (ESC).* Pt 1: General guidance.
10. *ISO 22088-3:2006: Plastics — determination of resistance to environmental stress cracking (ESC).* Pt 3: Bent strip method.
11. *ISO 22088-4:2006: Plastics — determination of resistance to environmental stress cracking (ESC).* Pt 4: Ball or pin impression method.
12. Mineev, E.A., Repa, V.P. (1989) *To problem of investigation of welded butt joint strength from polyethylene pipes.* Kyiv, PWI [in Russian].
13. *Minregionbud* of Ukraine (2010) DBN V.2.5-41: 2009. *Plumbing installations and constructions. External networks and facilities. Gas pipelines from polyethylene pipes.* Pt 1: Design. Pt 2: Construction. Kyiv, SE Ukrarkhbudinform [in Ukrainian].
14. Hosemann, R. (1982) Dependence of the change in the free enthalpy on the lattice number with the formation of microparacrystals. *Colloid and Polymer Sci.*, **9**, 864–870.

ORCID

G.M. Korab: 0000-0001-8030-1468,
M.V. Iurzhenko: 0000-0002-5535-731X,
M.O. Kovalchuk: 0000-0003-2161-643X

CONFLICT OF INTEREST

The Authors declare no conflict of interest

CORRESPONDING AUTHOR

M.V. Iurzhenko
E.O. Paton Electric Welding Institute of the NASU
11 Kazymyr Malevych Str., 03150, Kyiv, Ukraine.
E-mail: 4chewip@gmail.com

SUGGESTED CITATION

G.M. Korab, M.V. Iurzhenko, M.O. Kovalchuk, L.S. Parshutina, O.M. Chukashkin (2023) Investigations of the structure of welded joints of polymers using the Rehbinder effect. *The Paton Welding J.*, **2**, 18–23.

JOURNAL HOME PAGE

https://patonpublishinghouse.com/eng/journals/tpwj

Received: 02.01.2023
Accepted: 30.03.2023

DOI: https://doi.org/10.37434/tpwj2023.02.04

DETONATION COATINGS BASED ON TiAl INTERMETALLICS WITH ADDITIONS OF NON-METALLIC REFRACTORY COMPOUNDS

A.L. Borysova, A.I. Kildii, T.V. Tsymbalista, M.A. Vasylkivska

E.O. Paton Electric Welding Institute of the NASU
11 Kazymyr Malevych Str., 03150, Kyiv, Ukraine

ABSTRACT

The results of producing and examination of structure and phase composition of detonation coatings from composite powders (CP) based on TiAl intermetallics and non-metallic refractory compounds (B_4C, BN, SiC, Si_3N_4) are presented. Detonation spraying with CP was carried out using the automatic detonation complex "Perun-S". As working gases, the mixture "propane–butane–oxygen" and as diluent and transporting gas air were used. CP for detonation spraying was produced by the method of mechanochemical synthesis (MChS) with a subsequent conglomeration. The size of CP particles was 40–80 μm. It was revealed that the main changes in the phase composition of detonation coatings as compared to the source CP consist in the appearance of a large number of oxide phases; in the composition TiAl–B_4C–TiO_2, Ti_3O_5; TiAl–BN–Ti_3O_5, TiO, TiO_2; TiAl–SiC–TiO_2, Ti_3O_5, SiO_2; TiAl–Si_3N_4–TiO_2, TiO, SiO_2. The most dense and homogeneous structure was obtained in the coatings with CP TiAl–SiC i TiAl–Si_3N_4.

KEYWORDS: Ti–Al system intermetallics, non-metallic refractory compounds, detonation coatings

INTRODUCTION

Due to low density, high specific strength, good mechanical properties at elevated temperatures and resistance to environmental influence, TiAl intermetallics are already used for some components of the automotive and aircraft industry, including for turbochargers or low-pressure turbine blades. However, some drawbacks inherent in TiAl alloys, such as low plasticity and low impact toughness are still inhibiting their wider use as a bulk material. On the other hand, TiAl can be used as a protective coating, for example, for titanium alloys. The main advantages of TiAl coatings consist in the fact, that they have a density lower than MCrAlY alloy coatings, good compliance with titanium alloys in terms of thermal and mechanical properties, as well as the ability to form a strong adhesion with a metal base due to interdiffusion at a lower tendency to brittle phase formation. In addition, adding alloying elements can reduce the rate of oxidation and improve the mechanical properties of TiAl binary alloy. To provide TiAl alloy with a high strength, rigidity and wear resistance SiC, TiB_2, B_4C, TiC, Al_2O_3, etc. are used [1–4].

TiAl-based coatings can be produced in several ways, among which thermal spraying [5, 6] and aluminizing have become most widespread [7].

Among the different methods of thermal spraying of TiAl coatings, most studies were focused on plasma, high-velocity oxygen fuel (HVOF), cold, detonation and electric arc surfacing.

As for the coatings produced by detonation spraying, the research data are mainly referred to TiAl [8–13], Ti_3Al [12, 14] and TiAlCr [15].

In [10, 11, 14], in addition to intermetallics, in the coatings small amounts of titanium carbide, nitride and oxide were found. These secondary phases are located on the boundaries or inside the lamellas, depending on the mechanism of formation. The formation of such inclusions of the secondary phase is sometimes carried out consciously, as they provide or enhance the specific characteristics of coatings. For example, titanium nitride was included in the composition of TiAl-coatings to increase the tribological properties of these coatings [14]. Titanium aluminide coatings deposited using hydrogenated titanium [16] was distinguished by a higher hardness, heat resistance and oxidation resistance as compared to the coatings deposited from the source titanium aluminide [12]. The process of detonation spraying can be used to produce nanostructured alumotitanium coatings with a higher microchardness than appropriate plasma coatings. Producing multilayer alumotitanium coatings from conventional and nanostructured powders with alternating layers from partially molten nanostructural material are presented in [11]. In [14] the results of studying the composition of the coatings produced by the method of detonation spraying from Ti_3Al powders in environments of different chemical composition are presented by changing the ratio of O_2/C_2H_2. In these coatings, along with Ti_3Al, TiN and Ti_2N were revealed, which are formed as a result of the reaction of heated particles with nitrogen used to transport the powder. In addition, the studies showed that in the conditions of detonation spraying, a strong oxidation of Ti_3Al occurs, which contributes to the loss of aluminium.

In [11, 12] the authors revealed that from the mechanoalloyed Ti powder, 50 at.% Al a ceramic coating based on Al_2TiO_5 compound can be produced by the oxidizing

effect of the working gas environment on the powder. Titanium aluminide coatings based on TiN inclusions can be formed at the influence of the working gas environment (air, nitrogen) on the powder. At the same time, when using cast TiAl (γ) powder, its phase composition is inherited by the coating. Thus, the coatings produced from mechanically alloyed and cast powders are different both in structure and phase composition. The use of powders produced by mechanoalloying allows not only to vary the phase composition of coatings due to a high chemical activity of a nanostructural X-ray amorphous sprayed material, but also provides new opportunities for creating the optimal coating structure.

The aim of the work was to study the processes of coating formation during spraying by detonation method from composite powders based on TiAl intermetallics with additions of non-metallic refractory compounds (B_4C, BN, SiC and Si_3N_4).

CHARACTERISTICS OF SOURCE MATERIALS AND RESEARCH PROCEDURE

As the source materials to produce coatings by the method of detonation spraying, TiAl intermetallics powder was used containing (wt.%): 62.5 Ti and 37.5 Al (T65Yu35) and composition powders (CP) based on it with the introduction of non-metallic refractory compounds (NRC) such as B_4C, BN, SiC, Si_3N_4 into their composition.

The composite TiAl/NRC powders were produced by the method of mechanochemical synthesis (MChS) in the high energy reactor "Activator 2SL" at 1.5 h of processing. The technology of producing CP of this type is described in detail in [17]. For powder conglomeration, polyvinyl alcohol (PVA) in the amount of 3 % was used.

To study the source powders and sprayed coatings, the methods of metallographic, X-ray structural phase and microdurometric analysis with the construction of variational curves of microhardness were used.

SELECTION OF DETONATION SPRAYING MODE

The coatings were sprayed in the detonation installation "Perun-S". As working gases, a mixture of "propane–butane–oxygen", and as a diluent and transporting gas air were used.

When choosing a detonation spraying mode, a series of experiments was performed with an assessment of the effect of the degree of filling the barrel of a detonation installation with a working gas on the quality of coating, determining the optimal spraying distance, optimal process cyclogram, as well as the consumption of transporting gas and the thickness of the coating, which is formed in a one cycle.

To study the effect of the degree of filling of the barrel on the quality of coatings, the air consumption in the mixture (from 0.4 to 1.15 m^3/s) was changed at a constant ratio of working gases (propane–butane and oxygen) consumption being 1:3 and a distance of spraying of 100 mm, which corresponds to the change in connection with this degree of filling the barrel from 58.3 to 76 %. The most optimal ratio for producing quality coatings was the ratio of working gases (propane-butane+oxygen+air) being 1:3, 1:1.3 for spraying coatings from Ti–Al powder with the particles size of 40–100 μm and the degree of filling the installation barrel being 64 %.

When changing the spraying distance, the 4 distances from the muzzle barrel of the installation to the base with an interval of 40 mm (70, 110, 150 and 190 mm) was chosen. It was found that during spraying at a distance of 70 mm, the coating is dense with a clearly defined border, but both the base and the coatings have temper colors, probably caused by overheating of the base and the coating. In addition, at a small spraying distance, the base may deform and in the coating microcracks may appear under the action of thermal stresses. During spraying at a distance of 110 mm, the coating is dense, the powder particles of all sizes are involved in the formation of the coating: in small-sized particles the temperature and velocity have not been already reduced, the border of the coating is slightly blurred, the temperature of the base and the coating is ~ 300 °C. The coating at a spraying distance of 150 mm is formed by medium- and large-sized powder particles, and small-sized particles lose velocity and temperature at this distance. The coating spot is larger than the diameter of the barrel, the border is blurred, the porosity of the coating is increased. At a spraying distance of 190 mm, the coating is formed of large-sized particles that have not lost their velocity and temperature. The coatings of large powder particles have a considerable porosity, the border of the spot is blurred, on the base it is possible to see traces of ricochet of large particles. As the spraying distance increases, the temperature and velocity of the spraying particles decreases, which leads to the formation of a loose coating and reduction in the adhesion strength, which can lead to delamination of the coating from the base. Thus, according to the results of the coatings produced during spraying at different spraying distances, a distance of 110 mm was chosen.

To produce a quality coating, it is necessary that the sprayed powder particles interacting with the products of detonation acquired the required energy characteristics, i.e. the temperature of 0.8–0.9 from the melting point of the powder material, the velocity of the powder particles is 600–1000 m/s at the exit from the barrel. Obtaining such characteristics is achieved by the optimal value of powder loading into the barrel — the distance between the edge barrel and the location of the material portion being sprayed at the moment of mixture explosion. The size of the powder portion load is regulated by the cyclogram.

The cyclogram provides a pulse of transporting gas to supply the portion (cloud) of the powder to the desired place of the barrel at the moment of initiation of the gas mixture explosion. The choice of the cyclogram should be coordinated with the degree of filling the barrel with a mixture of working gases so that the powder cloud does not go beyond the mixture. In the "Perun-S" installation, 8 cyclograms (four per each dispenser) are provided, which can be used to deposit coatings of powder materials with different density and different sizes of particles. To supply the powder to the desired place of the barrel (at this degree of filling), the cyclogram 2–2 (dispenser 2) is installed, which is intended for spraying powders with a density of 3–9 g/cm^3 and particle size of 10–50 μm, which provides the location of a powder cloud with a length of 200 mm at a distance from the barrel edge to the front part of the cloud being 150 mm. The generation frequency during spraying of coatings was 6.6 s^{-1}.

The amount of transporting gas consumption is used to regulate the amount of a portion of the powder to produce a certain thickness of the coating per 1 cycle. For this detonation installation with a barrel length of 550 mm and a barrel diameter of 20 mm, a portion of powder (most of the sprayed materials) is optimal, during spraying of which the thickness of the coating per 1 cycle is 4–6 μm. Increasing the portion of powder (and the thickness of the coating) causes non-uniform heating of moving particles in the center and on the periphery of the metallization flow. Reduction of a powder portion leads to a decrease in the thickness of the coating, which is not economically feasible.

For TiAl powders with a density of 3.0–3.8 g/cm^3, the consumption of composite powders in the installation Perun-S was 0.9–1.2 kg/h.

Thus, for spraying coatings from TiAl-based powders with a melting point of the base being 1200 °C and particle size of 40–100 μm, a mode with the ratio of working gases 1:3, 1:1.3 and their consumption: propane-butane of 0.5 m^3/h, oxygen — 1.55 m^3/h, air — 0.65 m^3/h was selected. The degree of filling the barrel was 64 %. To supply the powder to the desired place of the barrel (at this degree of filling), the cylogram 2–2 (dispenser 2) was installed. The consumption of transporting gas for powders with the density of 3.0–3.8 g/cm^3 and particles with the size of 40–100 μm was 0.15–0.3 m^3/h. The spraying distance is 110 mm.

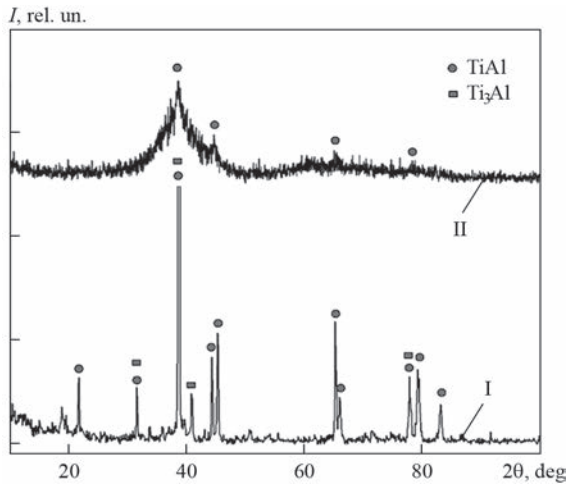

Figure 1. X-ray patterns of source TiAl powder (*a*) and TiAl powder after mechanical grinding in the planetary mill (*b*)

RESEARCH RESULTS AND DISCUSSION

Using the XRD method, in the source powder T65Yu35 TiAl, the phases of TiAl (γ-phase) and Ti_3Al were revealed (Figure 1, *a*). After grinding in the planetary mill, an expansion of diffraction lines and a decrease in their intensity (Figure 1, *b*) occurs, which indicates a partial amorphization of powder.

To find out the mechanism of physico-chemical interaction of components in CP in the conditions of the detonation spraying method, the coating of three types from TiAl powder without NRC additives was first investigated: 1) from the source powder in as-delivered state; 2) from the powder subjected to processing in the planetary mill for 1.5 h; 3) from the powder subjected to processing in the planetary mill with a subsequent conglomeration.

The study of the structure of detonation coatings from TiAl powder of all three types showed that the produced coatings are dense, without cracks and delaminations from the base, they contain large dark gray oxide lamellas, a small number of thin light lamellas and deformed light particles (Figure 2). In the coating from a grinded and conglomerated powder, the structure is more fine-dispersed with the most uniform distribution of light and dark lamellas (Figure 2, *c*). Microhardness in the coating from the source powder is 5330 ± 800 MPa, and in the coatings of grinded powder and that processed in the planetary mill with a subsequent conglomeration has almost no difference (average values are respectively 3990 ± 800, 4190 ± 630 MPa), and the most probable (Figure 3) are 3975 and 4010. The XRD method found that in the coatings from TiAl powders of all three types, the main phases are TiO_2, Al_2O_3 and TiO (Figure 4). The content of TiAl and Ti_3Al intermetallic phases from the conglomerated powder coatings are slightly increased relative to the coating from the source powder (traces). Regarding the quantitative phase composition, it is necessary to note the presence of more intensive peaks of intermetallic phases on X-ray patterns from grinded powders; in addition, judging by the intensity of X-ray lines, the content of TiO_2 is higher in the coating from the source TiAl powder (in Figure 4, *a*), than in the coatings of grinded powders (Figure 4, *b*, *c*), moreover, in the grinded powders, traces of Ti_3O_5 oxide were found. These differences may be associated with the

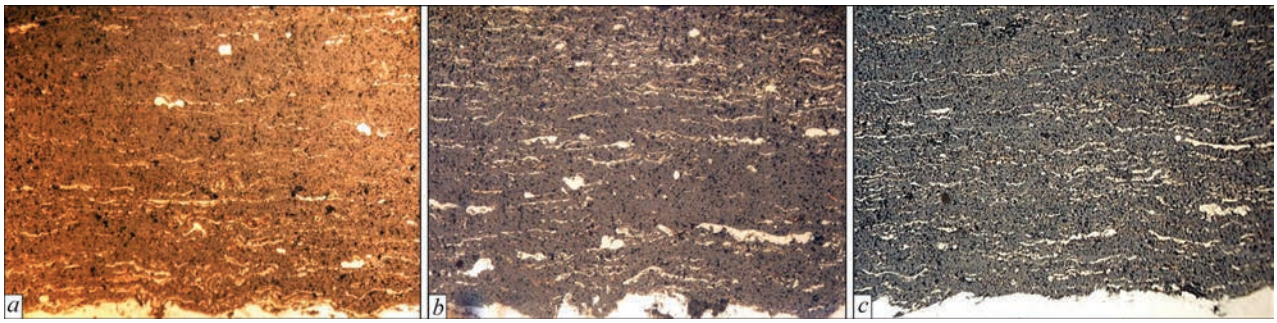

Figure 2. Microstructure (×400) of detonation coating from TiAl powder: *a* — source powder; *b* — powder produced by grinding in the planetary mill for 1.5 h; *c* — powder produced by grinding with a subsequent conglomeration

dispersion of sprayed powder particles (Table 1). The higher sizes of particles of 2nd and 3rd type as compared to the 1st one are explained by the formation of larger particles due to the welding processes during mechanical processing of powder in the planetary mill and in the future during conglomeration.

On the basis of the analysis of the results of the conducted investigations (Table 1), to produce composite powders and coatings from them, TiAl-powder of two types were selected: the powder processed in the planetary mill for 1.5 h; the powder processed in the planetary mill for 1.5 h with a subsequent conglomeration.

To deposit detonation coatings, the composite TiAl/NRC powders were used produced by the MChS method both in the initial state as well after additional processing-conglomeration (Table 2). At the same time, some differences in the structure and phase composition of the produced coatings were identified.

The examination of the structure of detonation coatings from composite TiAl/B_4C powder showed that the structure from a non-conglomerated powder (Figure 5, *a*) is dense, without cracks and delaminations, lamelar, consists of dark gray and has a small number of thin light lamellas. In the structure of the coating produced from a conglomerated powder (Figure 5, *b*), a larger number of light lamellas and non-melted particles with small dark gray inclusions is observed. The microhardness of the coating from the powders of both types differs slightly. The average values are 5550 ± 1080 and 4760 ± 950 MPa, respectively (most probable are 5090 and 5200) (Figure 6). When comparing the phase composition of the coatings (Figure 7) with the source powder (Table 2), it is possible to note an increase in the number of boride and carbide phases — products of interaction of CP components in the process of spraying and the appearance of oxides, first of all, of titanium as a result of interaction of CP particles with detonation flow in the process of spraying. At the same time, it can be noted that the coating from a conglomerated pow-

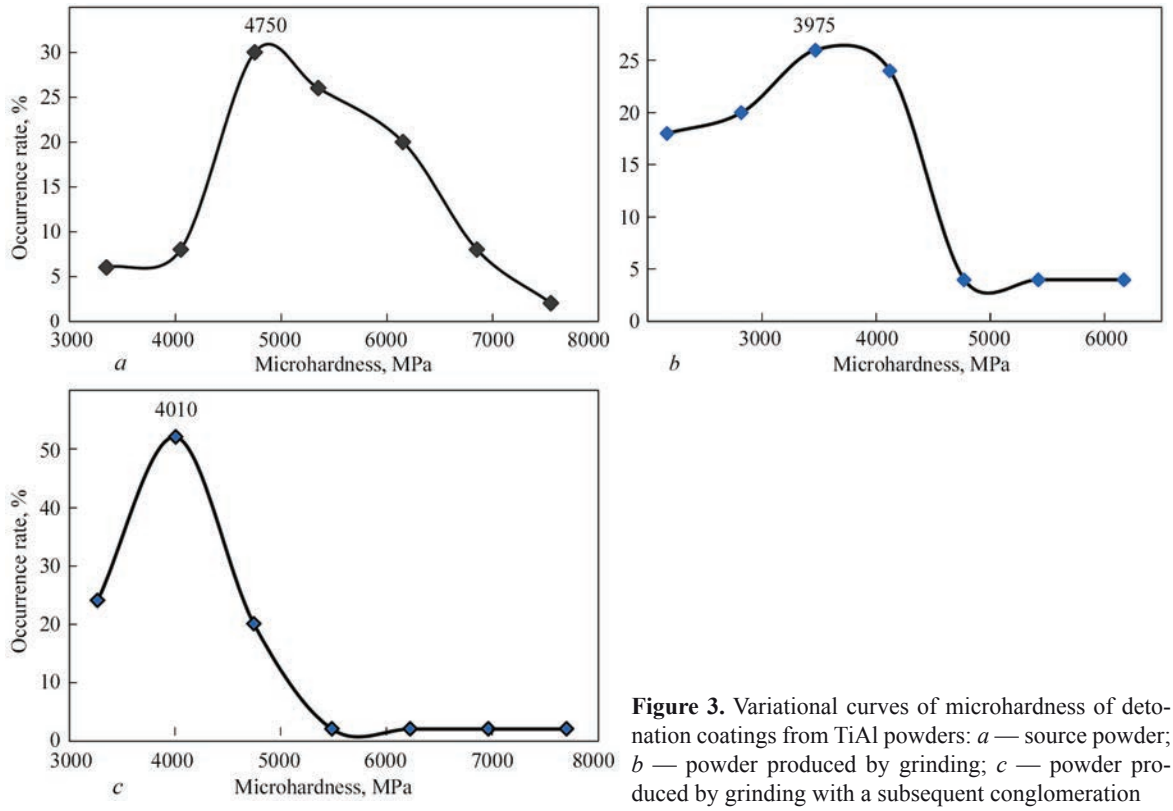

Figure 3. Variational curves of microhardness of detonation coatings from TiAl powders: *a* — source powder; *b* — powder produced by grinding; *c* — powder produced by grinding with a subsequent conglomeration

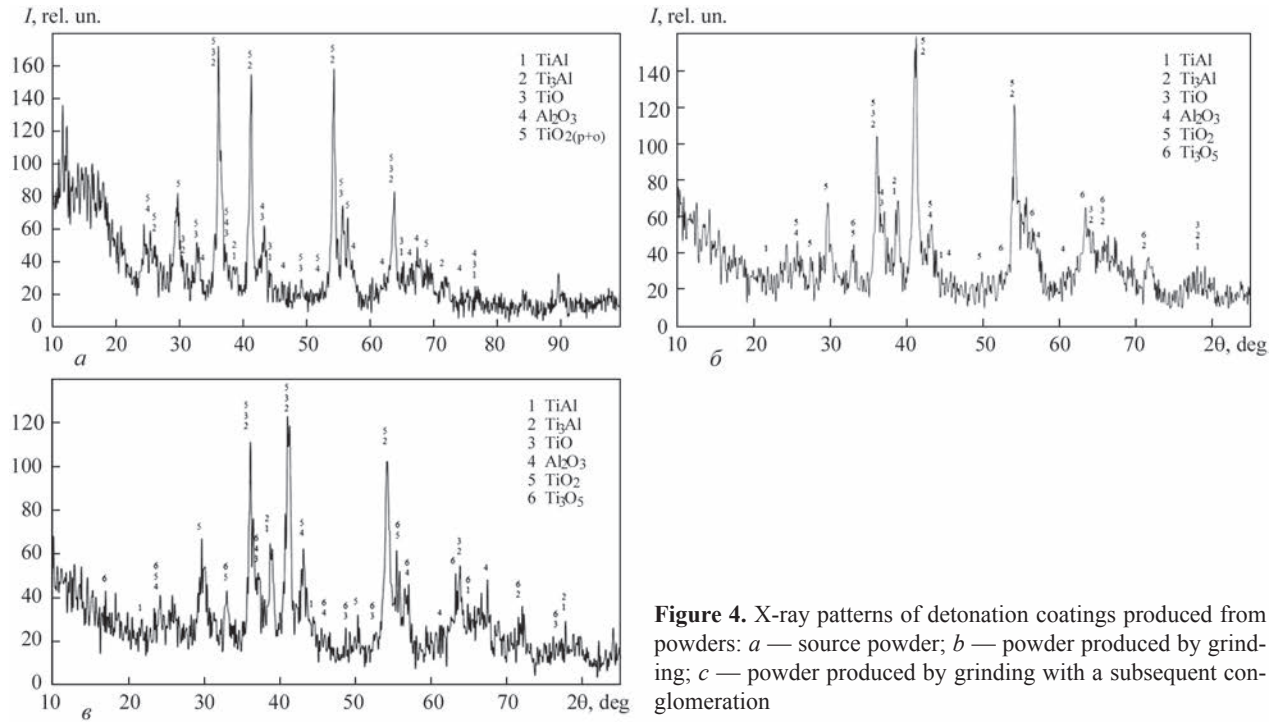

Figure 4. X-ray patterns of detonation coatings produced from powders: *a* — source powder; *b* — powder produced by grinding; *c* — powder produced by grinding with a subsequent conglomeration

der contains a lower amount of oxide phases, which is associated with a smaller specific particle surface that contacts the environment. On the other hand, the process of interphase interaction in the particles of a conglomerated powder proceeds more actively, which affects the phase composition — a number of interaction of TiAl products with B_4C increases, and the content of TiAl and Ti_3Al decreases.

In the detonation coatings from the composite powders of TiAl/BN while making the section, chipping of individual areas of the coating occurs, which indicates the brittleness of the formed phases (Figure 8). The coating produced from MChS powder, is strongly oxidized, has a dark gray color with small thin light lamellas (Figure 9, *a*). In the coating from the powder produced by MChS with the further conglomeration (Figure 9, *b*), more light lamellas and non-melted particles is observed. The microhardness of the coating from MChS powder is 4880 ± 1200 MPa, and from MChS powder with a subsequent conglomeration it is 4040 ± 850 MPa. The reduction of microhardness of the coatings from CP TiAl/BN of conglomerated powders was also noted on the variational curves (Figure 9).

The XRD method found that in the coating from MChS powder, a number of intermetallic phases (TiAl, Ti_3Al) is lower as compared to the source powder. The main phase in this coating is Ti_3O_5 oxide, the traces of TiN, TiB_2, AlB_2 and AlN phases and oxides TiO_2 and TiO (Figure 10, *a*) were also found in the coating. XRD method found, that in the coating from MChS powder with a subsequent conglomeration, the coating is less oxidized as compared to the coating from MChS powder, it contains a small amount of TiAl, Ti_3Al, in the coating an increase in the content of TiN, TiB_2, AlB_2 and AlN phases was revelaed and except of Ti_3O_5 and TiO_2 oxides, in the coating a high-temperature oxide Al_2TiO_5 phase is present (Figure 10, *b*).

The structure of detonation coatings from composite TiAl/SiC powders is dense, without cracks and delaminations from the base, with large dark-gray oxide

Table 1. Characteristics of TiAl powders and detonation coatings from them

Powder			Coating			
			Microhardness, MPa (P = 50 g)		Porosity, %	Phase composition
Type	Particle size, μm	Phase composition	Average	Most probable		
Source (1st type)	≤20	TiAl, Ti_3Al	5330 ± 800	4750	0.8	TiO, TiO_2, Al_2O_3, traces TiAl, Ti_3Al
Processed in the planetary mill for 1.5 h (2nd type)	4–80		3990 ± 800	3975	2.2	TiAl, Ti_3Al, TiO_2, TiO, Al_2O_3, traces Ti_3O_5
Processed with a subsequent conglomeration (3rd type)	40–80		4190 ± 630	4010	2.6	

Table 2. Characteristics of detonation coatings produced from composite powders

Characteristics of powder				Characteristics of coating				
Composition of mixture for CP, wt.%	Method of producing	Size of powder particles, μm	XRD	Thickness of coating, μm	Microhardness, MPa (P = 50 g)		Porosity, %	MChS
					Average	Most probable		
TiAl B_4C (16 % B_4C)	MChS,1.5 h	≤ 22	TiAl,Ti_3Al, TiB_2,TiC	175 ± 25	5550 ± 1084	5090	4	TiAl, Ti_3Al, TiC, TiB_2, AlB_2, TiO_2, Ti_3O_5, traces Al_2O_3
	MChS, 1.5 h + conglomeration	40–100		460 ± 30	4760 ± 1060	5200	8	TiB_2, AlB_2, TiC, Ti_3O_5, TiO_2, traces TiAl, Ti_3Al
TiAl + BN (18 % BN)	MChS, 1,5 год	≤ 19	TiAl, Ti_3Al, TiB_2, AlB_2, TiN, AlN, BN	215 ± 15	4880 ± 1200	5700	3	Ti_3O_5, TiO, TiO_2, TiN, TiB_2, AlB_2, traces TiAl, Ti_3Al
	MChS, 1.5 h + conglomeration	20–80		440 ± 30	4040 ± 850	4300	12	Ti_3O_5, TiO_2, TiN, TiB_2, AlB_2, Al_2TiO_5, traces TiAl, Ti_3Al
TiAl + SiC (16 % SiC)	MChS, 1.5 h + конгл.	≤ 19	TiAl, Ti_3Al, SiC, TiC, Ti_5Si_3	410 ± 70	4230 ± 750	5000	4	TiC, Ti_5Si_3, TiO_2, Ti_3O_5, SiO_2, traces Ti_3Al, TiAl,
	MChS, 1.5 h + conglomeration	40–100		480 ± 46	5250 ± 800	5700	2.9	
TiAl + Si_3N_4 (18 % Si_3N_4)	MChS, 1.5 h	≤ 14	TiAl, Ti_3Al, TiN, Si_3N_4, Ti_5Si_3, AlN	385 ± 50	4010 ± 670	4000	2.1	Ti_3Al, TiN, Ti_5Si_3, Al_2O_3, TiO_2, SiO_2, Al_2TiO_5, traces AlN, TiAl
	MChS, 1.5 h + conglomeration	40–100		500 ± 20	5440 ± 970	4975	4.4	

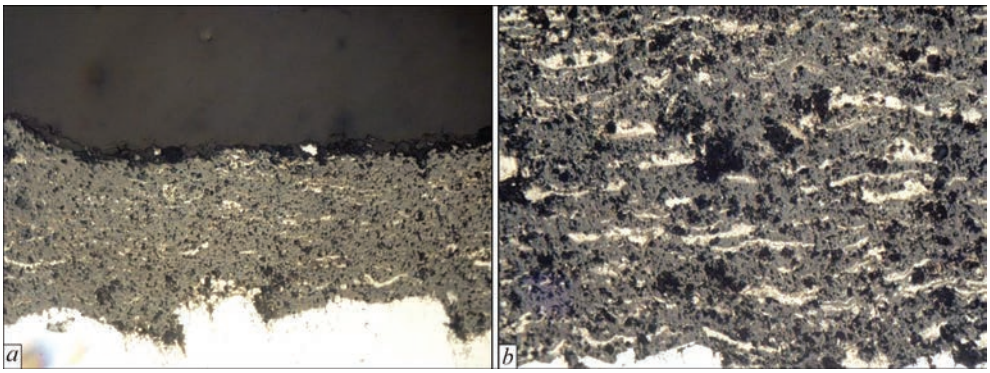

Figure 5. Microstructure (×400) of detonation coatings from composite TiAl/B_4C powders produced by the methods: *a* — MChS; *b* — MChS with a subsequent conglomeration

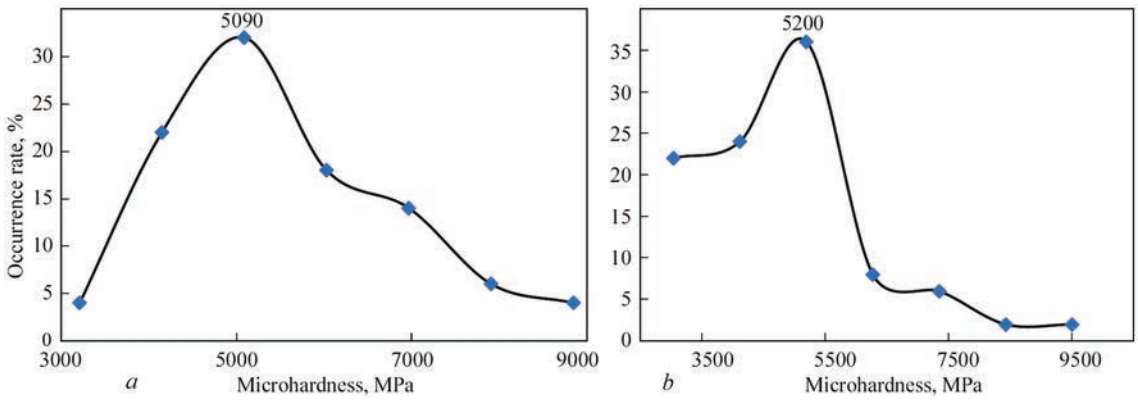

Figure 6. Variation curves of microhardness of detonation coatings from composite TiAl/B_4C powders produced by the methods: *a* — MChS; *b* — MChS with a subsequent conglomeration

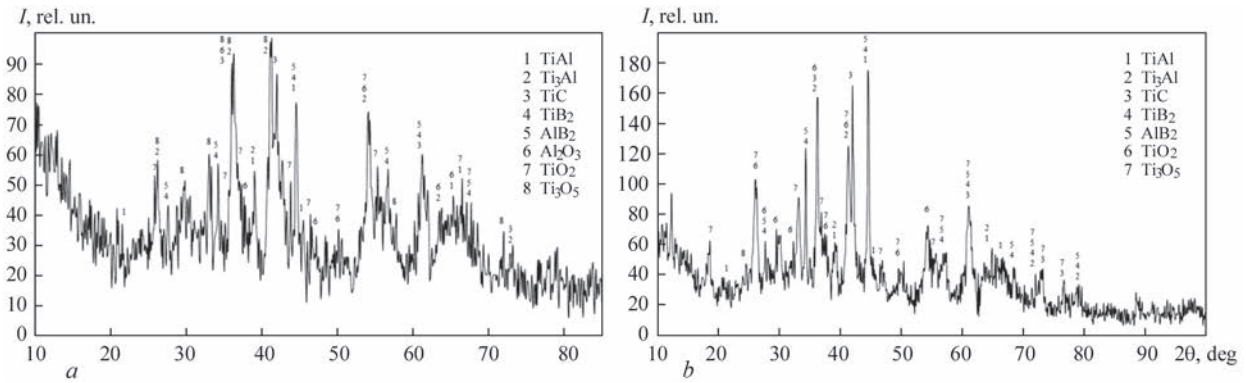

Figure 7. X-ray patterns of detonation coatings from composite TiAl/B_4C powders produced by the methods: *a* — MChS; *b* — MChS with a subsequent conglomeration

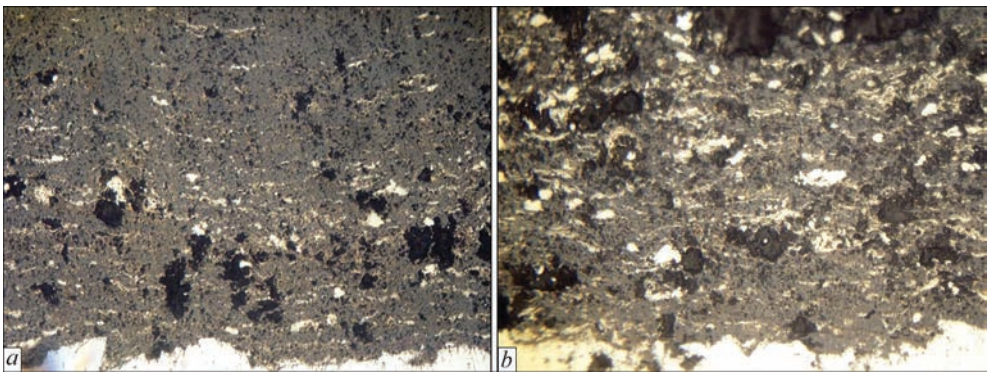

Figure 8. Microstructure (×400) of detonation coatings from composite TiAl/BN powders produced by the methods: *a* — MChS; *b* — MChS with a subsequent conglomeration

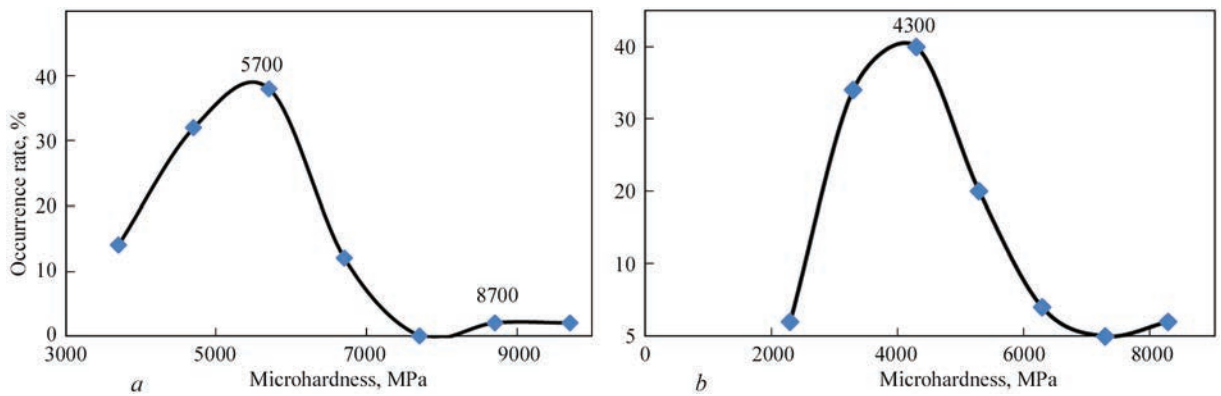

Figure 9. Variation curves of detonation coatings from composite TiAl/BN powders produced by the methods: *a* — MChS; *b* — MChS with a subsequent conglomeration

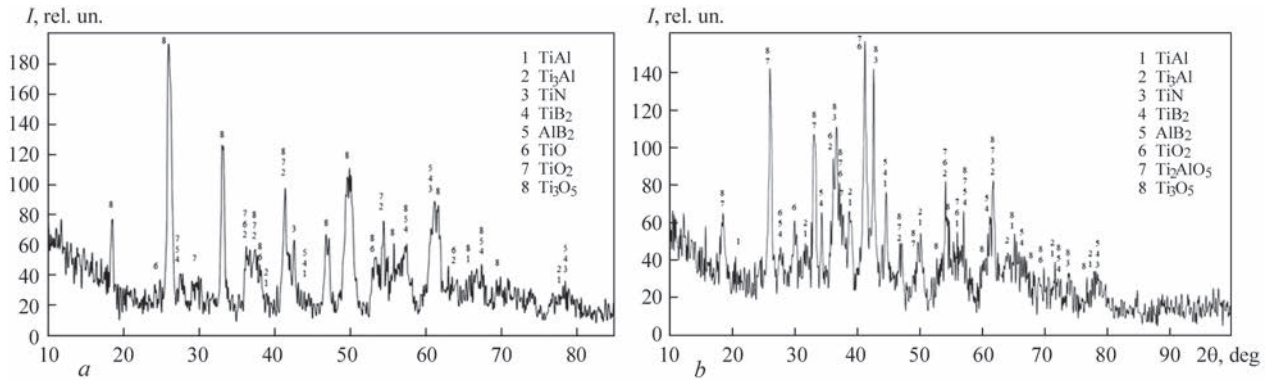

Figure 10. X-ray patterns of detonation coatings from composite TiAl/BN powders produced by the methods: *a* — MChS; *b* — MChS with a subsequent conglomeration

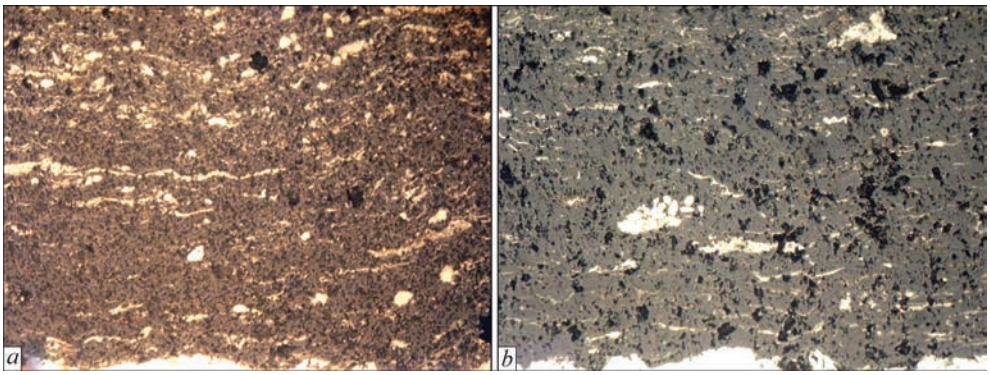

Figure 11. Microstructure of detonation coatings from composite TiAl/SiC powders produced by the methods: *a* — MChS; *b* — MChS with a subsequent conglomeration

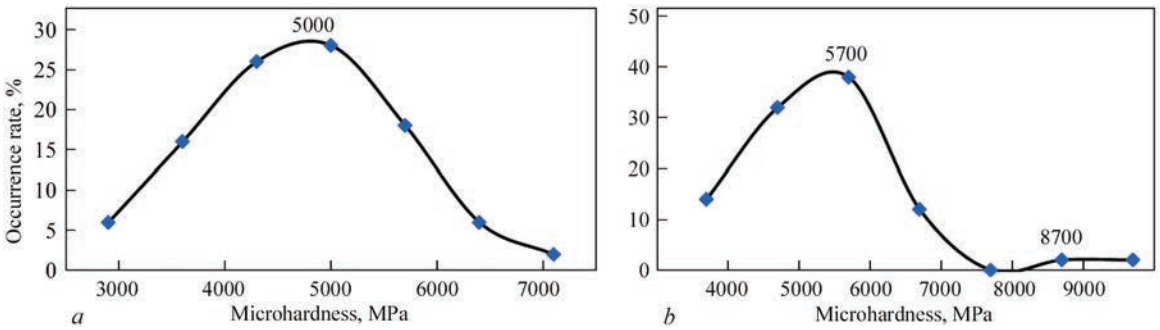

Figure 12. Variational curves of detonation coatings from composite TiAl/SiC powders produced by the methods: *a* — MChS; *b* — MChS with a subsequent conglomeration

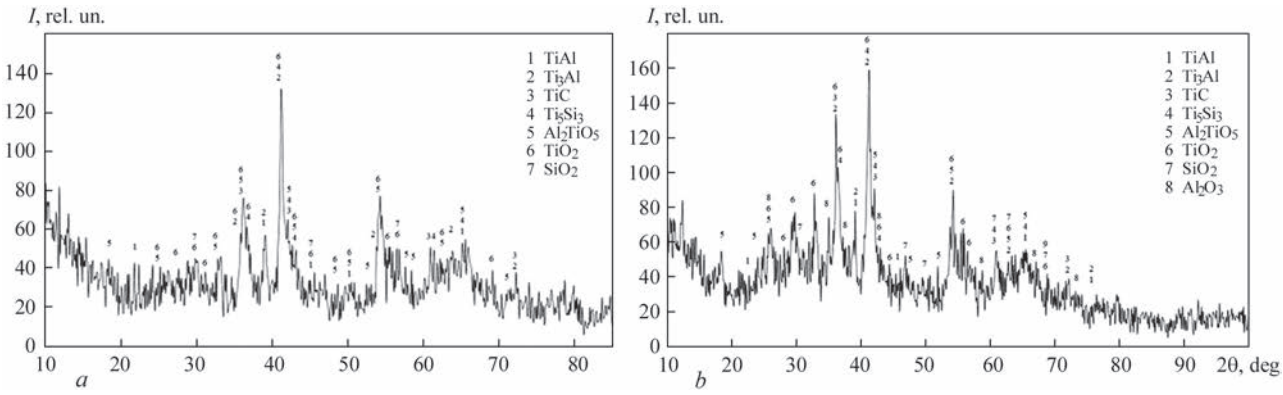

Figure 13. X-ray patterns of detonation coatings from composite TiAl/SiC powders produced by the methods: *a* — MChS; *b* — MChS with a subsequent conglomeration

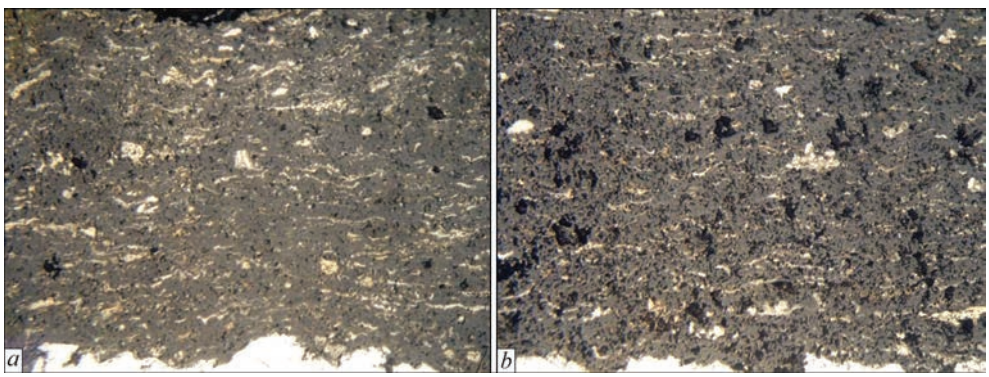

Figure 14. Microstructure of detonation coatings from composite TiAl/Si_3N_4 powders produced by the methods: *a* — MChS; *b* — MChS with a subsequent conglomeration

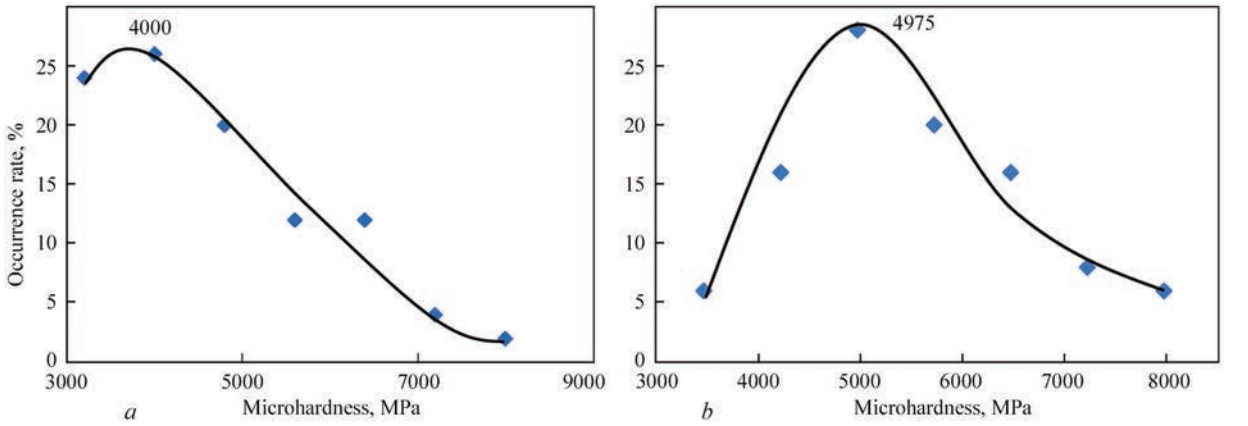

Figure 15. Variation curves of detonation coatings from composite $TiAl/Si_3N_4$ powders produced by the methods: *a* — MChS; *b* — MChS with a subsequent conglomeration

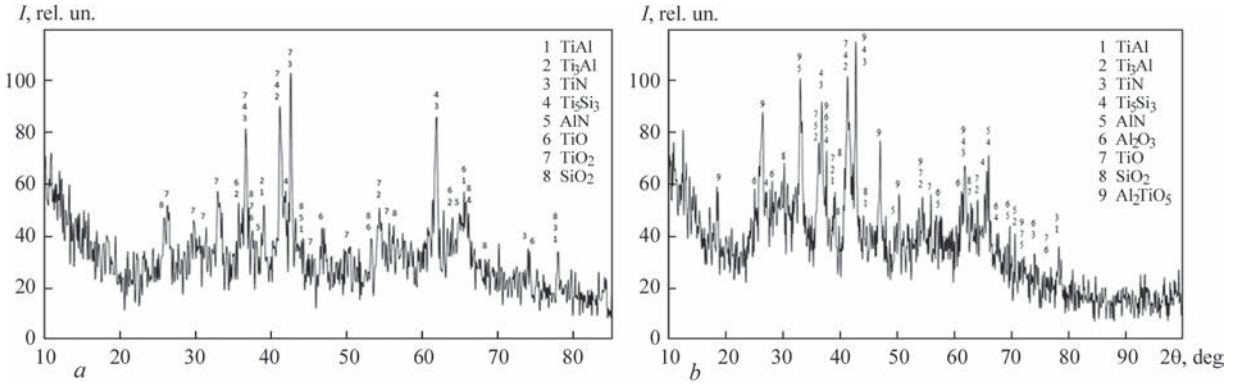

Figure 16. X-ray patterns of detonation coatings from composite $TiAl/Si_3N_4$ powders produced by the methods: *a* — MChS; *b* — MChS with a subsequent conglomeration

lamellas and thin light lamellas (Figure 11). The average value of microhardness of the coating from MChS powder is lower than in the coating from MChS powder with a subsequent conglomeration (4230 ± 750 and 5250 ± 800 MPa, respectively), which is associated with a denser structure of the coating from MChS powder with a subsequent conglomeration. The lower values of microhardness were obtained on the variational curves (Figure 12) for the coatings made of non-conglomerated powder.

On the X-ray patterns of the coatings (Figure 13), in addition to the main phases of TiAl, Ti_3Al, TiC and Ti_5Si_3, which are present in the powder, the oxides TiO_2, SiO_2, Al_2TiO_5 and Ti_3O_5 were found.

The structures of detonation coatings from the composite powders of $TiAl/Si_3N_4$ are similar to the structures of coatings from the composite powders of TiAl/SiC: they are dense, without cracks and delaminations from the base, with large dark-gray oxide lamellas and thin light lamellas (Figure 14). Microhardness of MChS powder coatings is lower than in the coating from MChS powder with a subsequent conglomeration (4010 ± 670 and 5440 ± 970 MPa, respectively), which as in the case of CP TiAl/SiC is associated with a denser structure of the coating from MChS powder with a subsequent conglomeration. The same regularity was marked for the most probable values of microhardness on the variational curves (Figure 15).

On the X-ray patterns (Figure 16, *a*, *b*) both the main phases characteristic of the source powder TiAl, Ti_3Al, TiN, Ti_5Si_3, AlN, as well as oxides TiO_2, SiO_2, TiO were revealed, which are present in the coating from MChS powder.

CONCLUSIONS

1. As a result of studying the impact of technological parameters on the formation of detonation coatings from TiAl intermetallics and composite powders on its base with the additives of non-metallic refractory compounds (B_4C, BN, SiC, Si_3N_4), the mode of producing high-quality coatings, distinguished in a high density of structure and absence of defects at the border with the base, was revealed.

2. During detonation spraying from TiAl powder, the oxidation of its particles with the formation of titanium (TiO, TiO_2, Ti_3O_5) and aluminium (Al_2O_3) oxides occurs. The content of oxides in the coating depends on the dispersion of the powder. Thus, it is lower in the coatings from conglomerated powders than in the coating from powders subjected to grinding only.

3. When forming detonation coatings from CP of TiAl/NRC, both oxidation of sprayed particles as well

as processes of interphase interaction of its components occur. Thus, in the coatings from CP of TiAl/B_4C oxides TiO_2, Ti_3O_5 and Al_2O_3 were revealed as well as increased content of TiC, TiB_2 and $A1B_2$ as compared to source CP. In the coatings from CP of TiAl/BN, the main phases are TiO, TiO_2, and Ti_3O_5 oxides, TiB_2 and $A1B_2$ borides and TiN nitride. When depositing coatings from TiAl/SiC and TiAl/Si_3N_4, oxidation occurs less actively than in the previous cases, and in CP of TiAl/Si_3N_4, the process of interphase interaction runs less active.

4. Comparing the structure and phase composition of detonation coatings from MChS powders and powders produced by MChS method with a subsequent conglomeration shows that in the second case, a decrease in the content of oxides for all compositions is observed, and the content of products of interphase interaction between TiAl and inclusions of non-metallic refractory compound grows.

5. The structure of coatings of all compositions is lamelar, consists of dark-gray (oxide) and light (metal-like) lamellas. In the coatings produced from MChS powders with a subsequent conglomeration, it is more dense and homogeneous than in the coatings from powders not exposed to conglomeration. The confirmation of a higher degree of homogeneity of the structure and phase composition is also the distribution of microhardness on the variational curves.

REFERENCES

1. Gotman I., Koczak, M.J. (1994) Fabrication of A1 matrix in situ composites via self-propagating synthesis. *Materials and Sci. and Eng.*, **187**, 189–199.
2. Han, Ch., Babicheva, R., Chu, J. et al. (2020) *Microstructure and mechanical properties of (TiB+TiC)/Ti composites fabricated in situ via selective laser melting of Ti and B_4C powders*. Additive Manufacturing.
3. Pfeiler, M., Zechner, J., Penoy, M. et al. (2009) Improved oxidation resistance of TiAlN coatings by doping with Si or B. *Surface and Coatings Technology*, **203**, 3104–3110.
4. Wu, H., Cui, X.P., Geng. L. et al. (2013) Fabrication and characterization of in-situ TiAl matrix composite with controlled microlaminated architecture based on SiC/Al and Ti system. *Intermetallics*, **43**, 8–15.
5. Gan, J.A., Berndt, Ch.C. (2015) Thermal spray forming of titanium and its alloys. *Titanium Powder Metallurgy*, 425–446.
6. Cinca, N., Guilemany, J.M. (2012) Thermal spraying of transition metal aluminides: An overview. *Intermetallics*, **24**, 60–72.
7. Goral, M., Swadzba, L., Moskal G. et al. (2011) Diffusion aluminide coatings for TiAl intermetallic turbine blades. *Intermetallics*, **19**, 744–747.
8. Venkataraman, R., Ravikumar, B., Krishnamurthy. R., Das, D.K. (2006) A study on phase stability observed in as sprayed alumina-13 wt.% titania coatings grown by detonation gun and plasma spraying on low alloy steel substrates. *Surface and Coatings Technology*, **201**, 3087–3095.
9. Semenov, S., Cetegen, B. (2002) Experiments and modeling of the deposition of nanosttructured alumina-titania coatings by detonation waves, *Materials Sci. and Eng. A*, 335(**1–2**), 67–81.
10. Cetegen, B., Semenov, S., Goberman, D. (2003) Deposition of multi-layered alumina–titania coatings by detonation waves. *Scripta Materialia*, **48**, 1483–1488.
11. Oliker, V.E., Syrovatka, V.L., Timofeeva, I.I. et al. (2005) Influence of properties of titanium aluminide powders and conditions of detonation spraying on phase- and structure formation of coatings. *Poroshk. Metallurgiya*, **9–10**, 74–84 [in Russian].
12. Oliker,V., Sirovatka. V., Timofeeva I. et al. (2006) Formation of detonation coatings based on titanium aluminide alloys and aluminium titanate ceramic sprayed from mechanically alloyed powders TiAl. *Surface and Coatings Technology*, **200**, 3573–3581.
13. Oliker,V., Sirovatka. V., Gridasova, T.Ya. et al. (2009) Influence of gas environment on evolution of structure and phase composition during spraying process of detonation coatings of mechanochemically synthesized Ti–Al–B powders. *Poroshk. Metallurgiya*, **11–12**, 12–20 [in Russian].
14. Dudina, D., Korchagin, M., Zlobin S. et al. (2012) Compositional variations in the coatings formed by detonation spraying of Ti_3Al at different O_2/C_2H_2 ratios. *Intermetallics*, 140–146.
15. Oliker, V., Kresanov, V. (2000) Structure and properties of detonation coatings based on γ-TiAl. *Powder Metallurgy and Metal Ceramics*, 39, 590–593.
16. Bratanich, T.I., Skorokhod, V.V., Kopylova, L.I. et al. (2010) Destructive hydrogenation and recombination of α_2-Ti_3Al alloy as a way to produce solid nanocomposites and coatings with improved properties. Pt 2. Recombination of Ti_3Al and producing of detonation coatings. *Poroshk. Metallurgiya*, **9–10**, 132–141 [in Ukrainian].
17. Borysov, Yu.S., Borysova, A.L., Burlachenko, O.M. et al. (2021) Composite powders based on FeMoNiCrB amorphizing alloy with additives of refractory compounds for thermal spraying of coatings. *The Paton Welding J.*, **11**, 38–47. DOI: https://doi.org/10.37434/tpwj2021.11.07

ORCID

A.L. Borysova: 0000-0002-7376-3370,
A.I. Kildii: 0000-0001-8133-8705,
T.V. Tsymbalista: 0000-0001-9569-7776,
M.A. Vasylkivska: 0000-0001-8311-6428

CONFLICT OF INTEREST

The Authors declare no conflict of interest

CORRESPONDING AUTHOR

T.V. Tsymbalista
E.O. Paton Electric Welding Institute of the NASU
11 Kazymyr Malevych Str., 03150, Kyiv, Ukraine.
E-mail: tstania@ukr.net

SUGGESTED CITATION

A.L. Borysova, A.I. Kildii, T.V. Tsymbalista, M.A. Vasylkivska (2023) Detonation coatings based on TiAl intermetallics with additions of non-metallic refractory compounds. *The Paton Welding J.*, **2**, 24–33.

JOURNAL HOME PAGE

https://patonpublishinghouse.com/eng/journals/tpwj

Received: 09.01.2023
Accepted: 30.03.2023

DOI: https://doi.org/10.37434/tpwj2023.02.05

HYGIENIC CHARACTERISTIC OF MAGNETIC FIELDS AT DIFFERENT ARC WELDING METHODS

O.G. Levchenko[1], **Yu.O. Polukarov**[1], **O.M. Honcharova**[2], **O.M. Bezushko**[2]

[1]National Technical University of Ukraine «Igor Sikorsky Kyiv Polytechnic Institute»
37 Peremohy Prosp., 03056, Kyiv, Ukraine
[2]E.O. Paton Electric Welding Institute of the NASU
11 Kazymyr Malevych Str., 03150, Kyiv, Ukraine

ABSTRACT

The levels and spectral composition of magnetic fields, generated by equipment for arc welding by different methods were determined, in order to assess their influence on the welder's body. Published data on electromagnetic safety of electric arc welding were analyzed. A description of the proposed methodological approaches to determination of magnetic field levels, their measurement means and methods of assessment of their influence on the welder's body is given. Modern standards are characterized as to evaluation of the electromagnetic field impact on man, and their difference from the earlier applied standards. It is shown that new publications began to appear recently, which are devoted to the harmfulness of electromagnetic fields at application of electric production equipment. Hence the need to conduct new studies of electromagnetic fields, in particular their magnetic component (magnetic field intensity, A/m), when using welding equipment. This is required for hygienic assessment of the magnetic fields and development of the respective methods and means of welder protection. For this purpose, it was necessary to choose new generation instruments for determination of the intensity of magnetic fields, generated by welding equipment proper. Proceeding from analysis of the obtained oscillograms and spectrograms of the magnetic fields, evaluation of their levels was performed at application of different arc welding methods. It is shown that the spectral composition of the magnetic field signal is determined, predominantly, by the welding process proper, features of arc burning and mode of electrode metal transfer in the arc gap, as well as output parameters of the welding arc power source.

KEYWORDS: arc welding, electromagnetic field, field intensity, oscillograms, spectrograms, welder protection

INTRODUCTION

Welding production is characterized by a continuous increase in the scope of applications of electric and electronic equipment, operation of which is accompanied by generation of higher levels of electromagnetic radiation [1, 2], harmful and in some cases hazardous for the human body. Therefore, special attention is given to the issues of electromagnetic safety of production and household equipment, impact of electromagnetic fields (EMF) on man [3–5], as well as development of respective measures and means of protection from them.

Unsolved issues of harmful and hazardous effect of EMF on the welder's body [1] require special attention, as welders are exactly one of the groups of workers exposed to the impact of highly intensive EMF, particularly, when they are located close to welding equipment and at direct contact of cables with their body [2, 6]. Depending on the welding process, type of welding equipment and distance from the worker to it, the levels of EMF magnetic component, i.e. magnetic field (MF) intensity can exceed the maximum permissible levels and can be hazardous for the human body.

The main MF sources are heavily loaded circuits, and particularly the welding circuit. The amplitude value of MF intensity in the welder workplace depends on welding current, welding circuit dimensions and shape, as well as on the distance between the worker and the field source [7]. Operation of electric equipment for arc welding is accompanied by generation of high level MF, predominantly, in the superlow frequency range [6] that creates a certain hazard for welders. So, work [2] presents the results of measurement of MF levels in the workplace for MAG welding (metal electrode in active gas) in keeping with the current European Directive 2013/35EU [3]. Obtained results of MF levels in the frequency band from 5 Hz to 400 kHz showed that they significantly exceed the MF levels generated by other types of electric equipment. This is attributable to the fact that relatively high electric currents (up to several hundred amperes) are used in arc welding. In work [2] in order to study the MF impact on the welder, its level in the workplaces was measured by a 3-axis Hall magnetometer, fastened to the welder's wrist, i.e. in the position closest to MF source (near the current source cable). Measurement results showed that MF magnetic induction in this point was equal to 1.49 mT that is below the limit permissible level (LPL) by the standards of DSN 3.36.096–2002 [8] (1.75 mT for an eight hour working shift).

It should be noted that the old sanitary standards [9] that were valid until 2002, specified MF only at 50 Hz frequency. The new Ukrainian standards cover the entire frequency range characteristic for welding processes and all the required factors: frequency, intensity and time of MF action on the human body. It enables their objective hygienic characterization for the human body.

Previous publications on MF were based on outdated procedures and they do not provide an adequate idea of MF impact. At present some, new publications on EMF harmfulness at application of household appliances began to appear, but there are no data on EMF in welding. This is attributable to absence of the respective instruments, which would allow fixing the magnetic field levels, characteristic exactly for the welding equipment (not on the level of μT, but predominantly, on the level of mT). It necessitated performance of new studies of MF (magnetic field intensity, A/m) at application of both the currently available and new welding equipment. Such studies need to be conducted in wide frequency ranges in the workplaces at application of different kinds of welding. Here, the influence of welding process features, distance from the welder workplace to MF source and time of his staying in the hazardous impact zone on MF level and frequency should be taken into account. Such data are required to develop the methods and means for protection from MF.

The objective of this work is investigation of magnetic field intensity at different arc welding methods for their hygienic assessment in keeping with the new standards.

The following tasks were posed in order to reach this goal:

- define the optimal conditions for conducting experiments on determination of the intensity of MF, generated by welding equipment;
- determine the permissible time of welder working in the zone with higher MF level;
- provide hygienic evaluation of MF in keeping with the new standards for further development of recommendations on welder protection from MF.

EXPERIMENTAL PROCEDURE

Assessment of MF parameters in the welder workplace was performed in the following sequence:

- determination of the possible zone of the worker being near the electric equipment during the welding current flowing;
- identification of points as close as possible to MF source in this zone;
- determination of radiation frequency ranges and measurement of MF intensity in these points and ranges;
- determination of MF time characteristics.

Measurements of MF intensity at arc welding methods should be conducted, taking into account the electric cable layout.

MF intensity was measured using a remote sensor (magnetic field converter), integrating *RC*-circuit and a recording device, which was a digital storage oscillograph with the function of fast fourier transformation (FFT) with extension block. The following instruments were used:

- magnetic field sensor DMP-1 (Ukraine);
- magnetic field induction meter GFI-1 (Ukraine);
- magnetic field induction meter TP2-2U-01 (Ukraine);
- oscillograph PCS-500 with PC (Velleman, Belgium);
- digital storage oscillograph TDS 1002 (Tektronix, USA).

During measurement of MF intensity, the sensor was brought into the studied field, and oriented in space by the maximum readings of the recording device. Three measurements were taken in the form of short pulses with a long period. The sensor was placed successively in three planes normal to each other, and its readings were recorded in each plane. The amplitude value of MF intensity vector was determined by the following formula [8]:

$$H_m = \sqrt{H_x^2 + H_y^2 + H_z^2}, \quad (1)$$

where H_x, H_y, H_z are the values of MF intensity in each plane.

Total value of magnetic field H was found from the following expression [8]:

$$H = \sqrt{H_1^2 + H_2^2 + \ldots + H_n^2}, \quad (2)$$

where H_n is the intensity of the magnetic field of a separate harmonic.

The exposure duration of workers during the shift was determined by conducting chronometric observations. The sum of total welding time shows the exposure time during the day.

Experiments were conducted in PWI welding laboratories in typical workplaces. MF intensity measurements were performed at manual, automatic and semi-automatic arc welding methods at direct and alternating current. Parts for welding were installed on the working surface of the metal table. Layout of welding equipment (power source, ballast rheostats, steel gas cylinders, etc.) was independently optimal. In connection with free layout of the power sources and ballast rheostats, the layout of the welding cables was also free in space and relative to the welder.

The main task of measurement of MF intensity is its comparison with the modern sanitary standards [8]. Here, MF scattering from the power sources, magnetic interference from neighbouring stations and impact of ferromagnetic masses, having a great influence on measurements, were not of fundamental importance at this stage of investigations. This is due to the fact that at manual welding the level of MF induced on the surface of different body parts of the welder and inside his body, is determined predominantly by welding current. In addition, the MF level is significantly influenced by the area of the radiating circuit, welders

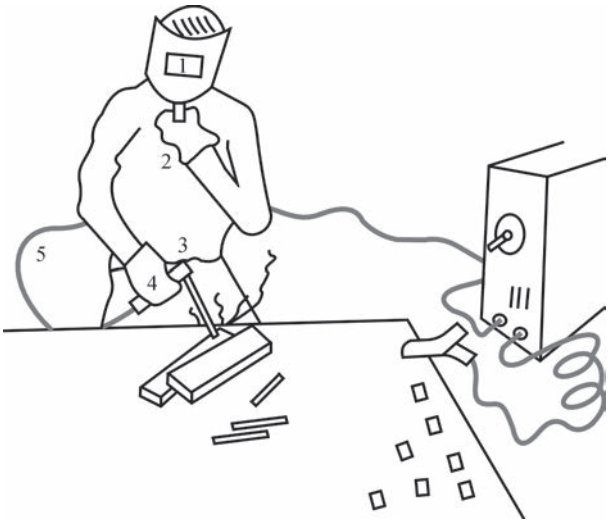

Figure 1. Layout of the zones of magnetic field intensity measurement: 1 — head (forehead); 2 — breast; 3 — abdomen; 4 — wrist; 5 — cable

position relative to the main radiation sources and the distance from the radiator to the welder body.

The layout of the zones where measurements were performed at manual and semi-automatic welding is shown in Figure 1.

The given description of experimental conditions allows correct measurement of MF levels in all the sensitive points of the human body, which can be exposed to the hazardous and harmful impact of MF. Such points mostly include those marked in Figure 1: 1 — brain; 2 — heart and lungs (breast); 3 — urogenital organs (abdomen); 4 — wrist. As the electric cable can touch the welder's body, we also have to measure the MF intensity on it.

Evaluation of the obtained results of MF intensity measurement was performed by their comparison with LPL standard values [8], which required knowledge of the welder exposure time in these fields. For this purpose, chronometric observation of the specific technological process which could be implemented under the real production conditions, was performed. However, earlier studies of welder employment show that the MF impact on the body is of intermittent nature. So, on the whole during an eight-hour working shift, the manual arc welding personnel stays in the zone of MF unfavourable impact for not more than two hours, which is due to the need to perform preparatory operations and welding equipment duty cycle (DC, %). Usually, it is equal to 20–60 % of the five-minute working cycle for manual arc and semi-automatic welding.

Table 1. Requirements to magnetic field levels in keeping with DSN 3.3.6.096–2002 [8]

Parameters	Limit amplitude values in the spectral ranges		
	0–5 Hz	5–50 Hz	0.05–1.0 kHz
$EH_{H_{LP}}$, (A/m)²·h	$1.4 \cdot 10^8$	$1.6 \cdot 10^7$	70000
H_{LP}, (A/m) for 2 h	11832	2828	187

Note. $H_{LP} = \sqrt{\frac{EH_{H_{LP}}}{T}}$, where $EH_{H_{LP}}$ is the limit admissible value of energy load during the work day; T is the exposure time, h.

Thus, taking 2 hours per shift as the net welding time, the normed parameters, in keeping with the sanitary standards, will have the values, given in Table 1.

Such conditions of performance of experimental measurements of MF intensity, i.e. net welding time, which is equal to 2 hours per shift, allows objective determination of the real values of MF LPL.

EXPERIMENTAL RESULTS AND THEIR ANALYSIS

Investigation of MF intensity was performed at arc welding by different methods (automatic submerged-arc, manual coated-electrode, semi-automatic gas-shielded welding) at electric current of industrial frequency (50 Hz), and direct current. The conditions of experiment performance (welding methods, brand of welding consumables and equipment, welding modes), as well as the results of determination of MF intensity are given in Tables 2–5.

Results of determination of MF intensity at automatic submerged-arc welding, using a thyristor transformer TDF-1002 with phase control, were derived by the method of analysis of oscillograms and spectrograms, obtained using the above-mentioned instruments. Measurements were conducted at 0.5 m distance from the axis of welding nozzle of TS-17 semi-automatic machine. The magnetic field, induced by welding current, is visually perceived as sinusoidal in the oscilloscope screen (Figure 2). However, its discrete spectrum (Figure 3) is characterized both by a pronounced predominantly right harmonics with 50 Hz frequency (H_{m50}), which reaches the maximum value in the area of the welder's abdomen H_{m50} = 360 A/m, and by harmonics H_{m100}= 180 and H_{m150} = 150 A/m. Obtained measurement results (Table 2) were compared with MF standard values.

Thus, determination of MF levels at automatic a.c. submerged-arc welding in the mode of medium power showed results satisfactory in hygienic terms (Table 2). One can see from the tabulated results that no exceeding of MF LPL was found in any of the studied ranges.

Here, it was taken into account that the automatic welding operator does not have to be continuously present in MF impact zone, i.e. he can be protected by distance from the welding equipment, minimizing the harmful impact of MF on the body.

Effective value of magnetic field H, calculated by expression (2), is equal to 404 A/m, that is much lower than the standard values (1400 A/m).

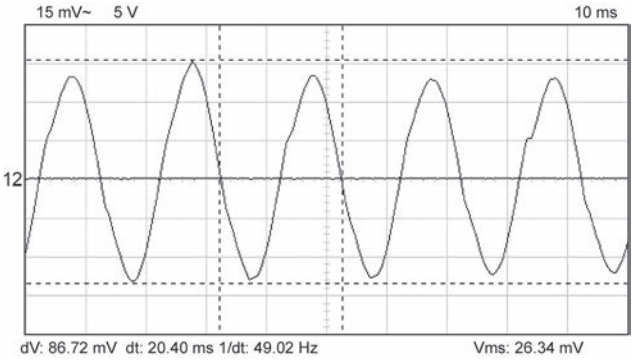

Figure 2. Oscillogram of the magnetic field at automatic submerged-arc welding

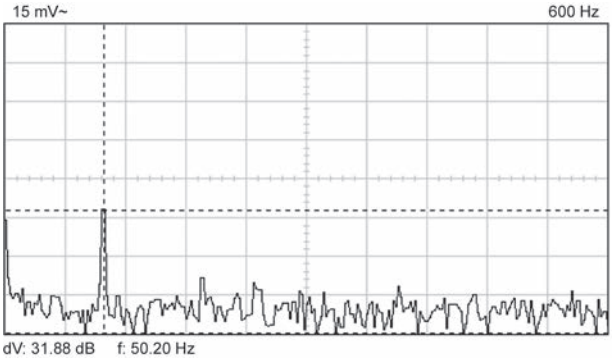

Figure 3. Spectrogram of the magnetic field of automatic submerged-arc welding

Further verification in keeping with DSN 3.3.6.096–2002, consists in checking the balance of energy load by frequency ranges and exceeding the norm in the range of 0–1000 Hz by expression [8]:

$$\sum H_n^2/\text{LPLs}^2 \le 1, \quad (3)$$

where LPLs are the limit permissible levels of MF of the respective ranges.

So, for the highest MF intensities, in this case in the region of the welder's abdomen, the value of ratio (3) is more than a unity at a two-hour exposure. Thus, in this zone at automatic submerged-arc welding the permissible values of MF intensity are exceeded, which requires application of protection means of the welder (in this case automatic welding operator).

Exceeding MF permissible level in the considered case is due to a non-sinusoidal shape of welding current and presence of MF second and third harmonics H_{m100} = 180 MPa and H_{m150} = 150 A/m in the spectrum.

It is understandable that in this case there is no need for the welding operator to stay in the above-mentioned zone, and the so-called distance protection can be used. In other cases, for instance, for manual and semi-automatic welding, the question of welder protection from MF will be more complicated.

Analysis of oscillograms and spectrograms, characteristic for other arc welding processes, was performed in a similar manner (Tables 3–5).

Results of studying MF levels (Table 3) at coated-electrode manual arc welding, using electrodes of ANO-2 grade in the optimal mode, showed no exceeding of standard MF levels in the frequency range of 0–5 Hz. In the frequency range of 5–50 Hz there is no exceeding either: all MF intensity values are below LPL at a two-hour or even eight-hour exposure. However, MF intensity near the cable proper (current conduit), which connects the welding current rectifier VDU-506 with the electrode holder, is equal to 3977 A/m along the entire cable length in the frequency range of 0–5 Hz, i.e. the stress intensity in this zone almost reaches LPL (4200 A/m). Now, in the frequency range of 50–1000 Hz, for which LPL is equal to 94 A/m for an eight hour working shift, individual harmonics H_{300} = 896 A/m and H_{600} = 179 A/m were found, which greatly exceed LPL. It shows that if the welder is close to the cable (wraps it around his body or winds it on the arm holding the electrode), it will be hazardous for his health.

Investigations of MF intensity (Table 4) in semi-automatic CO_2 welding with Sv-08G2S wire showed that MF LPL are exceeded in all the studied zones of the welder's body in the frequency range of 50–1000 Hz.

Table 2. Results of determination of magnetic field intensity in automatic submerged-arc welding with AN-65 flux (wire diameter of 4.0 mm, TS-17automatic machine, current source — TDF-1002 transformer, alternating current, 700 A, 36 V)

Spectral composition of the magnetic field and amplitudes of harmonic components H_{mn} in measurement zones by frequency ranges, A/m														
Measurement zones														
1 (forehead)			2 (breast)			3 (abdomen)			4 (wrist)			5 (cable)		
Frequency ranges, Hz														
0–5	5–50	50–1000	0–5	5–50	50–1000	0–5	5–50	50–1000	0–5	5–50	50–1000	0–5	5–50	50–1000
1	2	3	1	2	3	1	2	3	1	2	3	1	2	3
H_5 = 83	H_{50} = 12	H_{100} = 62	H_5 = 130	H_{50} = 210	H_{100} = 98 H_{150} = 70 H_{200} = 48	H_5 = 230	H_{50} = 360	H_{100} = 180 H_{150} = 150	*	*	*	*	*	*
Note. * in this frequency range no magnetic field signal was found.														

Table 3. Results of determination of magnetic field intensity at manual arc welding with ANO-21 electrodes (electrode diameter of 4.0 mm, current source is VDU-506 rectifier, direct current of 200–220 A, 32–34 V)

Spectral composition of the magnetic field and amplitudes of harmonic components H_{mn} in measurement zones by frequency ranges, A/m														
Measurement zones														
1 (forehead)			2 (breast)			3 (abdomen)			4 (wrist)			5 (cable)		
Frequency ranges, Hz														
0–5	5–50	50–1000	0–5	5–50	50–1000	0–5	5–50	50–1000	0–5	5–50	50–1000	0–5	5–50	50–1000
1	2	3	1	2	3	1	2	3	1	2	3	1	2	3
H_5 = 397	H_{50} = 28	H_{150} = 20 H_{300} = 32 H_{600} = 15	H_5 = 658	H_{50} = 40	H_{100} = 49 H_{150} = 64 H_{250} = 31 H_{300} = 82 H_{450} = 15	H_5 = 2386	H_{25} = 283 H_{50} = 159	H_{100}=127 H_{300} = 710 H_{400} = 113 H_{500} = 113	H_5 =1531	H_{50} = 113	H_{100} = 50 H_{300} = 357 H_{500} = 43	H_5 = 3977	H_{25} = 253	H_{100} = 90 H_{150} = 56 H_{200} = 63 H_{300} = 896 H_{350} = 23 H_{400} = 25 H_{425} = 15 H_{500} = 21 H_{600} = 179

Presence of such a large number of harmonics in this frequency range is attributable to the influence of the characteristics of the welding process proper on MF signal shape. In particular, the MF signal shape is influenced by the features of arc burning, nature of electrode metal transfer in the arc gap, and, certainly, by the initial parameters of the welding arc power source. The welding process can be characterized by the presence of the arc gap short-circuiting, size of molten metal drops and other factors [10], which affect the frequency of the generated MF.

The results of determination of the intensity of MF, generated in manual nonconsumable electrode argon-arc welding of steel, using MAGIC WAVE-3000 current rectifier (Austria), are given in Table 5. These results are indicative of a complete absence of exceeding the MF level in all the frequency ranges and zones of the welder's body. This is attributable to improved electric characteristics of the above-mentioned modern current rectifier with welding current modulation.

At the same time, presence of MF signal of the magnitude of 160 A/m (H_{320}) in the frequency range of 50–1000 Hz, in the zone of the wrist, with which the welder holds the electrode (see Figure 1), does not mean that LPL is exceeded. It is attributable to the fact that in keeping with the sanitary standards in the case of local MF action on the wrists the following multiplying coefficient is used:

Table 4. Results of determination of magnetic field intensity at semi-automatic CO_2 welding (Sv-08GS wire of 1.2 mm diameter, current source is VDG-3-3 rectifier, direct current of 220 A, 20–22 V)

Spectral composition of the magnetic field and amplitudes of harmonic components H_{mn} in measurement zones by frequency ranges, A/m														
Measurement zones														
1 (forehead)			2 (breast)			3 (abdomen)			4 (wrist)			5 (cable)		
Frequency ranges, Hz														
0–5	5–50	50–1000	0–5	5–50	50–1000	0–5	5–50	50–1000	0–5	5–50	50–1000	0–5	5–50	50–1000
1	2	3	1	2	3	1	2	3	1	2	3	1	2	3
H_5 = 477	*	H_{75} = 318 H_{200} = 202 H_{300} = 126 H_{400} = 51 H_{480} = 63 H_{600} = 32	H_5 = 560	H_{46} = 356	H_{66} = 226 H_{80} = 253 H_{210} = 224 H_{232} = 126 H_{266} = 89 H_{276} = 63 H_{300} = 561 H_{350} = 80	H_5 = 1193	H_{46} = 450	H_{56} = 450 H_{114} = 316 H_{134} = 201 H_{158} = 201 H_{178} = 201 H_{184} = 201 H_{222} = 201 H_{300} = 201	H_5 = 768	H_{20} = 127 H_{40} = 318	H_{60} = 357 H_{120} = 253 H_{186} = 253 H_{216}=143 H_{242}=113 H_{276}=113 H_{300}=159 H_{350}=127 H_{400}=63 $H_{462=}$71 H_{520}=51	*	*	*
Note. * in this frequency range no magnetic field signal was found.														

Table 5. Results of determination of magnetic field intensity at manual nonconsumable electrode argon-arc welding (electrode diameter of 3.0 mm, current source is MAGIC WAVE-3000 rectifier (Austria), direct current of 100 A, 10 V)

Spectral composition of the magnetic field and amplitudes of harmonic components H_{mn} in measurement zones by frequency ranges, A/m														
Measurement zones														
1 (forehead)			2 (breast)			3 (abdomen)			4 (wrist)			5 (cable)		
Frequency ranges, Hz														
0–5	5–50	50–1000	0–5	5–50	50–1000	0–5	5–50	50–1000	0–5	5–50	50–1000	0–5	5–50	50–1000
1	2	3	1	2	3	1	2	3	1	2	3	1	2	3
$H_5 = 416$	$H_{25} = 33$	$H_{85} = 45$ $H_{100} = 35$ $H_{115} = 45$ $H_{295} = 20$	$H_5 = 310$	*	*	$H_5 = 636$	$H_{40} = 21$	$H_{95} = 29$ $H_{160} = 29$ $H_{270} = 40$ $H_{320} = 80$	$H_5 = 1081$	$H_{40} = 39$	$H_{95} = 49$ $H_{160} = 51$ $H_{290} = 71$ $H_{320} = 160$ $H_{550} = 41$	*	*	*
Note. * in this frequency range no magnetic field signal was found.														

$$H_{\text{LP LOC}} = 5H_{\text{LPGEN}}, \quad (4)$$

where $H_{\text{LP LOC}}$ is the LPL of a variable magnetic field of 50 Hz frequency at local impact (wrists); $H_{\text{LP GEN}}$ is the LPL of a variable magnetic field at general impact [8].

Therefore, in this case LPL is not exceeded: this harmonic is located much lower than the permissible level of 470 A/m, which is lower than LPL. Thus, for manual argon-arc welding at direct current the standard MF values are not exceeded even at an eight hour exposure.

The low MF levels in this case are attributable to application of a low direct current and low arc voltage, as well as the features of MAGIC WAVE-3000 current rectifier.

On the other hand, in these experiments manual nonconsumable electrode argon-arc welding was performed without filler wire. Now in other experiments at filler feeding into the arc gap additional modulation of MF signal and complication (by the number of harmonics) of its spectrum are possible due to wave processes.

Obtained results show that in semi-automatic CO_2 metal-arc welding MF are generated in the welder workplace, which exceed LPL in the frequency range of 50–1000 Hz. This is due, predominantly, to the presence in the induced MF composition of rather intensive high-frequency (compared to 50 Hz frequency) harmonic signals, as MF norm in this frequency range, decreases abruptly (becomes more stringent) by approximately 15 times in keeping with the regulations [8].

The spectrum of all the studied welding processes is characterized by presence in MF signals of components with the main (first) of harmonics of 20, 50, 60, 300 Hz, multiple to primary frequencies and combination frequencies. The origin of these harmonics in arc welding can be attributed to the following features of the welding process:

- 20–25 Hz is the frequency of the arc gap short-circuiting, arising during metal-electrode CO_2 welding;
- 50 Hz is the frequency of the mains voltage, powering the welding transformer, rectifier, inverter, etc.;
- 60 Hz is the frequency of voltage in the secondary circuit of foreign arc power sources (for instance, MAGIC WAVE-2600);
- 300 Hz is the frequency of the first harmonic of the alternating component of rectified voltage at application of a six-phase circuit of alternating current rectification.

We should be also take into account the influence on MF shape of filler wire, used in all of our experiments, except for manual nonconsumable electrode welding in argon, which promotes additional modulation of MF signal and makes its spectrum more complicated.

Analyzing the regularities of running of the welding processes, it becomes clear that the spectral composition of the signal of MF generated by the welding equipment is predominantly determined by two principally inseparable factors:

- welding process proper, features of arc burning and mode of electrode metal transfer in the arc gap;
- output parameters of welding arc power sources: transformers, rectifiers, as well as additional electric devices included into the welding circuit (choke, capacitors, stabilizers, oscillators; arc ignition devices, ballast rheostats, etc).

It is natural that for developers of electric welding equipment of greatest interest is the method of lowering the intensity of higher harmonics due to weakening of the influence of the second factor. Therefore, from the viewpoint of electromagnetic safety, the developers of such equipment should reduce the steepness of the rising front of current and voltage pulses in welding arc power sources, operating in key modes. When designing the power sources, it is necessary to find compromise solutions, selecting some optimal values of the converter working frequency and welding current pulse shape. As regards the influence of the methods of manual and semi-automatic welding

proper on MF frequency spectrum and intensity in the working zone, in our opinion, it is necessary to:

● constantly limit application of processes with short-circuiting of the arc gap, and wider apply welding in gas mixtures (Ar + CO_2, Ar + O_2, Ar + O_2 + CO_2) by small-diameter wires, which will ensure absence of these short-circuits;

● consider (in terms of hygiene) the applicability of other welding and surfacing processes with welding mode modulation, in order to achieve a more stable and predictable process of MF generation;

● apply automation and robotization of the welding processes.

CONCLUSIONS

1. The necessary conditions for measuring the levels of MF, generated by welding equipment, for their correct hygienic assessment, were determined. It is shown that for objective assessment of the magnetic field levels, the net welding time should be 2 hours per shift.

2. Results of hygienic assessment of the magnetic fields, in keeping with the new standards, are as follows:

● semi-automatic CO_2 metal-arc welding is characterized by exceeding the limit permissible level of the magnetic field in the frequency range of 50–1000 Hz;

● at automatic submerged-arc welding there is no exceeding of the limit permissible levels of individual magnetic field harmonics, but the total value of all the harmonic components of the magnetic field is exceeded;

● manual nonconsumable electrode DC argon-arc welding is characterized by a medium level of the magnetic field in the workplace;

● during manual coated-electrode arc welding the magnetic field level is exceeded only in the electrode cable proper.

To minimize the harmful impact of the magnetic field on welders, the following recommendations should be followed (as far as possible):

● increase the distance from the power source and welding equipment to the welder's body;

● avoid the electrode or return cable wrapping around the worker's body;

● avoid the welder's body being between the electrode cable and any other cable; all the cables should be kept together from one or the other side.

REFERENCES

1. Pačaiová, H., Oravec, M., Šmelko, M. et al. (2018) Extra low frequency magnetic fields of welding machines and personal safety. *J. of Electrical Eng.*, 69(**6**), 493–496. https://sciendo.com/pdf/10.2478/jee-2018-0084
2. Michałowska, J., Przystupa, K., Krupski, P. (2020) Empirical assessment of the MAG welder's exposure to an electromagnetic field. *Przegląd Elektrotechniczny*, **96**. DOI: https://doi.org/10.15199/48.2020.12.48
3. Modenese, A., Gobba, F. (2021) Occupational exposure to electromagnetic fields and health surveillance according to the European Directive 2013/35/EU. *Inter. J. of Environmental Research and Public Health*, 18(**4**), 1730. DOI: https://doi.org/10.3390/ijerph18041730
4. Stam, R. (2018) *Comparison of international policies on electromagnetic fields (power frequency and radiofrequency fields)*. Publication of the National Institute of Public Health and the Environment, Bilthoven, Netherlands. https://rivm.openrepository.com/bitstream/handle/10029/623629/2018998.pdf?sequence=1
5. Fuentes, M.A., Trakic, A., Wilson, S J., Crozier, S. (2008) Analysis and measurements of magnetic field exposures for healthcare workers in selected MR environments. *IEEE Transact. on Biomedical Eng.*, 55(**4**), 1355–1364. DOI: https://doi.org/10.1109/TBME.2007.913410
6. Yamaguchi-Sekino, S., Ojima, J., Sekino, M. et al. (2011) Measuring exposed magnetic fields of welders in working time. *Industrial Health*, 49(**3**), 274–279. DOI: https://doi.org/10.2486/indhealth.MS1269
7. Levchenko, O., Polukarov, Y., Goncharova, O. et al. (2022) Determining patterns in the generation of magnetic fields when using different arc welding techniques. *Eastern-European J. of Enterprise Technologies*, **2**, 10(116), 50–56. DOI: https://doi.org/10.15587/1729-4061.2022.254471
8. (2002) DSN 3.3.6.096-2002: *Intensity of electromagnetic fields of commercial frequency.* Kyiv, MOZ, 16. https://zakon.rada.gov.ua/laws/show/z0203-03#Text [in Ukrainian].
9. (1986) *Maximum permissible level of magnetic fields of 50 Hz frequency*. Moscow, No. 3206-85, 17.01.85, 7. https://docs.cntd.ru/document/1200031592
10. Potapievsky, A.G. (2007) *Consumable electrode shielded-gas welding.* Pt 1: Welding in active gases. 2nd Ed. Kyiv, Ekotekhnologiya. https://themechanic.ru/wp-content/plugins/download-attachments/includes/download.php?id=13675

ORCID

O.G. Levchenko: 0000-0002-9737-7212,
Yu.O. Polukarov: 0000-0002-6261-3991,
O.M. Honcharova: 0000-0002-5213-6300,
O.M. Bezushko: 0000-0002-6148-1675

CONFLICT OF INTEREST

The Authors declare no conflict of interest

CORRESPONDING AUTHOR

O.G. Levchenko
E.O. Paton Electric Welding Institute of the NASU
11 Kazymyr Malevych Str., 03150, Kyiv, Ukraine.
E-mail: levchenko.opcb@ukr.net

SUGGESTED CITATION

O.G. Levchenko, Yu.O. Polukarov, O.M. Honcharova, O.M. Bezushko (2023) Hygienic characteristic of magnetic fields at different arc welding methods. *The Paton Welding J.*, **2**, 34–40.

JOURNAL HOME PAGE

https://patonpublishinghouse.com/eng/journals/tpwj

Received: 25.02.2023
Accepted: 30.03.2023

DOI: https://doi.org/10.37434/tpwj2023.02.06

INFLUENCE OF EXTERNAL LONGITUDINAL MAGNETIC FIELD ON FORMATION OF ESR INGOT SURFACE

V.B. Porokhonko, I.V. Protokovilov, D.A. Petrov

E.O. Paton Electric Welding Institute of the NASU
11 Kazymyr Malevych Str., 03150, Kyiv, Ukraine

ABSTRACT

The influence of permanent and pulsed longitudinal magnetic fields with the induction B = 0.16–0.30 T on the quality of outer surfaces of titanium ingots of 85 mm diameter, produced by ESR process, was studied. It is shown that alongside the positive effects of magnetic field action, manifested in increase of ESR process efficiency, improvement of chemical homogeneity of the ingots, and refinement of their crystalline structure, application of magnetic fields leads to deterioration of the quality of formation of the ingot side surface. Here, the degree of surface deterioration depends on magnetic field induction and duration of its pulses. It is found that application of pulsed magnetic fields leads to deterioration of the ingot surfaces to a smaller extent than application of permanent magnetic fields. Described are the mechanisms which negatively affect the quality of ingot surface formation under the impact of the longitudinal magnetic field. They consist in removal and solidification of electrode drops near the mould walls and periodical change of the skull crust thickness as a result of the slag and metal pool melt vibration.

KEYWORDS: electroslag remelting; longitudinal magnetic field; pulsed field; ingot; surface; titanium

INTRODUCTION

External magnetic fields are an effective tool for controlling heat transfer and crystallization of metal in ESR [1–6]. The advantage of using them consists in the possibility of a contact-free force effect on the melts of slag and metal pools to achieve certain metallurgical effects. In particular, in [3–6] the possibility of refinement of crystalline structure and increasing the chemical and physical homogeneity of ESR ingots using external magnetic fields was shown. It was established, that under the action of pulsed longitudinal magnetic field in the metallurgical melt, electric eddy currents and vibrations are formed, which provide intensive stirring of liquid metal, intensify the processes of melting of a consumable electrode, contribute to refinement of crystallites formed in a two-phase zone, and the formation of new crystallization centres. This leads to a number of positive effects, expressed in an increased the chemical homogeneity of ingots, refinement of their crystalline structure and enhancing the efficiency of the ESR process. Because of this, the use of magnetic fields at ESR allowed producing titanium alloys, whose cast structure is approaching the structure of a wrought metal.

It was also found that the action of external magnetic fields can lead to a deterioration of the quality of formation of a side surface of the ingots.

Figure 1 shows the appearance of a titanium ingot with a diameter of 65 mm, the lower part of which is melted without the use of magnetic field and the upper one is melted using a permanent longitudinal magnetic field with the induction of 0.25 T. The photo clearly shows the boundary of this interface. In particular, the lower part of the ingot produced without a superposition of the magnetic field is characterized by an excellent quality of surface formation. However, the ingot surface produced using a magnetic field is characterized by the presence of significant cavities, slag inclusions and corrugations. It is quite obvious that the further use of ingots with such a surface requires their mechanical treatment with a large amount of wastes.

Figure 1. Titanium ingot with a diameter of 65 mm, melted without (*1*) and with the use (*2*) of a longitudinal magnetic field with an induction of 0.25 T

The aim of this work is to study the effect of longitudinal permanent and pulsed magnetic fields on the formation of ESR surface ingots and determine the mechanisms that lead to a deterioration of surface quality.

MATERIALS AND RESEARCH PROCEDURE

Experimental studies were performed during melting of commercial titanium VT1-0 of 85 mm diameter with the use of different parameters of a longitudinal magnetic field.

Figure 2 shows the appearance of ingots, melted in the conditions of a permanent magnetic field with the induction of 0.16–0.30 T. The analysis of the obtained data shows that under other things being equal, the quality of the surface deteriorates with an increase in the induction of the magnetic field. If at 0.16 T, the surface of the ingot is satisfactory (Figure 2, *a*), then when it grows to 0.24–0.30 T, on the surface of the ingots, defects in the form of slagging, cavities, corrugations, etc. are formed with the depth of up to 1.5–2.0 mm (Figure 2, *b*, *c*).

The further experiments were performed under the conditions of a pulsed longitudinal magnetic field. Both induction of the magnetic field (within the ranges B = 0.16–0.24 T), as well as the duration of pulses and pauses of its action (within the ranges of t_{pulse} = = 0.3–21 s, t_{pause} = 10–33 s respectively) were changed.

Figure 3, *a–c* presents ingots produced at the same induction of the magnetic field (0.24 T), but with different duration of pulses of its action t_{pulse} = 0.3–2.0 s. The duration of pauses in all cases was equal to t_{pause} = 10 s.

The obtained results showed that with the duration of pulses of the magnetic field t_{pulse} = 0.3 s, their effect on the quality of the ingot surface is almost unnoticeable (Figure 3, *a*). On the surface of the ingot, the traces of the magnetic field action are barely visible. This suggests that with such a small duration of field pulses, in the metallurgical pool enough powerful hydrodynamic currents, that would affect the quality of the ingot surface, do not have time to form. However, as the pulse duration is increased to t_{pulse} = 1–2 s, corrugation is already noticeable on the surfaces of the ingots, which grows with an increase in the duration of the magnetic field pulses (Figure 3, *b–d*). In general, with the duration of pulses of up to 1.5 s, the surface of the ingots can be considered as good (Figure 3, *a–c*).

In the further experiments, the value of the magnetic field induction was reduced to 0.22–0.16 T, and the duration of pulses and pauses of the magnetic field was increased to t_{pulse} = 11–21 and t_{pause} = 21–33 s, respectively (Figure 3, *e–g*). In this case, on the surface of the ingots, zones of action of the magnetic field are clearly visible, which were manifested in the form of transverse bands (corrugations). The depth of such corrugations was up to 1–2 mm, and the height was 2–5 mm, and with an increase in the duration of pulses of magnetic field, the depth and length of these zones increased (Figure 3, *f*, *g*).

It should be emphasized that the effect of the pulsed magnetic field on the formation of surfaces with a lower induction (B = 0.16 T), but with the longer pulse duration (t_{pulse} = 21 s) (Figure 3, *g*) is higher than at the induction B = 0.24 T and the duration of the pulse action t_{pulse} = 1 s (Figure 3, *b*). Obviously, the explanation for such a phenomenon may be the results of physical modeling, which show that for the formation of hydrodynamic flows of the maximum in-

Figure 2. Appearance of titanium ingots, melted by ESR using a longitudinal permanent magnetic field of a different induction, T: *a* — 0.16; *b* — 0.24; *c* — 0.30

Figure 3. Appearance of titanium ingots, melted by ESR with the use of a longitudinal pulsed magnetic field: *a* — B = 0.24 T, t_{pulse} = = 0.3 s, t_{pause} = 10 s; *b* — B = 0.24 T, t_{pulse} = 1.0 s, t_{pause} = 10 s; *c* — B = 0.24 T, t_{pulse} = 1.5 s, t_{pause} = 10 s; *d* — B = 0,24 T, t_{pulse} = 2.0 s, t_{pause} = 10 s; *e* — B = 0,22 T, t_{pulse} = 11 s, t_{pause} = 21 s; *f* — B = 0.16 T, t_{pulse} = 11 s, t_{pause} = 33 s; *g* — B = 0.16 T, t_{pulse} = 21 s, t_{pause} = 33 s

tensity in the slag pool, the duration of the magnetic field pulse should exceed some value, which for the ingots of the corresponding diameters (60–100 mm) is about 2.5 s [7, 8]. At a lower pulse duration, the flow intensity will be lower and, therefore, the impact on the surface formation will also be lower.

Thus, when applying a pulsed magnetic field, the formation of the ingot surface is affected not only by the value of the magnetic field induction, but also by the duration of pulses and pauses of its action.

It is obvious, that the mechanisms of effect of the magnetic field on the formation of ESR ingots are associated with the power action of the magnetic field on the melts of slag and metal. This action occurs as a result of the interaction of the longitudinal magnetic field with the electric current of melting. As a result of such interaction in the current-carrying melts of slag and metal, a volumetric electromagnetic force (Lorentz force) is formed, which leads to the movement or vibration of liquid slag and metal.

Directly the mechanisms of deterioration of the formation quality of the ingot surface can be associated with periodic changes in the thickness and destruction of the skull crust on the surface ingot, caused by the vibrations of the melt, and also by the spread of electrode metal drops and their solidification on the mould walls and the ingot surface (Figure 4).

Thus, during physical modeling of the drop transfer at ESR, it was found that a longitudinal magnetic field can lead to twisting and spreading drops of electrode metal in the slag pool and their removal to the mould walls [7, 8]. In this case, during ESR, drops of electrode metal will be subjected to intensive cooling and crystallize near the walls of the mould or in the skull crust on the ingot surface, which will lead to deterioration of the quality of its formation (Figure 4, *b*, *c*).

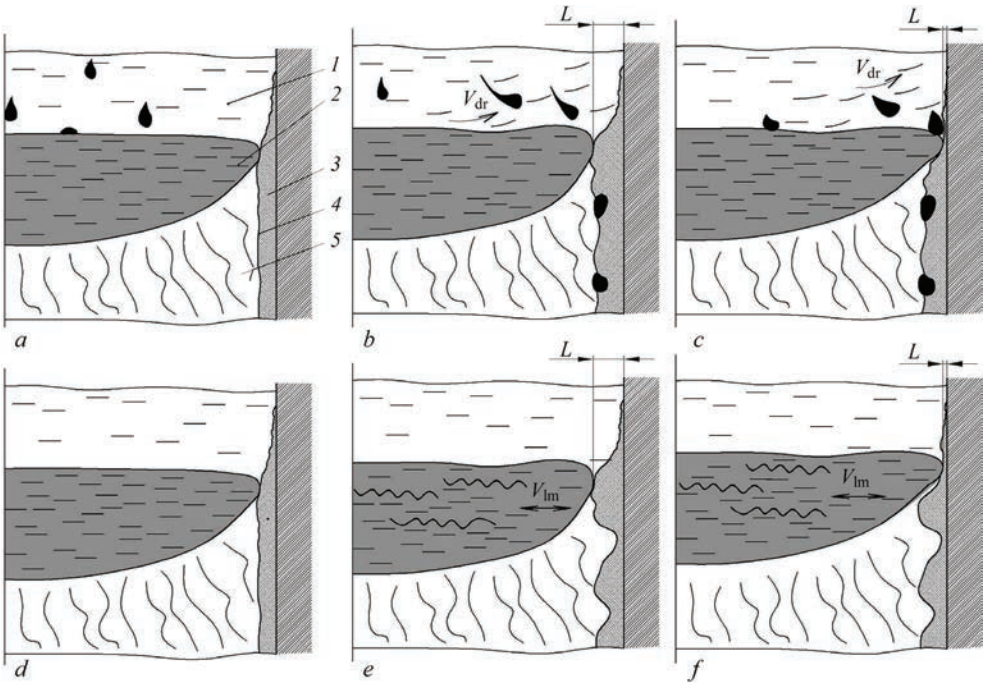

Figure 4. Mechanisms of deterioration of the surface of ESR ingots when using a longitudinal magnetic field due to chaotically spread drops (*a*–*c*) and vibration of melts of slag and metal pools (*d*–*f*): *1* — slag pool; *2* — metal pool; *3* — skull crust; *4* — ingot surface; *5* — ingot; *L* — thickness of the skull crust; V_{dr} — movement of electrode metal drops; V_{lm} — vibration of liquid metal

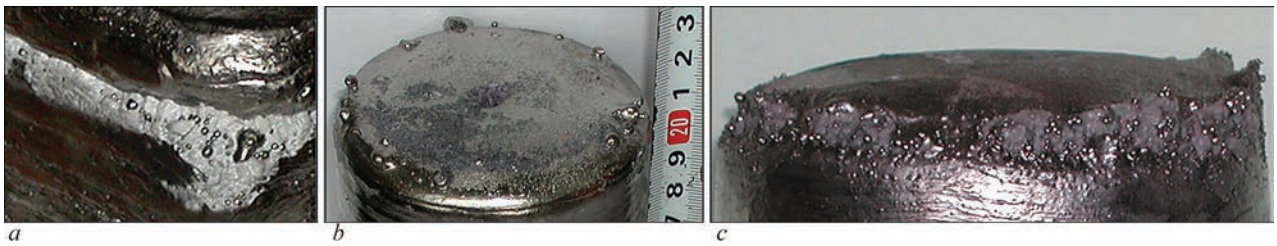

Figure 5. Electrode metal drops in ESR in a magnetic field: *a* — in a slag crust; *b*, *c* — in the peripheral sections on the ingot surface

The high probability of the mechanism described above is indicated by the detection of electrode metal drops in slagging (Figure 5, *a*) and directly on the surface of the ingots that were melted in a magnetic field (Figures 5, *b*, *c*).

Another mechanism of deterioration of the ingot surface may be associated with the vibration of the melts of slag and metal pools due to the action of the magnetic field (Figure 4, *d*, *f*). Such vibration with a frequency of 50 Hz is formed at the interaction of alternating current of melting with a permanent magnetic field. When the pulsed magnetic field is used, the vibration is enhanced by the hydrodynamic shocks that occur at the moment of switching on/off the magnetic field. Such oscillations in slag and metal pools lead to a chaotic change in the thickness of the skull crust *L* (Figure 4, *e*, *f*) and to the deterioration of the quality of the ingot surface formation.

It is quite possible that the mechanisms described above operate simultaneously and lead to a deterioration of the quality of ESR ingot surface formation under the effect of a longitudinal magnetic field.

CONCLUSIONS

1. It is shown that the use of an external longitudinal magnetic field in ESR along with the positive effects (enhancing the efficiency of the ESR process, increasing the chemical and structural homogeneity of the ingots) has also a negative impact, which manifests in the deterioration of the quality of formation of the reverse side ingot surface. Moreover, the degree of deterioration of the ingot surface depends on the type and parameters of the magnetic field.

2. It is established that at an increase in the magnetic field induction and the duration of pulses of its action, the quality of the surface formation deteriorates, as well as the use of pulsed magnetic fields to a lesser extent leads to a deterioration of the ingot surface and is manifested only in the form of transverse bands. Their depth and elongation depend on the parameters of the pulsed magnetic field. At a short duration of magnetic field pulses, its negative impact on the formation of the ingot surface is hardly noticeable. It can be assumed that the mechanisms of surface deterioration consist in removing drops to the walls of

the mould and their solidification there, as well as associated with the action of vibration of the melts of slag and metal pools on the formation of a skull crust on the ingot surface.

3. This article did not consider the positive effect of the longitudinal magnetic field on the structure formation of metal and its chemical homogeneity. However, in real conditions of ESR, obviously it is necessary to determine the ratio of the degree of deterioration of the ingot surface to the effectiveness of improving the inner characteristics of ESR ingots produced under the effect of external magnetic field.

REFERENCES

1. Dudko, D.A., Rublevsky, I.N. (1960) Electromagnetic stirring of slag and metal pool in electroslag process. *Avtomatich. Svarka*, **9**, 12–16 [in Russian].
2. Trochun, I.P., Chernysh, V.P. (1965) Magnetic control of crystallization in ESR. *Svarochn. Proizvodstvo*, **11**, 3–5 [in Rusian].
3. Paton, B.E., Medovar, B.I., Us, V.I., Tomilenko, S.V. (1989) Development and examination of methods of control of ESR crystallizing ingot structure by magnetic field superposition. *Problemy Spets. Elektrometallurgii*, **4**, 3–7 [in Russian].
4. Kompan, Ya.Yu., Protokovilov, I.V. (2002) Some technological aspects of magnetically-controlled electroslag melting (MEM) of titanium alloys. In: *Proc. of Int. Sci.-Tech. Conf. on Special Metallurgy: Yesterday, Today, Tomorrow (Ukraine, Kyiv, 8–9 October 2002)*. 256–262.
5. Kompan, Ya.Yu., Nazarchuk, A.T., Protokovilov, I.V. (2007) Towards the problem of intensification of electromagnetic action in magnetically-controlled electroslag melting of titanium alloys. *Advances in Electrometallurgy*, **4**, 3–7.
6. Kompan, Ya.Yu., Nazarchuk, A.T., Protokovilov, I.V., Petrov, D.A. (2012) Possibilities of application of pulsed electromagnetic effects in electroslag processes. *Advances in Electrometallurgy*, **2**, 8–13.
7. Protokovilov, I., Shapovalov, V., Porokhonko, V. et al. (2021) Effect of the longitudinal magnetic field on the droplets evolution during electroslag remelting process. *Magnetohydrodynamics*, 57(**4**), 559–568. DOI: https://doi.org/10.22364/mhd.57.4.10
8. Protokovilov, IV., Porokhonko, V.B. (2017) Physical modeling of electrode metal drop transfer in ESM with superposition of pulsed magnetic fields. *Suchasna Elektrometal*., **3**, 9–13 [in Ukrainian]. DOI: https://doi.org/10.15407/sem2017.03.02

ORCID

V.B. Porokhonko: 0000-0002-6490-7221,
I.V. Protokovilov: 0000-0002-5926-4049,
D.A. Petrov: 0000-0003-2937-9299

CONFLICT OF INTEREST

The Authors declare no conflict of interest

CORRESPONDING AUTHOR

V.B. Porokhonko
E.O. Paton Electric Welding Institute of the NASU
11 Kazymyr Malevych Str., 03150, Kyiv, Ukraine.
E-mail: lab38@paton.kiev.ua

SUGGESTED CITATION

V.B. Porokhonko, I.V. Protokovilov, D.A. Petrov (2023) Influence of external longitudinal magnetic field on formation of ESR ingot surface. *The Paton Welding J*., **2**, 41–45.

JOURNAL HOME PAGE

https://patonpublishinghouse.com/eng/journals/tpwj

Received: 29.09.2022
Accepted: 30.03.2023

DOI: https://doi.org/10.37434/tpwj2023.02.07

SURFACE EDDY CURRENT PROBES OF DOUBLE DIFFERENTIAL TYPE AS AN EFFECTIVE TOOL TO SOLVE NON-DESTRUCTIVE INSPECTION PROBLEMS

V.M. Uchanin

G.V. Karpenko Physico-Mechanical Institute of the NASU
5 Naukova Str., 79060, Lviv, Ukraine

ABSTRACT

A new type of surface eddy current probes of double differential type, which are characterized by increased sensitivity to surface and subsurface defects of various types, is presented. A family of double differential eddy current probes of different diameters with different spatial resolutions has been developed. The paper analyzes the main features of double differential eddy current probes and presents new innovative inspection techniques which allow solving the most complex problems of non-destructive testing. In particular, the developed eddy current probes have been researched and tested as an effective tool of inspection of multilayered aircraft structures, in which it is necessary to detect internal defects. They provide, in particular, the detection of cracks in the second layer of stratified aircraft structures or cracks on the back surface of the aircraft structures skin; detection of subsurface defects in the weld zone with a rough surface; detection of cracks through repair patches made of aluminium alloy or carbon composite; detection of subsurface cracks near rivet holes, etc. These techniques create unique opportunities for timely detection of dangerous damage without disassembling the inspected object or removing the protective coating. The developed eddy current probes are effective for detecting cracks in ferromagnetic steel products such as forgings, gas turbine blades and shafts, rails, wheels or axles of railway rolling stock, rough-surfaced castings, etc. In addition, high sensitivity to defects can be achieved even during the inspection through an air gap or dielectric coating. This allows them to be successfully used in many automated inspection systems.

KEYWORDS: nondestructive testing, eddy current probe of double differential type, stratified aircraft structure, subsurface defect, repair patches, rivet hole

INTRODUCTION

Eddy current (EC) method of non-destructive testing (NDT) is one of the most widespread for detection of surface and subsurface defects and determination of the characteristics of conductive materials [1-9]. At the beginning of its development the EC method was mainly used for detection of surface defects due to high operating frequencies which were used in the first EC flaw detectors. This resulted in the concentration of alternating current in the external layers of the conductive material due to skin-effect [10, 11]. Later on the low operating frequencies started to be used that expanded a sphere of application of the EC method and allowed detecting hidden subsurface defects including in multilayer structures of aircrafts. Eddy current probes (ECP) being commonly used in EC testing practice are divided on two main types, namely absolute and differential [3–5, 8]. Several decades ago a new type of surface ECP named double differential ECP [8, 12, 13] was created at G.V. Karpenko Physico-Mechanical Institute of the NASU (PMI) for the purpose of improvement of EC testing selectivity. The experience of their application showed that these ECP can solve the tasks, which are difficult (and sometimes impossible) to solve using traditional ECP of absolute or differential type. Proposed ECP of double differentiatial type are characterised with increased sensitivity to surface and subsurface defects of different type which appear during manufacture of a product or initiated by fatigue or corrosion phenomena in an operated structures. There was developed a family of double differential ECP of different diameter with various spatial resolution. Its content is constantly expanded [8]. Developed ECP were examined and tested as an effective tool of NDT of typical aircraft multilayer structures (AS), where it is necessary to detect inner defects. They, in particular, provide detection of cracks in a second layer of multilayer AS or cracks on reverse surface of AS skin with decrease of effect of reinforcing band edge; detection of subsurface defects in weld zone with rough surface; detection of cracks through repair patches, made of aluminium alloy or carbon composite; detection of subsurface cracks near rivet holes etc. These technologies create unique possibilities for timely detection of dangerous damages without disassembly of a tested object (TO) or removal of a protective coating [8, 12, 13]. Besides, developed ECP are efficient for detection of cracks in ferromagnetic steel products such as forgings, blades or shafts of gas turbines, rails, wheels or axes of railway rolling stock, castings with rough-finished surface, etc. [8]. The double differential ECP, for example, is used in the mechanized 8-channel unit for crack detection in welds of ferromagnetic alloys through dielectric protective coating of 4 mm thick-

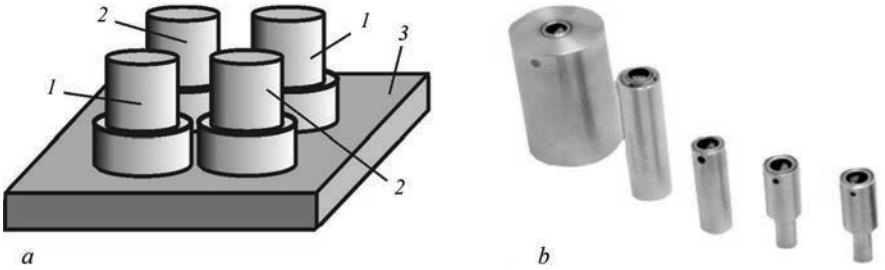

Figure 1. Design of double differential ECP (*a*): *1* — drive coils; *2* —sensing coils; *3* — TO; double differential ECP of different size and spatial resolution (*b*)

ness developed by German Company Test Maschinen Technik GmbH. At that high sensitivity to defects can be reached even at testing through air gap or dielectric coating of up to 10 mm thickness. Thanks to this peculiarity double differential ECP are successfully used in many automated NDT systems, for example, in the 64-channel EC testing system for detection of defects of aluminium bands developed at Fraunhofer Institute for Non-destructive Testing (Saarbrücken, Germany), multichannel NDT systems for wheel pairs and railway axes, developed at the Ukrainian Institute for Non-Destructive Testing (Kyiv) etc. [8].

This paper analyses the main peculiarities of the double differential ECP and provides new innovative technologies of EC NDT which allow solving the most complex NDT problems.

DESIGN OF DOUBLE DIFFERENTIAL ECP AND MAIN PECULIARITIES OF FORMATION OF SIGNALS FROM DEFECTS

Double differential ECP consist of two drive coils *1* and two sensing coils *2*, installed on the ferrite cores and located in the corners of a square (Figure 1, *a*) [8]. Two drive coils *1* have a series connection and oriented for generation of the similar and opposite primary electromagnetic fields. Developed ECP were mounted in a casing from aluminium alloy in order to reduce electronic interferences and provided with the connectors of different type for work with the flaw detectors of the leading manufacturers of devices for EC testing (Figure 1, *b*).

Design of the double differential ECP (Figure 1, *a*) creates the important peculiarities for distribution of a primary and secondary electromagnetic field, created by eddy currents induced in TO (Figure 2). In particular, a typical neutral plane is created in a zone between the drive coils. In it a vertical component of a total electromagnetic field equals zero (shown in Figure 2, *a* by dotted line) [8]. The sensing ECP coils are installed in the neutral plane and they have sensitivity orientation to a vertical component of the electromagnetic field which equals zero for isotropic and defect-free TO materials. It is important that eddy currents generated by both drive coils have similar direction and thus being added in the neutral plane (Figure 2, *b*) that promotes increase of sensitivity of EC testing. A double differential response of output ECP signal is realised due to counter connection of the sensing coils.

The design of double differential ECP provides deep penetration of eddy currents inside TO material since attenuation of eddy currents can be reduced by means of selection of large diameter of ECP coils of co-axial type or by using the drive and sensing coils of small diameter located at some distance from one another (Figure 1). Thanks to relatively small diameters of the coils it was also obtained a high spatial resolution that is important for detection of local defects. A typical peculiarity of such ECP in comparison with regular ones is a high sensitivity to elongated (crack type) as well as local (such as short crack, corrosion pitting or pore) defects; high sensitivity to surface and subsurface defects including at testing through a non-magnetic skin,

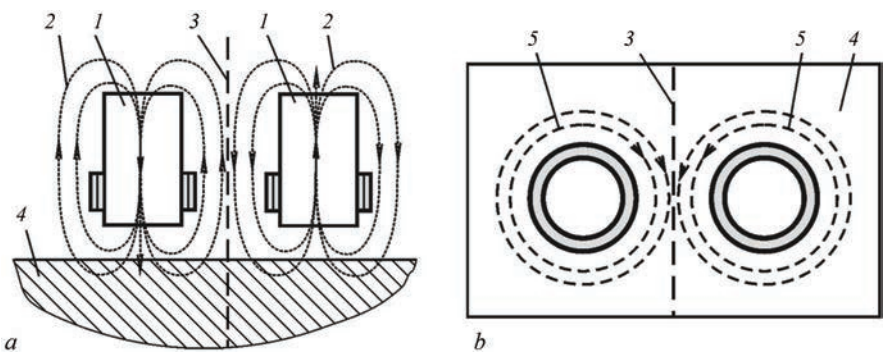

Figure 2. Primary electromagnetic field generated by drive coils (*a*) and corresponding eddy currents (*b*): *1* — ferrite cores; *2* — primary electromagnetic field; *3* — neutral plane; *4* — TO; *5* — eddy currents

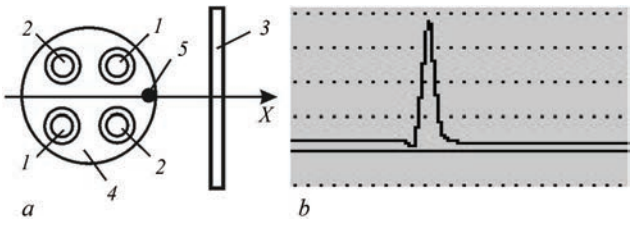

Figure 3. Optimum orientation of double differential ECP relatively to crack direction (*a*): *1*, *2* — drive and sensing coils, respectively; *3* — crack; *4* — casing; *5* — special mark; "quasi-absolute" signal from crack (*b*)

layer of a protective coating or a gap between ECP and TO surface; high testing depth for low-frequency ECP; low level of interferences including caused by effect of lift-off change. There was developed a series of double differential ECP of 4–33 mm diameter that are characterized by different size of the coils, range of operating frequencies and spatial resolution (Figure 1, *b*). Double differential ECP are adapted to modern versatile EC flaw detectors. They provide testing on different operating frequencies in 50 Hz–12 MHz range.

The peculiarity of double differential ECP is a dependence of their sensitivity on crack orientation. The optimum orientation of these ECP relatively to crack direction is shown on Figure 3, *a*, where a line connecting a centre of drive coils is oriented under 45° angle relatively to a crack direction. Special mark on ECP casing helps selecting the optimum orientation. At that a signal from the crack has "quasi-absolute" nature (Figure 3, *b*) similar to an ECP absolute signal which is characterized with the maximum amplitude at a time of ECP location directly over the crack.

Real signals of low-frequency double differential ECP of MDF 1201 type being generated by a subsurface defect in a complex plane of EC impedance of ELOTEST B1 type flaw detector of German Company Rohmann GmbH are presented on Figure 4. A low operating frequency 2 kHz was used for detection of the subsurface defects of crack type located at 1 and 3 mm depth. Sensitivity of EC flaw detector as for a defect lying at 3 mm depth was taken by 10 dB more than for a defect with lying depth 1 mm. In this case the depth of defect lying corresponds the distance between the upper edge of subsurface defect and TO surface. Also for comparison there was given a signal from a gap ("lift-off" on Figure 4) as the main source of the interferences. The lift-off signals are oriented in a complex plane horizontally corresponding to a standard EC testing procedure.

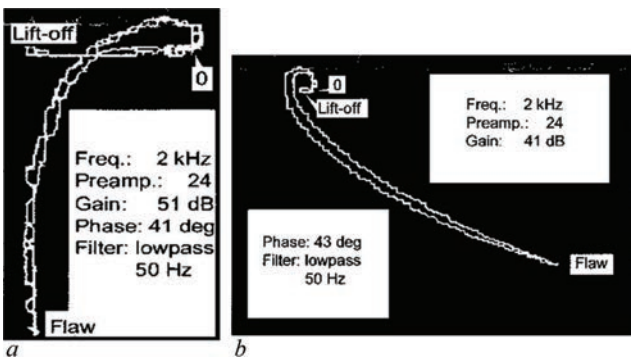

Figure 4. Signal of double differential ECP from subsurface cracks with lying depths 1 (*a*) and 3 mm (*b*)

Provided results show a relatively high sensitivity to subsurface defects with high level of suppression of effect of lift-off change. Even for a defect located at 3 mm depth a relationship of the amplitude of signal from defect to the amplitude of lift-off signal significantly exceeds 6 dB. Besides, the signals differ by phase (direction of signals in a complex plane) that provides additional possibilities for separation of the useful signals created by the defect and lift-off effect.

For local defects, such as pores or corrosion pitting, the double differential ECP create a specific spatial four-point distribution of the signal with two positive and two negative peaks. Figure 5 provides typical experimental distributions of sensitivity obtained using double differential ECP of MDF 1201 type during serial scanning of a zone of local defect simulated by 1 mm diameter hole drilling [8].

DETECTION OF FATIGUE CRACKS IN A SECOND LAYER OF RIVETED AIRCRAFT STRUCTURES

Let us consider a problem of detection of fatigue cracks between the rivets in a second layer of double-layer joints stringer-skin that appeared during AS operation. Such joints are typical for most AS.

The task was to detect in the investigated specimen the cracks between the rivets through 1.4 mm thick upper skin. The distance between the edges of the flush rivets made only 8 mm. Thus, scanning of the zone between the rivets revealed a false signal at defect absence related with rivet hole influence. Figure 6 presents a specimen for adjustment of EC flaw detector. Two trajectories of scanning were used during testing, namely trajectory *5* allows observing the signals at defect absence and trajectory *6* simulates scanning through a crack located in the AS second layer [12].

The main problem at EC testing of such structures is a high level of interferences related to the defect-free rivet influence. Therefore, the testing

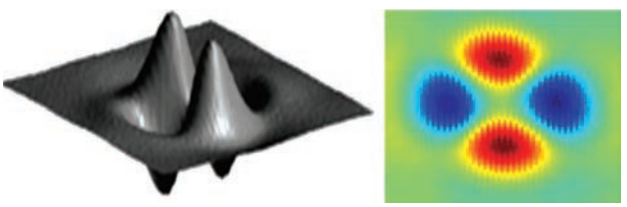

Figure 5. Four-point spatial distribution of signal with two positive and two negative peaks for local defects

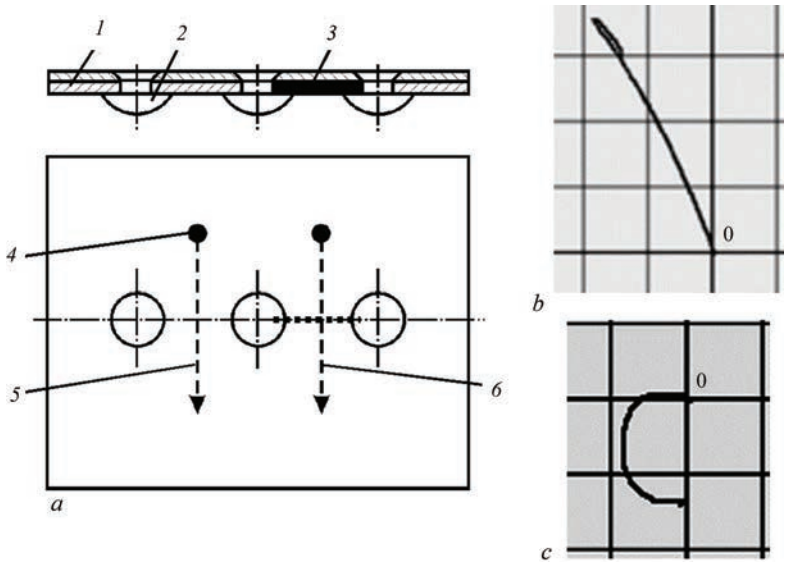

Figure 6. Specimen for simulation of double-layer AS with rivets (*a*): *1* — double-layer structure; *2* — rivets; *3* — crack; *4* — balancing point; *5*, *6* — trajectories of scanning in defect-free and defective zones, respectively; ECP signal in complex plane from crack in second layer (*b*); signal caused by influence of holes of defect-free rivets (*c*)

procedure should separate the defect signals in the second layer from the interference signal created by the rivets. Selective interpreting of the signals can be provided by means of analysis of the features typical for the defect in a complex plane on a flaw detector screen. Developed procedure provides application of ECP of MDF 0602 type of 6 mm diameter, which scans the zone between the rivets (dashed line on Figure 6, *a*). Preliminary an imbalance signal was compensated after ECP installation in point *4* which is located at 10–12 mm distance from a line joining the rivets *2*. The signals were registered using EC board of EDDYMAX type on operating frequency 6 kHz. Figure 6, *b* shows the signals from crack in the second layer and Figure 6, *c* the signals during scanning of defect-free zone between the rivets.

The obtained results indicate that the ECP signals during scanning of a defect-free zone (Figure 6, *c*) move from a balance point ("0" on Figure 6) in a direction of lower part of a complex plane. And vice versa, a signal from the defect has another upward direction into another quadrant of the complex plane (Figure 6, *b*). These results show the possibility of selective EC testing at which useful signals from the defects are easily separated from the signals generated by the rivet holes at defect absence.

DETECTION OF FATIGUE CRACKS CREATED ON AS REVERSE SIDE IN A ZONE OF EDGE OF REINFORCING BAND

Another typical example of effective EC testing of AS concerns the problem of detection of internal fatigue cracks in fuselage skin of Boeing 737 airplane in the places of juncture joints with additional reinforcing band (RB) (Figure 7, *a*). RB 3 of 0.9 mm thickness is located between the skins 1 and 2 from aluminium alloy of 0.9 mm thickness (Figure 7, *a*). The proposed EC testing procedure is oriented on detection of fatigue cracks of 0.45 mm depth (50 % of skin thickness) being initiated on the inner surface of upper skin 1 along the edge of RB 3 with access only from fuselage side (Figure 7, *c*). The problem is in the necessity of separation of the signals from cracks located on the inner surface of upper skin from sufficiently strong false signals caused by effect of RB edge being generated due to the application of low operating frequencies.

The proposed NDT procedure is based on application of low-frequency ECP of MDF 1201 type with operating frequency 26 kHz. The ECP signals were registered in a complex plane which was rotated in such a way that a signal from the RB edge being directed horizontally (Figure 7, *b*) [12]. It can be seen (Figure 7, *b*) that the signal from a crack that occurs at 0.45 mm depth deflects from a horizontal line for ~30° angle. This difference is enough for complete separation of the signals from the crack and RB edge. Moreover, an angle between these signals can be easily increased by selection larger (for example by 12 dB) amplification on a vertical axis in comparison with amplification on a horizontal line. This procedure was implemented for maintenance NDT of Boeing 737 airplane at "Ukraine International Airlines" Company (Figure 7, *c*).

DETECTION OF AS FATIGUE CRACKS THROUGH REPAIR PATCHES

Repair patches glued on airplane damaged structures are widely used as economic effective method of service life increase. The methods of repair with the purpose of reinforcement of damaged AS provide application of different materials such as aluminium alloy

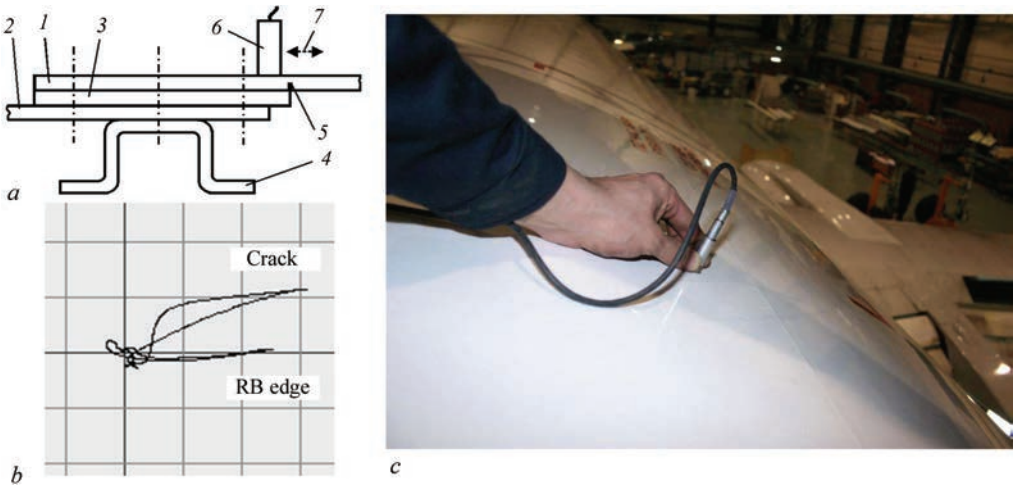

Figure 7. Multilayer structure of Boeing 737 airplane with reinforcing band (*a*): *1*, *2* — skins; *3* — RB; *4* — stringer; *5* — crack; *6* — ECP; *7* — scanning trajectory; signal from crack (*b*); testing of Boeing 737 airplane skin using ECP of MDF 1201 type (*c*)

or carbon fiber-reinforced plastic etc. Such structures are subjected to additional NDT for the purpose of detection of fatigue cracks which can appear in repaired AS under a patch. The double differential ECP were successfully used for detection of cracks through a patch from aluminium alloy glued on a damaged wing of Tu-154 airplane. After crack removal a rounded cavity was formed for reduction of mechanical stress concentration. It was expected that a crack can appear in a lower part of the cavity due to skin weakening. Because of such expectations it was planned to demount the patch every 300 landings of airplane for detection of possible cracks at the bottom of cavity using traditional EC testing methods. The procedure of EC testing built on application of low-frequency double differential ECP provided detection of cracks in a wing skin through the patch from aluminium alloy of 2 mm thickness without its dismounting.

Current AS repair technologies use the patches from composite carbon materials [14, 15]. Most often the repair patches from carbon fiber-reinforced plastic are glued on a damaged AS element from aluminium alloy. To investigate sensitivity of double differential ECP of MFD 1201 type there was produced a specimen of aluminium alloy with two electrodischarge cuts of 0.5 and 1 mm depth which was covered with a carbon fiber-reinforced plastic 4.5 mm thick sheet. Any common ECP do not have sufficient sensitivity for detection of such defects through a carbon fiber-reinforced plastic layer. The signals generated by defects under the patches were registered on operating frequency 30 kHz using EC board of EDDYMAX type in a complex plane and in a mode of time-base sweep (Figure 8) [12].

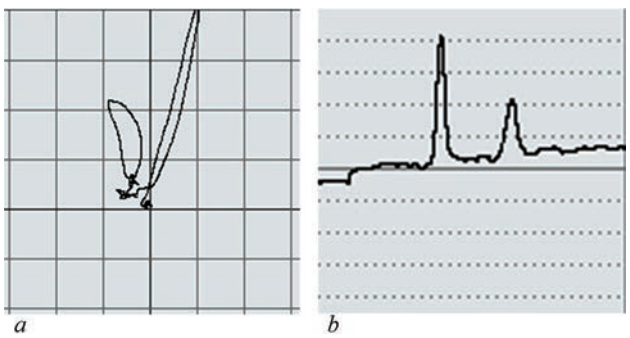

Figure 8. Signals from crack of 0.5 and 1 mm depth during testing through 4.5 mm patch from carbon fiber-reinforced plastic in complex plane (*a*) and in mode of time-base sweep (*b*)

The results given on Figure 8 demonstrate sufficiently high level of signals from a 0.5 mm deep crack during testing through a carbon fiber-reinforced plastic 4.5 mm thick patch that is enough for effective maintenance NDT. At that an amplitude of a signal correlates with a depth of detected defect that can be used for their quantitative evaluation.

ROTATION PROCEDURE OF DETECTION OF FATIGUE CRACKS IN MULTILAYER AS UNDER RIVET HEAD

Earlier it was shown that the highest sensitivity to cracks starting from rivet holes has a rotation method at which ECP is installed on a rivet head and rotated around its axis [8]. Figure 9 presents a scheme of realizing of such a procedure using double differential ECP. A special hole was made for ECP installation and centering in its body. A dielectric plate is used for centering of countersunk rivets. Accuracy of centering of ECP relatively to rivet during its rotation is important since effects the level of interferences.

Rotation ECP was tested on operating frequency 2 kHz. The specimens with a hole of 6 mm diameter were used for the investigation. On hole side surface electro-discharge cuts of 0.1 mm width and the lengths in the range from 1 to 6 mm were produced. The specimen was covered with defect-free 2 mm thick skin with a hole of 6 mm diameter and joined with a rivet for simulation of real AS (Figure 9, *a*, *b*). The ECP signals from the defects were investigated

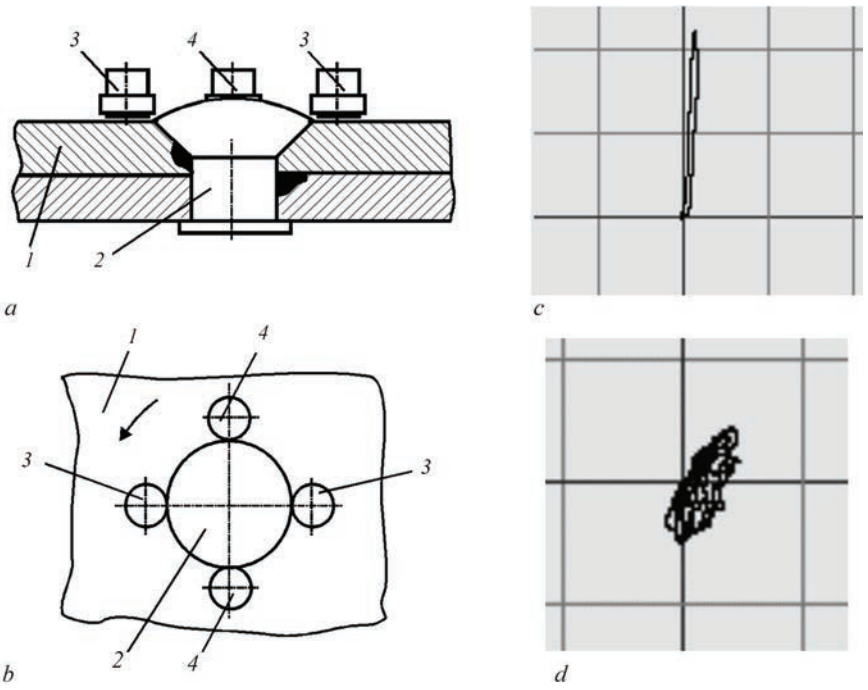

Figure 9. Rotation double differential ECP installed on rivet of double layer AS: cross section (*a*) and upper view (*b*): *1* — TO; *2* — rivet; *3*, *4* — drive and sensing coils, respectively; ECP signals in complex plane from 1 mm long crack located under rivet head and 2 mm thick skin (*c*); interference signals during ECP rotation around defect-free rivet (*d*)

in a complex plane of EC board of EDDYMAX type. Firstly, the ECP were installed on the defect-free specimen that simulates AS without defect and performed compensation of unbalance [13]. After that registration of the signals from the defects was performed by means of ECP rotation. All the defects were detected with a high signal-to-noise ratio. Figure 9, *c* as an example provides a signal in the complex plane obtained from the smallest 1 mm long defect. Figure 9, *d* shows the interference signals generated during rotation of ECP around the rivet in the defect-free specimen. These results show that a signal from the shortest 1 mm long crack for more than 6 dB exceeds the level of signal from possible interferences. It convincingly demonstrates that the proposed rotational ECP is able to detect at least the 1 mm long cracks under rivet and upper 2 mm thick skin. For many AS it means that fatigue cracks will be detected before they developed beyond the edges of a rivet head when fatigue crack reaches the critical size and avalanche-like failure of AS takes place.

PROCEDURE OF SLIDING TESTING FOR DETECTION OF FATIGUE CRACKS IN MULTILAYER AS

New highly productive procedure of detection of transverse (relatively to a row of rivets) cracks occurring in a riveted zone of AS during operation is also based on application of the double differential ECP (Uchanin V. Eddy current method of detection of defects in a rivet zone in the inner layers of one-piece aircraft structures (Pat. of Ukraine 122624, Publ. 10.12.20, Bul. No. 23).

For procedure realizing there was developed a low-frequency ECP of MDF 1502 type of 15 mm diameter. Following the proposed procedure, ECP scans AS along the rivet row line parallel to a row of rivets at some distance as shown on Figure 10.

Possibility of application of the double differential ECP for detection of transverse cracks located in a second layer of 3 mm thickness close to rivets (Figure 10) was investigated using EC board EDDYMAX. The double differential ECP provide the possibility to increase the testing reliability related with complete separation of EC signals from transverse cracks and defect-free rivets by different directions of a signal in a complex plane. This peculiarity is illustrated on Figure 10, which shows the signals for a crack of 6 mm length in a second layer in the complex plane (Figure 10, *b*) and in a mode of time-base sweep (Figure 10, *c*). For comparison Figure 10, *d* and Figure 10, *e* present the signals obtained from the defect-free rivet holes in the complex plane and in the mode of time-base sweep, respectively. It can be seen that the signals from the defect-free holes have sufficiently large amplitude since they are located in upper skin. However, these results show possibility of reliable differentiation of the signals generated by the cracks in the second layer of AS and defect-free holes, by direction in the complex plane or by sign of the signals in the time-base sweep mode. This pro-

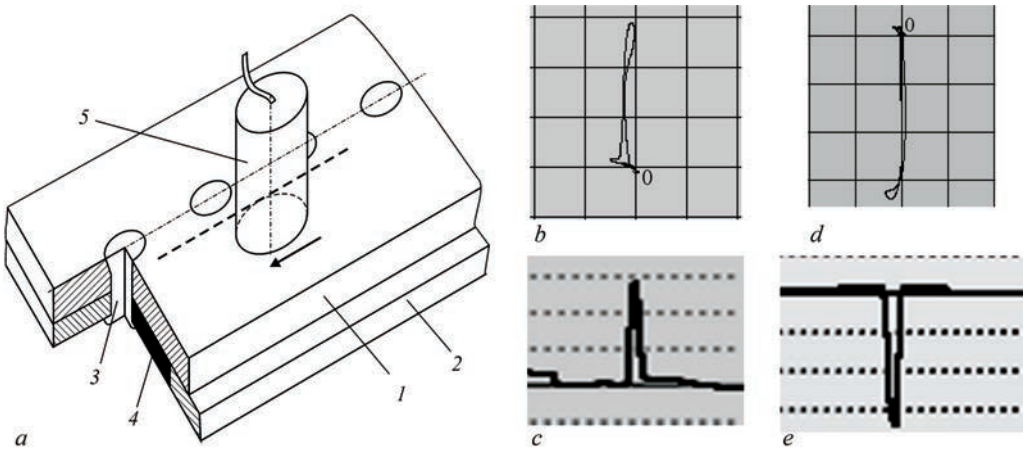

Figure 10. Scheme of realization of sliding procedure for detection of transverse cracks in rivet zone in AS second layer (*a*): *1*, *2* — first and second TO layers, respectively; *3* — rivet; *4* — transverse crack; *5* — ECP; EC testing signals in complex plane (*b*, *d*); time-base sweep (*c*, *e*) from crack in second layer (*b*, *c*) and from defect-free rivet holes (*d*, *e*)

cedure has lower sensitivity to cracks in comparison with the rotation method. Thanks to this it can be used in the cases with lower requirements as for threshold sensitivity. Nevertheless, significantly higher productivity of the sliding EC testing in comparison with the rotation method provides some advantages for on-line testing under AS operation conditions.

DETECTION OF CRACKS IN FILLET ZONE OF GAS TURBINE BLADES

To master a new NDT technology in a fillet zone of a blade there was made a 4 mm long and 0.2 mm deep cut (opening 0.2 mm) using electro-discharge method.

There is always a gap of ~1 mm between ECP operational surface and blade surface due to its curvature (Figure 11, *a*) which limits EC testing possibilities using conventional ECP. Besides, zigzag scanning of this zone provokes change of ECP position relatively to a testing surface that results in generation of high level of interferences by traditional ECP which makes impossible performance of EC testing. These limitations can be eliminated using the double differential ECP of MDF 0501 type on operating frequency 800 kHz. ECP signals were registered using EC flaw detector of ELOTEST 300 type (Rohmann GmbH Company, Germany). The results given on Figure 11, *b* also demonstrate sufficiently high level of signal of double differential ECP of MDF 0501 type in comparison with interference signals. The special double differential ECP with operational diameter 5 mm and long handle was developed for detection of cracks in a fillet zone of gas turbine blades during periodic maintenance EC testing (Figure 12).

DETECTION OF CRACKS IN HOLES OF GAS TURBINES

For detection of the defects on a side wall of gas turbine holes there was developed a special rotation head with double differential ECP based on ELOTEST SR-1 rotor of Rohmann GmbH (Figure 13, *a*). A standard specimen with a hole of 39 mm diameter was produced for testing procedure mastering. Four artificial defects of crack type of 0.2; 0.3; 0.5 and 1.0 mm depth were made on the specimen side wall.

Figure 13 *b*, *c* demonstrates the results obtained in a rotational mode at operating frequency 400 kHz with application of a standard specimen with defects without signal processing and using a filter of upper frequencies with cut-off frequency 20 Hz. In both cases there was achieved a high sensitivity with suppression of typical interferences related to non-uniformity

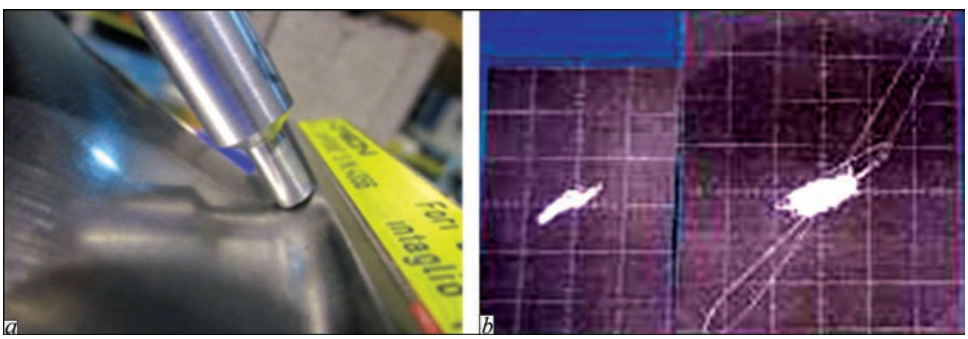

Figure 11. ECP located in blade fillet zone (*a*) and signals (*b*) of gap change during scanning of defect-free zone for different ECP orienting (left) and signal from defect (right)

Figure 12. Maintenance testing of gas turbine blades using ECP of MDF 0501 type

of magnetic properties of TO material and change of ECP position relatively to the surface during scanning.

MULTIELEMENT ECP FOR TESTING PRODUCTIVITY INCREASE

Testing of large-sized structures takes a lot of time necessary for sensitive and reliable inspection due to small dimensions of ECP. ECP with elongated sensitivity zones are used in some cases in order to increase testing efficiency. But such ECP do not correspond to the sensitivity requirements that limit their application. The best efficiency can be achieved with application of multiplex testing systems based on array ECP [16, 17]. However, such systems have high cost and necessity of adjustment to assemblies of different sizes and shapes. Our main aim was development of a new ECP characterized with high sensitivity and spatial resolution in combination with expanded testing zone and possibility of work with comparatively cheap one-channel EC flaw detectors. In order to increase testing productivity there was developed the five-element ECP of EDDYLINE 5/12 type (Uchanin V., Ivashchenko K. Multielement eddy current probe of transformer type for single-channel flaw detectors. Positive decision on invention application Ukraine No. 202101949 dated 13.04.21). The multielement ECP consists of five separate located in series ECP connected using a special switching unit for summation of signals from separate ECP (Figure 14). All separate ECP are realized by double differential scheme for better interference suppression. Thanks to such connection it was possible to get a high sensitivity zone of ~60 mm. At the same time high locality of testing was provided since each separate ECP works with the same sensitivity as before their connection by the proposed scheme.

Sensitivity of the developed ECP of EDDYLINE 5/12 type was studied on a specimen made of ferromagnetic steel St 45 with artificial defects of crack type of 0.1 mm width and 30 mm length made by electric erosion method. Produced defects have different depth in the range from 0.1 to 2 mm. Figure 15 shows the signals of EDDYLINE 5/12 type ECP from the smallest 0.1 and 0.2 mm deep notches of when a defect zone was scanned only with one separate ECP on operating frequency 200 kHz. At this moment other four ECP were located outside the specimen (in "air"). Figure 15, *a* demonstrates the signals for the same defects when the defect zone was scanned with two separate ECP. Figure 15, *c* shows the defect signals when three separate ECP simultaneously scanned a zone of elongated defect. It can be seen (Figure 15,

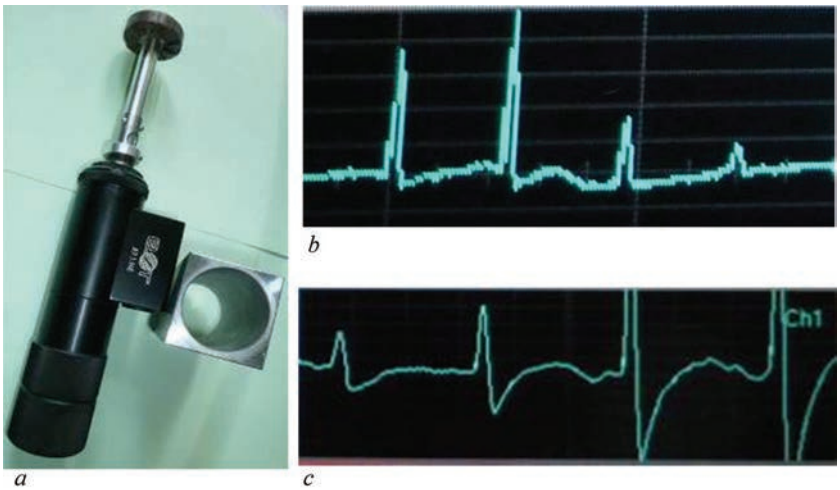

Figure 13. ELOTEST SR-1 rotor with double the differential ECP and standard specimen (*a*) and four signals from defects on side wall of hole without signal processing (*b*) and with application of filter of low frequencies with cut-off frequency 20 Hz (*c*)

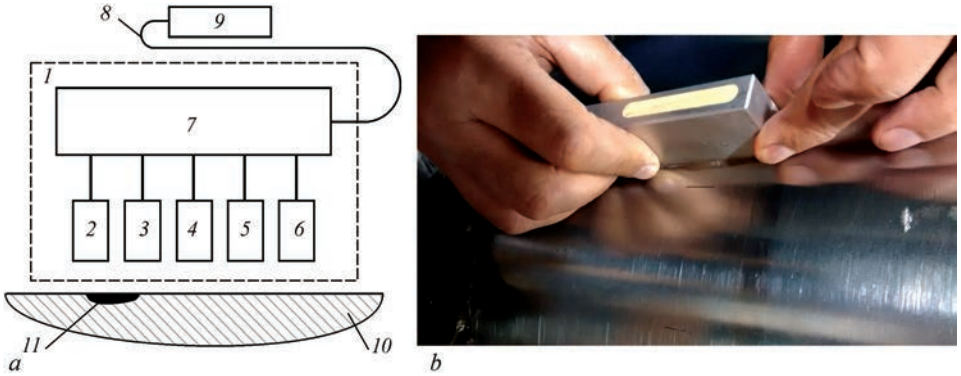

Figure 14. Construction scheme of multielement ECP for work with single channel flaw detectors: *1* — EDDYLINE type ECP; *2–6* — set of separate ECP; *7* — switching unit; *8* — connection cable; *9* — flaw detector; *10* — TO; *11* — crack; five-element ECP of EDDYLINE 5/12 type during testing of steel forgings (*b*)

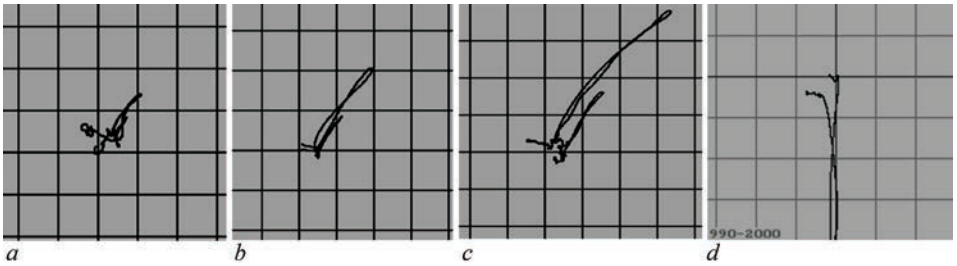

Figure 15. Signals of EDDYLINE type ECP in complex plane for one (*a*), two (*b*) and three separate ECP from 0.1 and 0.2 mm deep crack-like defects; signals from lift-off change (*d*)

a–c) that the signals of each of additional separate ECP passing over the elongated crack are summed increasing an amplitude of signal respectively to number of such ECP, i.e. an effect of possible mutual compensation of their signals is absent. Figure 15, *d* for comparison shows a lift-off signal in a complex plane, from which it can be seen that the lift-off signal and the signals from defects have opposite direction. This demonstrates possibility of reliable separation of useful signals generated by the defects, and interferences, generated by lift-off change of ECP during scanning of TO surface.

Multielement ECP of EDDYLINE 5/12 type is successfully used in a connection with a single-channel flaw detector of ELOTEST B300 type for testing of forgings from ferromagnetic and austenite steels under their production conditions (Figure 14, *b*). There were also carried out the successful trials of multielement ECP for manual testing of shafts of gas turbines and airplane shock strut pistons.

CONCLUSIONS

There was presented a design of the proposed at PMI surface eddy current probes of double differential type and analysed the peculiarities of their signals generated by the different type defects. There were given the typical examples of innovative procedures for EC testing based on application of double differential ECP. Result obtained demonstrates high sensitivity and selectivity of double differential ECP to the surface and subsurface defects of different type and large testing depth that is of particular importance for detection of hidden defects in the inner layers of the multilayer aircraft structures. Presented ECP can be used in industry for effective solution of the most difficult NDT tasks.

REFERENCES

1. Libby, H.L. (1971) *Introduction to electromagnetic non-destructive test methods*. New-York, etc. Wiley-Interscience.
2. McMaster R.C., VcIntire P. (1986) *Nondestructive testing handbook.* Vol. 4: Electromagnetic Testing (Eddy current, Flux leakage and Microwave Nondestructive Testing). Second edition. USA, American Society for NDT.
3. Dorofeev, A.L., Kazamanov, Yu.G. (1980) *Electromagnetic flaw detection.* Moscow, Mashinostroenie [in Russian].
4. Sobolev, V.S., Shkarlet, Yu.M. (1967) S*urface and screen sensors.* Novosibirsk, Nauka [in Russian].
5. Dyakin, V.V., Sandovsky, V.A. (1981) *Theory and calculation of surface eddy-current transducers.* Moscow, Nauka [in Russian].
6. Sophian, A., Tian, G., Taylor, D., Rudlin, J. (2001) Electromagnetic and eddy current NDT: A review. *Insight*, 43(**5**), 1–5.
7. Kriezis, E.E., Tsiboukis, T.D., Panas, S.M., Tegopoulos, J. (1992) Eddy Currents: Theory and Applications. In: *Proc. of the IEEE*, 80(**10**), 1559–1589.
8. Uchanin, V.M. (2013) *Eddy-current surface double differentiation probes*. Lviv, Spolom [in Ukrainian].
9. García-Martín, J., Gómez-Gil, J., Vázquez-Sánchez, E. (2011) Non-destructive techniques based on eddy current testing. *Sensors*, **11**, 2525–2565. DOI: https://doi.org/10.3390/s110302525
10. Hagemaier, D.K. (1985) Eddy-current standard depth of penetration. *Materials Evaluation*, 43(**10**), 1438–1454.
11. Mottl, Z. (1990) The quantitative relations between true and standard depth of penetration for air-cored probe coils in eddy-current testing. *NDT Inter.*, 23(**1**), 11–18.

12. Uchanin, V. (2022) Eddy current techniques for detecting hidden subsurface defects in multilayer aircraft structures. *Transact. on Aerospace Research*, 267(**2**), 69–79. DOI: https://doi.org/10.2478/tar-2022-0011
13. Uchanin, V. (2020) Detection of the fatigue cracks initiated near the rivet holes by eddy current inspection techniques. *Transact. on Aerospace Research*, 258(**1**), 47–58. DOI: https://doi.org/10.2478/tar-2020-0010.
14. *Bachir* Bouiadjra, B., Benyahia, F., Albedah, A. et al. (2015) Comparison between composite and metallic patches for repairing aircraft structures of aluminium alloy 7075 T6. *Inter. J. of Fatigue*, **80**, 128–135.
15. Bona, A. (2019) Theoretical and experimental review of applied mechanical tests for carbon composites with thermoplastic polymer matrix. *Transact. on Aerospace Research*, **4**(257), 55–65. DOI: https://doi.org/10.2478/tar-2019-0023
16. Mook, G., Michel, F., Simonin, J. (2008) Electromagnetic imaging using probe arrays. In: *Proc. of 17th World Conf. on Nondestructive Testing, Shanghai.* www.ndt.net. DOI: https://doi.org/10.5545/sv-jme.2010.173
17. Bureau, J.-F., Ward, R.C., Julien, A. (2012) Application of eddy current array technology to surface inspection. In: *Proc. of 18th World Conf. on Nondestructive Testing, Durban, South Africa.* www.ndt.net

ORCID
V.M. Uchanin: 0000-0001-9664-2101

CORRESPONDING AUTHOR
V.M. Uchanin
G.V. Karpenko Physico-Mechanical Institute of the NASU
5 Naukova Str., 79060, Lviv, Ukraine.
E-mail: vuchanin@gmail.com

SUGGESTED CITATION
V.M. Uchanin (2023) Surface eddy current probes of double differential type as an effective tool to solve non-destructive inspection problems. *The Paton Welding J.*, **2**, 46–55.

JOURNAL HOME PAGE
https://patonpublishinghouse.com/eng/journals/tpwj

Received: 23.12.2022
Accepted: 30.03.2023

SUBSCRIPTION–2023

«The Paton Welding Journal» is Published Monthly Since 2000 in English, ISSN 0957-798X, doi.org/10.37434/tpwj.

«The Paton Welding Journal» can be also subscribed worldwide from catalogues subscription agency EBSCO.

If You are interested in making subscription directly via Editorial Board, fill, please, the coupon and send application by Fax or E-mail.

12 issues per year, back issues available.

$384, subscriptions for the printed (hard copy) version, air postage and packaging included.

$312, subscriptions for the electronic version (sending issues of Journal in pdf format or providing access to IP addresses).

Institutions with current subscriptions on printed version can purchase online access to the electronic versions of any back issues that they have not subscribed to. Issues of the Journal (more than two years old) are available at a substantially reduced price.

Subscription Coupon **Address for Journal Delivery**			
Term of Subscription Since	**20**	**Till**	**20**
Name, Initials			
Affiliation			
Position			
Tel., Fax, E-mail			

The archives for 2009–2021 are free of charge on www://patonpublishinghouse.com/eng/journals/tpwj

ADVERTISING
in «The Paton Welding Journal»

External cover, fully-colored:
First page of cover
(200×200 mm) — $700
Second page of cover
(200×290 mm) — $550
Third page of cover
(200×290 mm) — $500
Fourth page of cover
(200×290 mm) — $600

Internal cover, fully-colored:
First/second/third/fourth page
(200×290 mm) — $400

Internal insert:
(200×290 mm) — $340
(400×290 mm) — $500

- Article in the form of advertising is 50 % of the cost of advertising area
- When the sum of advertising contracts exceeds $1001, a flexible system of discounts is envisaged
- Size of Journal after cutting is 200Í290 mm

Address
11 Kazymyr Malevych Str., 03150, Kyiv, Ukraine
Tel./Fax: (38044) 205 23 90
E-mail: journal@paton.kiev.ua
www://patonpublishinghouse.com/eng/journals/tpwj